Production and characterisation of carbon-encapsulated iron nanoparticles by arc-discharge plasma

Noemí Aguiló Aguayo

Production and characterisation of carbon-encapsulated iron nanoparticles by arc-discharge plasma

Noemí Aguiló Aguayo

Universitat de Barcelona

Departament de Física Aplicada i Òptica

Facultat de Física

Production and characterisation of carbon-encapsulated iron nanoparticles by arc-discharge plasma

A thesis submitted for the degree of Doctor of Phylosophy
presented by

Noemí Aguiló Aguayo

Supervisor: Enric Bertran Serra

PhD Program: Nanoscience

Barcelona, September 2012

I would like to dedicate this thesis to my loving parents Loli Aguayo Quiñones and Javier Aguiló Collar,

Εν οίδα οτι ουδέν οίδα
I know one thing, that I know nothing
Sólo sé que no sé nada

Socrates

Preface

This thesis started at the end of 2007 beginning of 2008, after the author finished the Master's thesis in Engineering Physics. During the mastery, author already acquired experience with the design of an arc–discharge plasma reactor following by the synthesis and characterisation of carbon–encapsulated iron nanoparticles. Both, thesis and master, were carried out in the FEMAN Group in the Department of Applied Physics and Optics of the Universitat de Barcelona and supervised by Dr. Enric Bertran Serra.

The present work was developed in the framework of a national project *Nanotechnologies in biomedicine* (Nanobiomed) by the program Consolider–Ingenio 2010 (CSD2006–00012) within the line of core@shell nanoparticles. This project was financed by Ministerio de Educación y Ciencia (MEDU). The author also collaborated in two more research projects about *Detection of nanometric particles by phase modulated ellipsometry* (DPI2006-03079) financed by MEDU and *Multifunctional absorbent systems of emerging pollutants based on carbon nanotubes* (CTQ2009–14674–14674–C002–01) financed by Ministerio de Ciencia e Innovación (MICINN).

Some part of this thesis was performed during two stays abroad. In 2009, the first stay was in collaboration with Prof. Dr. Judith C. Yang from the Department of Mechanical Engineering and Materials Science from the University of Pittsburgh. The second stay was in 2011 in collaboration with the Laboratoire de Technologie des Poudres (LTP) under the direction of Prof. Dr. Heinrich Hofmann in the École Polytechnique Fédérale de Lausanne (EPFL).

In addition, the work done in this thesis focused on the design and development of a modified arc–discharge plasma reactor led to the realisation of a patent.

Outline of the thesis

The aim of this thesis is the production and characterisation of carbon–encapsulated superparamagnetic iron nanoparticles (Fe@C NPs) showing very narrow size distributions with well-characterised magnetic properties for several applications, in particular those related to the biomedical field (hyperthermia, drug delivery or MRI). However, we should mention that the systematic studies of these applications were not in the framework of this thesis.

Fe@C nanoparticles are being researched heavily, since they present advantageous properties over other protective coatings such as polymer or silica, the carbon coating protects the iron core from oxidation, chemical and thermal degradation and therefore, magnetic cores present stable magnetic properties when nanoparticles are exhibited in air or other environments. Several studies about carbon–encapsulated magnetic nanoparticles were already reported. However, nanoparticles are obtained rather polydisperse and not very uniform. For this reason, the production of Fe@C nanoparticles with controlled morphological and structural properties as well as the systematic study of their magnetic properties is still a challenge in this field.

The content of this dissertation comprises the design of two arc–discharge plasma (ADP) reactors (a conventional and a modified one); the experimental study of the different reactor parameters involved; the morphological, structural and magnetic characterisation of the obtained Fe@C nanoparticles; the comprehension of the mechanisms involve in the formation of this kind of core@shell nanoparticles in comparison with Fe@C nanoparticles obtained by other methods; and finally, a first approach to the functionalisation of the nanoparticles for the biomedical applications. A general flow chart about the thesis plan is shown in Fig. 1.

This thesis is structured in four parts: Backgrounds, Nanotools, Results and Conclusions. The first part contains Chapter 1. The second part consists in Chapter 2 and Chapter 3. The third part contain from Chapter 4 to Chapter 8 and finally, a list of conclusions are described.

Chapter 1 – Basis of Fe@C nanoparticles

A general introduction of the nanoparticle properties derived from their nanometric dimensions is presented in this chapter. The state of the art about the formation mechanisms and techniques used for the generation of this kind of nanoparticles is described. Several applications of this kind of nanoparticles in fields such as biomedicine, electronics or food and environmental, are also presented.

Chapter 2 – Characterisation methods

The most common characterisation techniques used to investigate the morphological, composition, structural and magnetic properties are described within this chapter. Details about the equipments and conditions used during this thesis for the characterisation of the Fe@C nanoparticles are also reported.

Chapter 3 – Experimental set-up

In this chapter, the description of two different arc-discharge reactors used during this thesis is presented. The first reactor (conventional ADP) was developed by following similar experimental setups described in the literature. Second reactor (a modified ADP) was designed to overcome the disadvantages from the first reactor and to obtain high quality nanoparticles (narrower size distribution, uniform composition).

Chapter 4 – Preliminary studies from conventional ADP reactor

This chapter presents a design of experiments (DOE) based on the Plackett-Burman design in order to evaluate the reactor parameters that influence the most the final characteristics of the nanoparticles. This study was performed using the conventional ADP reactor and the preliminary results were very useful for the development of next generation of experiments using the second reactor, the modified ADP.

Chapter 5 – Generation of Fe@C NPs by a modified ADP reactor

Morphological and structural properties of Fe@C NPs obtained by the modified ADP reactor are presented. The discussion of the effect of the most relevant parameters on the formation of the nanoparticles is reported. Iron core diameters with corresponding size distribution as well as the carbon shell formation obtained under different parameter conditions are investigated.

Chapter 6 – Magnetic properties of Fe@C NPs

A systematic study of the magnetic properties of the nanoparticles obtained in Chapter 5 is performed. Size-dependent variables such as magnetic moments, coercivity values, blocking temperature and anisotropy energies are presented. Magnetic properties were in agreement with the morphological characteristics of the nanoparticles.

Chapter 7 – Comparison of annealed Fe@C nanoparticles

The comparison of annealed Fe@C nanoparticles obtained by mADP and chemical vapour deposition (CVD) method is presented in this chapter. Differences on the morphological, structural and magnetic properties are studied. Structural evolution of nanoparticles during annealing treatment under in–situ TEM observations is investigated.

Chapter 8 – First approach to biomedical applications

As a first approach to biomedical applications, the stabilisation of the nanoparticles in aqueous solution by using polyvinyl–alcohol is investigated. Results of the internalisation of the nanoparticles into HeLa cells are presented.

As supplementary information, the Appendix contains information about the produced samples, the resume of the author with a list of publications, patents and conferences attended.

Figure 1: General flow chart about the thesis plan.
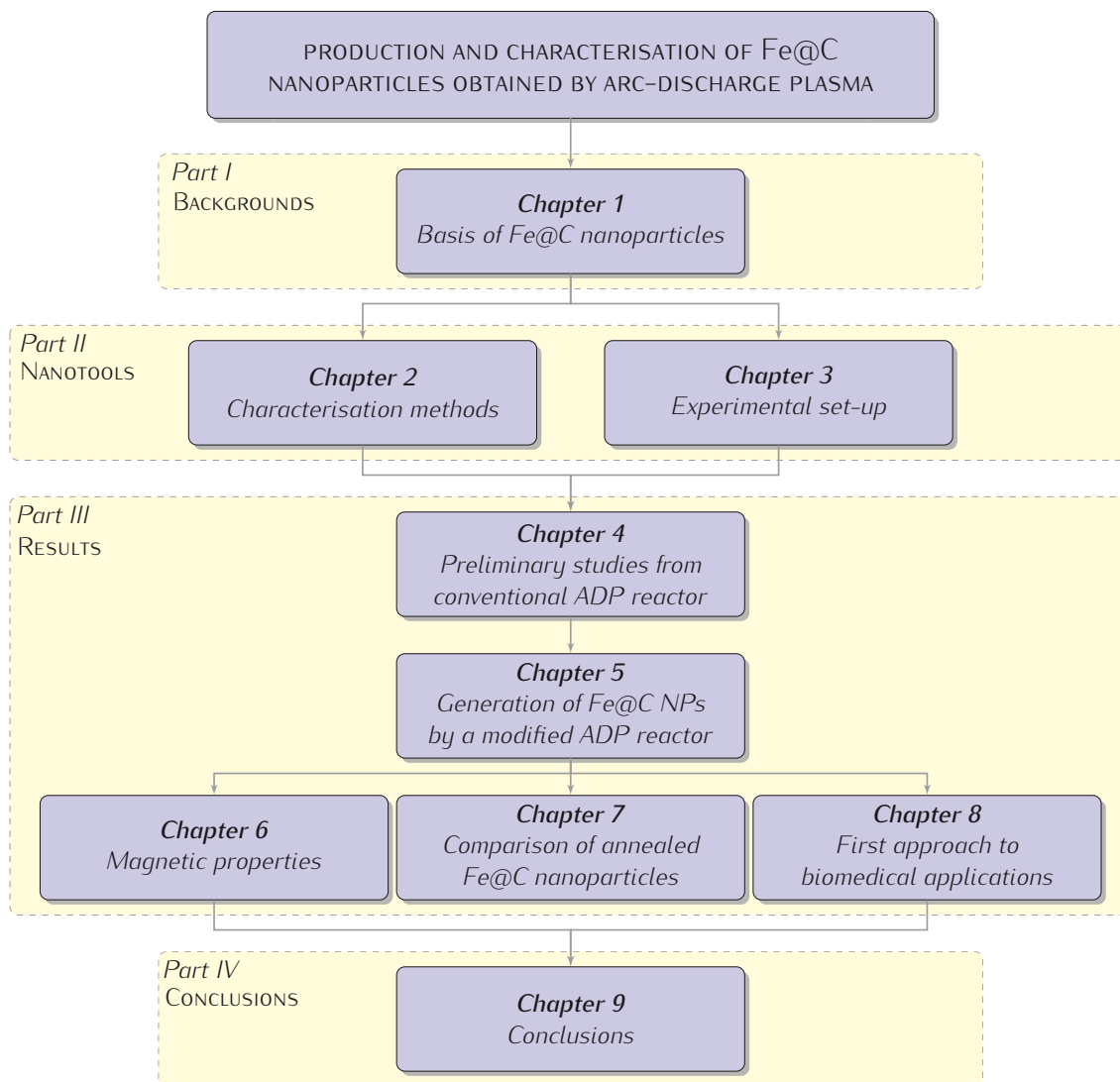
Agraïments

Quan comences aquest capítol només desitges una cosa, no oblidar-te de ningú.

Per començar m'agradaria donar les gràcies al meu tutor Enric Bertran per oferir-me l'oportunitat de treballar amb el grup FEMAN i dur a terme aquesta tesi doctoral. Sempre li estaré molt agraïda per la confiança que ha dipositat en mi en tot aquest procés de la tesi, per oferir-me l'oportunitat de participar en el gran nombre de congressos interessants als que he pogut assistir i per donar-me suport en realitzar estades a l'estranjer. A nivell més personal, donar-li les gràcies pel regal de la meva gateta Guen sempre present amb mi en aquests darrers 5 anys.

Aquest treball no hagués estat possible sense el suport incondicional dels meus pares, als quals va dedicada amb especial amor aquesta tesi. Ellos han sido y son mis grandes maestros, no hay día que no me enseñen algo nuevo. Si existe algún tipo de suerte, yo la agoté toda con los padres que me tocaron. Si existeix la sort, la vaig esgotar tota amb els pares que em van tocar. Juntament amb els meus germans, Ingrid i Xavi, agraïr-los la seva atenció i el coratge que m'han sapigut trasmetre en els pitjors moments.

Amb especial amor, vull agraïr a en Dani la seva paciència durant tot aquest temps i el seu amor incondicional en els millors i pitjors moments. Suportar algú que fa un doctorat no és gens fàcil i si hi ha algú que s'hagi llegit tota aquesta tesi, és ell. Crec que aquestes alçades deu saber més de nanopartícules que jo mateixa.

Continuar agraint als meus amics germans de l'ànima, David y Rubén, Rubén y David, gracias de verdad, me habéis aguantado como nadie sabe, en todos los aspectos de mi vida, y como no, en la tesis y en su parte más dolorosa, la escritura. Para ser justos necesitaría escribir un par de tesis más para agradecer a cada uno lo que se merece, y aún me quedaría corta. Y también gracias a sus respectivas parejas, a Jose que en estos últimos meses le he calentado la cabeza con preguntas sobre química, me he acoplado a todos sus planes con Rubén y que un poquito

más y ya no sabe como sacarme de su vida. Y a Rubén F. por mandarme todas esas fotos que me ponen al día, por hacerme sentir en su casa como si fuera la mía, y por cocinar esos platos tan exquisitos que le alegran a uno la vida.

Al meu amic Albert Pridas, que sempre el sento al meu costat i encara que ell no en sigui conscient, representa un punt d'encontre amb mi mateixa.

Al meu petitó Mathís, per donar-me la felicitat més gran d'ésser tieta en els darrers moments i més crítics de la tesi. Per quan siguis gran i si encara segueix rondant la meva tesi per ahí, aquestes paraules són per tu petitó meu, gràcies per les abraçades que em vas donar que van aconseguir fer-me oblidar de totes les preocupacions. I també gràcies al seu pare Sergi, perquè en aquestes darreres setmanes també ha estat donant-me suport en la tesi, dissenyant portades com un boig per la seva cunyada!

I would like to thank all the people who I met during my stays abroad, specially to Prof. Judith Yang and Prof. Heinrich Hofmann for giving me the opportunity to work with them. Thank you very much for your interest and your time sharing interesting discussions and perspectives. I would also thank to the people who I met in Pittsburgh, specially to Nuria and Mari Paz who made my stay there as if I was at home, as well as to Dr. Zhenyu Liu, who helped me and supported my work in Pittsburgh from the beginning. During my stay in Lausanne, I have a special love to the good memories from the time that I spent with Lionel and Rakesh, traveling around Lausanne by car singing Dragon Ball in catalan, french and maybe also english. Thanks my lovely friend Rakesh for our discussions about physics and to open my heart again to people. Thanks Lionel for your eternal support during and after my stay, you were an excellent colleague and I am really grateful to have worked with you. I would like to also thank all the people from University of Pittsburgh and the LTP group who shared with me all their knowledge and were always ready to help me.

También me gustaría agradecerles a Mai, Damarys, Virginia y Coté por la amistad que me han ofrecido durante este tiempo, por esas risas y *pijamadas* que tanto echaré de menos.

Al Centre Científic i Tecnològics de la UB o el que era abans, els serveis cientifico-tècnics, per tenir a l'abast tota mena d'equips i gent especialitzada que m'han ajudat en tot moment, voldria agraïr amb especial atenció a la Dra. Núria Clos, per les mesures de l'SQUID, al Dr. Tariq pel seu suport en les mesures de Raman, a la Regina Roca per la seva ajuda en les mesures d'anàlisi elemental i finalment a tota la gent de microscopia, de raigs-X i AFM, en especial a Dr. Quim Portillo, Joan Mendoza, Dra. Sònia Estradé, Dr. Xavier Alcobé i Dr. Gerard Oncins.

També agraïr a tots els companys del departament i del grup FEMAN, i la gent que ha anat arribant i marxant, en especial a en Javi per tota l'ajuda amb el reactor, en Carles Ros per la seva ajuda en la preparació de mostres and thanks to Reza and Stefanos for keeping work in this issue. Good luck!

Contents

List of Figures

List of Tables

Part I

BACKGROUNDS

1

Basis of Fe@C nanoparticles

The 21st century has become the era of nanoscience and nanotechnology. The discovery of new properties related to the nanosize scale has made researchers all over the world to focus on the development of new nanomaterials with unique characteristics, and thus devising revolutionary applications. All of this happens within a context where the technology market is moving towards smaller devices with higher capability and with multi-functionality. However, the technology market is not the only beneficiary of this new era, the discovery of structures of nanosize scale has made possible the approach to the bio-world opening new routes to fight diseases such as cancer, malaria, alzheimer and degenerative diseases, among others.

As early as 1959, the physicist Richard P. Feynman, known as the father of the nanotechnology, presented a talk entitled *There's Plenty of Room at the Bottom* at the annual meeting of the American Physical Society at the California Institute of Technology (Caltech), where he already foresaw the importance of the *small scale* and the enormous potential of a new field moving in this direction. In 1985, researchers from Rice University discovered a new allotropic form of carbon, spherical fullerenes, named C_{60} or buckminsterfullerene (buckyball). This new structure similar to graphite, but with a cage-like structure composed by carbon atoms in a soccer-ball orientation, showed new properties of heat resistance and superconductivity in comparison with the allotropic forms hitherto known, graphite and diamond. This was the first step to a new nanoscience field related to the development and study of several carbon-based nanostructures, such as graphene, single, double and multiwalled carbon nanotubes (SWCNT, DWCNT, MWCNT), carbon nanobuds, fullerites, or carbon-encapsulated magnetic nanoparticles (CEMNPs). These nanomaterials exhibit novel physical and chemical properties for instance, extraordinary

strength and thermal conductivity, unique electrical properties or a new magnetic behaviour (superparamagnetism) with potential applications.

Within this chapter, we will explain how physical and chemical properties change in nanoparticles as a consequence of the energy competition between bulk and surface. We will focus on carbon-encapsulated magnetic nanoparticles, in particular, Fe@C nanoparticles, we will review the growth mechanisms that have been so far described in the literature, we will describe the most common techniques used for their fabrication and finally, we will mention a list of the most promising applications.

1.1 Nanoworld: Size matters

Nanoparticles have been used since the dawn of civilization. In the fifth century Romans used gold nanoparticles for the fabrication of coloured glasses and ancient Chinese used carbon nanoparticles in the composition of their inks for the preservation of their paintings. Nanoparticles can be formed by natural processes, such as in volcanic plumes or via chemical disintegration of organic materials in plants or microorganism debris. However, until the development of instruments and equipments which allow us the characterisation at an atomic level, it was not possible to become aware of their existence.

The importance of the nanomaterials stems on their high surface-to-volume ratio, their characteristic length-scale is so small that new properties emerge different than bulk materials, making nanoparticles very interesting for many applications. Mechanical, thermal or optical properties are influenced by shape, size, structure and orientation and can be changed from the already known bulk ones. When their characteristic size is large enough, the physical properties under consideration tend to be those of the bulk material.

1.1.1 Nanothermodynamics

At this level, thermodynamic properties (surface tension, chemical potential, vapour pressures, melting points) become size-dependent. At the macroscopic level, large systems are described by classical thermodynamics functions considering uniformity and equilibrium. In small systems, thermodynamics functions will be defined assuming under *quasi-thermodynamic assumption* or the so-called *point thermodynamic approximation*, but fundamental questions regarding the definition of local temperature at this scale are still under investigation [Amer et al., 2010].

High rate of atoms in the surface implies different coordinate number (number of neighbouring atoms) between the surface atoms and the inside atoms. Surface atoms are less stable, offering high affinity to form bonds (higher catalytic activity). Surface atoms influence the average cohesion energy of the nanoparticle, the average bond energy per atom, decreasing with decreasing the nanoparticle size and showing different values than bulk materials.

The fraction of atoms at the surface is called dispersion F and is proportional to $\propto N^{-1/3}$, where N is the total number of atoms. Due to this scaling law, all properties which depend on the fraction surface atoms lead to a straight line when plotted against r^{-1}, d^{-1}, or $N^{-1/3}$ [Roduner, 2006].

1.1.1.1   Surface energy

Cohesive energy is the responsible for the surface energy, As we already mentioned, atoms from the surface present less cohesive energy than those from the bulk, and cohere more strongly to those directly associated with them on the surface (adhesive forces). Surface energy will play an important role in nanoparticle systems, promoting relevant phenomena such as solubility, high vapour pressure or lower melting points.

Surface energy, γ is defined as the energy required to create a unit area of a new surface (J/m^2), it can be also named surface tension defined as the force per unit length that opposes the expansion of a surface area (N/m). Both are the same, however, surface energy is often used in solids, whereas surface tension is often applied to liquids. Surface tensions are represented in Fig. 1.1 for a spherical particle (left image) and for a droplet liquid deposit on a solid flat surface. Different energy tensions appear at interfacial liquid–gas, solid–gas or solid–liquid phases.

When nanoparticles present spherical shape, they display liquid–like behaviour showing specific properties associated to fluids (example, pressure). However, when nanoparticles show geometric shapes, they behave more like crystals since their internal energy dominates over the surface energy.

The surface energy is equal to,

$$\gamma = \left(\frac{\delta G}{\delta A} \right)_{p,T} \tag{1.1}$$

where, G is the Gibbs free energy in J and A is the area in m^2, ΔG is negative os spontaneous when surface area is decreased and positive, requiring energy input, when surface is increased. However, if energy is required to create a new surface, a release of energy will occur when surfaces are merged, and therefore a release of energy in the form of heat occurs when two nanoparticles merged to form a larger one showing spherical shape (liquid–like behaviour), this process is called coalescence [Hornyak et al., 2008].

1.1.1.2   Kelvin Equation

In 1805, Thomas Young and Pierre Simon de Laplace independently deduced the pressure difference (difference between internal, p_α and external pressure, p_β) across the surface of a particle, known as the Young–Laplace equation (Fig. 1.1),

Figure 1.1: Representation of the surface tension for a spherical nanoparticle (left image) and liquid droplet on a flat solid surface (right image).
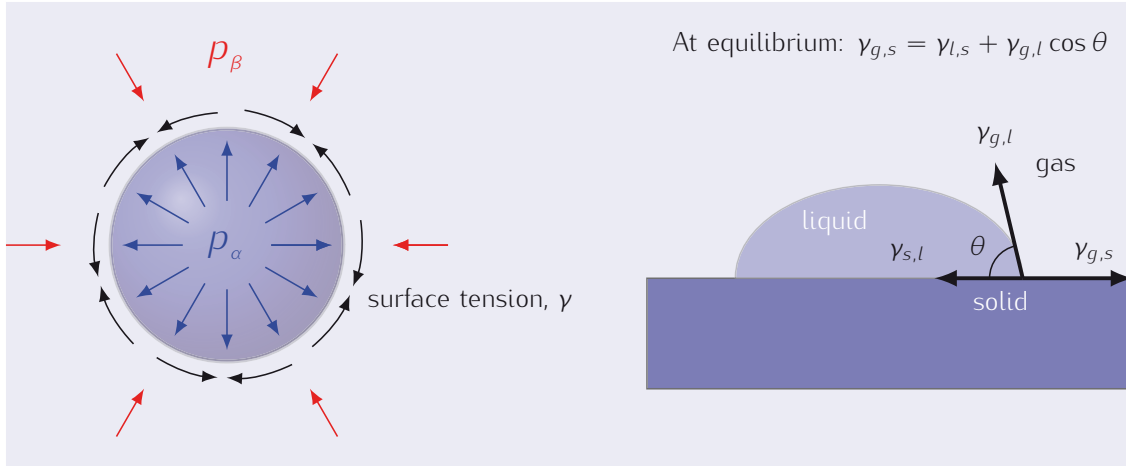
$$p_\alpha - p_\beta = \gamma \left(\frac{1}{R_1} + \frac{1}{R_2} \right) \tag{1.2}$$

where R_1 and R_2 are the radii of curvature along the x and y-axes, and γ is the surface energy [Pellicer et al., 2000]. In a sphere, the equation would be simplified to $\Delta p = 2\gamma/R$. The Young–Laplace equation shows that the pressure inside the particle is always larger than the external pressure.

If we consider now that the pressure into consideration is the vapour pressure, a direct consequence of the Young–Laplace equation is that the vapour pressure for a nanoparticle, p_0^r, is larger than that for a flat surface, p_0^∞. The Kelvin equation describes this dependence of vapour pressure with curvature of a nanoparticle,

$$p_0^r = p_0^\infty \exp \left(\frac{2\gamma V_a}{r k_B T} \right) \tag{1.3}$$

where V_a is the atomic volume, r is the radius of the particle, k_B is the Boltzmann constant and T is the temperature.

From the above, one can derive that melting temperature also exhibits a size–dependent behaviour. The so–called Gibbs–Thomson equation describes the dependence of the melting temperature with the curvature. For spherical nanoparticles,

$$T_m^\infty - T_m^r = \left(-\frac{2T_m^\infty \gamma_{s,l}}{\Delta H_f^\infty \rho_s r} \right) \tag{1.4}$$

where, T_m^∞ and ΔH_f^∞ are the melting temperature and latent heat of fusion for the bulk material, ρ_s is the solid phase density, $\gamma_{s,l}$ is the solid–liquid interfacial energy and r is the radius of the

spherical particle [Gibbs et al., 1902, Sun and Simon, 2007].

From the Gibbs-Thomson equation it is also assumed that heat of fusion decreases with particle size due to an increase in the surface energy as,

$$\Delta H_f(r) = \Delta H_f^\infty - \frac{2\gamma_{s,l}}{\rho_s r} \tag{1.5}$$

Shibuta and co-workers [Shibuta et al., 2009] investigated the melting temperature of iron nanoparticles as a function of the particle size by a classical molecular dynamics simulations. They represented the depression of the Fe melting point from the bulk value as a function of the particle size for Fe nanoparticles inside liquid iron and freestanding (Fig. 1.2). They results showed an estimated value of the Gibbs-Thomson coefficient, $\Sigma = 2.1 \cdot 10^{-7}$ mK, ($\Delta T = 2\Sigma/r$), which was 1.1 times the experimental value found in iron-carbon alloy.

Figure 1.2: Depression of the Fe melting points for nanoparticles embedded in liquid iron and freestanding as a function of the inverse of the particle radius, reprinted from [Shibuta et al., 2009].
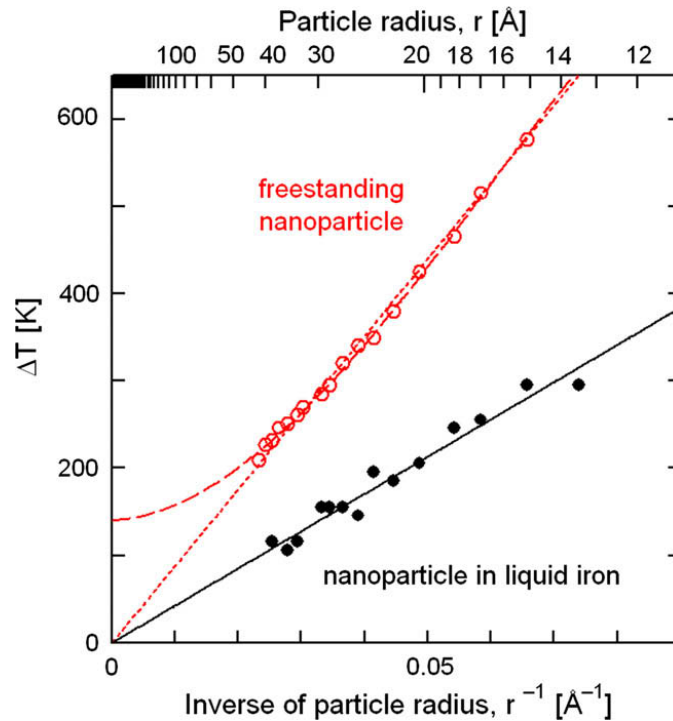
1.1.1.3   Lattice parameters

The dependence of the crystal lattice parameter with nanoparticle size has been investigated from 1950 [Nicolson, 1955]. However, there is still disagreement between theory and experiments.

For spherical nanoparticles, the simplest expression to estimate the surface tension with lattice contracts is,

$$\frac{\Delta a}{a^\infty} = -\frac{2\gamma\beta}{3r} \tag{1.6}$$

where Δa represents that lattice contracts uniformly, a^∞ is the lattice parameter from the bulk material, γ is the surface tension, β is the compressibility of a elastically–isotropic sphere and r is the radius of the particle. This expression, however, ignores the anisotropy of surface tension and elasticity and make further assumptions on the relation between volume and lattice parameter changes [Stoneham, 1977].

It has been observed that the lattice parameter contracts or expands with decreasing the size depending on the surface and volume stress, nature of the interatomic bonds, an excess or deficiency of an atom in the surface. Nanoparticle compounds such as Pb [Wang et al., 2012], Cu [Montano et al., 1986], Au [Zhang and Sham, 2002], Sn, Bi are reported to decrease their lattice parameter as particle decreases [Sheng et al., 2010]. However, α-Fe_2O_3, MgO, TiC [Fukuhara, 2003], Pt [Du et al., 2010], CeO_2 [Hailstone et al., 2009], the lattice parameter contracts. Other nanoparticles, Ni and Pd, seemed to present both lattice contraction and expansion depending on their size [Sheng et al., 2010].

Concerning α-Fe nanoparticles, Choi and co-workers [Choi et al., 2002] synthesised nanoparticles composed by an iron core encapsulated by an iron–oxide shell, they studied the evolution of the lattice parameter as a function of the Fe diameter and found an expansion of the lattice constant with the decrease of the core size (Fig. 1.3).

1.1.2   Quantum confinement effect

When nanoparticles present diameters on the order of the de De Broglie wavelength, another size-effect named quantum confinement is produced and the energy spectrum changes from continuous to discrete.

In solids, the energy levels of electrons can be assumed to be near continuous, forming the conduction and valence bands. The energy difference between the top of the valence band and the bottom of the conduction band is called band gap and depending on this energy, materials can be classified by conductors, insulators and semiconductors.

In very small nanoparticles, the band structure is not longer valid and energy states become discontinuous. In the simplest model, a nanoparticle can be considered as an *electron box*, where energy levels are the solutions of the Schrödinger equation for the box of a given

Figure 1.3: Dependence of the lattice constant of bcc iron as a function of the particle size reprinted from [Choi et al., 2002], for α-Fe bulk the lattice constant is 2.8664 Å.
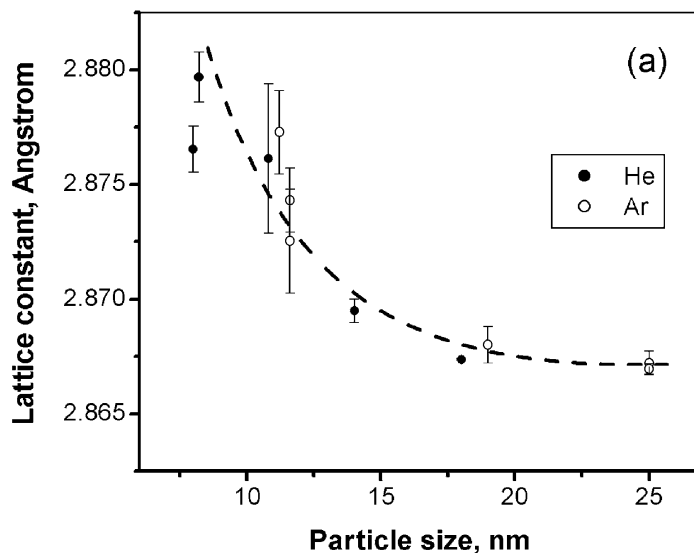
size and geometry [Society, 2001]. The Kubo gap (δ) is the average spacing between two consecutive energy levels, given by $\delta = 4E_F/3N$ (E_F is the Fermi energy and N is the nuclearity, the number of atoms), and is measured in terms of meV [Kubo, 1962]. The Kubo gap will govern some physicochemical properties, optical absorption and fluorescence become size-dependent and new properties emerged, such as photoluminescence (spontaneous emission of light from a material under optical excitation [Gfroerer, 2006]). This was observed in nanoparticles compounds, such as Si (3.4–4.8 nm in diameter) [Ledoux et al., 2000], GaN (diameters of 5–8 nm) [Cao et al., 2000] or in ZnO (20 nm in diameter) [Alim et al., 2005]. Nanoparticles that present quantum confinement are also named as quantum dots. In addition, when Kubo gap is equal to thermal energy, non–magnetic materials can become magnetic or magnetic properties can change dramatically [Roduner, 2006]. For instance, bulk Au does not show magnetic behaviour, however, 2–3 nm gold nanoparticles become magnetic, or for Pb nanoparticles, when size is decreased from 65 to 7 nm, the superconducting transition temperature also decreases from 7.24 to 6.4 K [Ghosh., 2011].

1.1.3 Superparamagnetism

Magnetic behaviour is also affected by the large surface–to–volume ratio of nanoparticles. In atomic clusters, due to the high number of atoms in the surface and the lower effective co-ordination number, the orbital hybridisation is different than in bulk material showing lower magnetic moments per atom with the decrease of the nanoparticle size. In Fig. 1.4 is depicted

the effective magnetic moment per atom as a function of the number of atoms for a Fe cluster. The dependence of the magnetic moment with the effective coordination number is approximately linear, but not decay monotonically. Magnetic moments do not depend exclusively on the number of atoms of the cluster at a fixed temperature, they also depend on the cluster crystalline structure [Sattler, 2010b].

Superparamagnetism occurs in ferromagnetic materials (Fe, Ni, Co) when sizes are reduced under a critical diameter and become comparable with fundamental magnetic lengths (effective anisotropy length, $l_k = \sqrt{A/K}$[1], the magnetostatic length, $l_S = \sqrt{A/2\pi M_S^2}$, the applied field length $l_H = \sqrt{2A/HM_S}$ [Leslie-Pelecky and Rieke, 1996]). Under these conditions, the energy required to form magnetic domain walls along a nanoparticle is larger than the magnetostatic volume energy associated to a single–domain (monodomain) nanoparticle, thus preventing the formation of magnetic domains [Gubin, 2009]. A schematic drawing of the orientation of the atomic spins in a superparamagnetic (a) and a ferromagnetic (b) nanoparticle is depicted in Fig. 1.5. If we consider negligible the effect on the surface spin canting and we assume that all the spins rotate coherently, the superparamagnetic nanoparticle behaves then as a large magnetic dipole, similar to the situation of a paramagnetic material. In paramagnetism, we talk about μ as the magnetic moment per atom, whereas in superparamagnetic nanoparticles, μ is considered as the magnetic moment per nanoparticle with higher magnetic moments, $\mu \approx 1000\mu_B$, hence the name of superparamagnetism.

When a magnetic field is applied to a ferromagnetic system, magnetic domains try to orientate at the same direction of the field, reaching a saturation magnetisation. When the magnetic field is removed, magnetic domains are disorientated but the sample retains most of the magnetisation, the so–called remanent magnetisation. These are the basis of a hysteresis loop for a ferromagnetic material. The coercive field is defined as the opposite applied magnetic field required to reduce the remnant magnetisation to zero. In nanoparticles, the coercive field is size–dependant. Fig. 1.6 shows the dependence of the coercivity with the diameter of the nanoparticle at thermal equilibrium [Cullity and Graham, 2009, Kneller and Luborsky, 1963].

There are two different regimes: stable single–domain named also blocked state, and the superparamagnetic state, depending on the relaxation time of their magnetic moments. Superparamagnetic nanoparticles show zero coercivity since thermal energy overcomes easily the energy barrier, and the magnetisation easily flipped during time measurements. For blocked nanoparticles, the magnetic moments are thermally stable and do not flip during time measurements, magnetisation is fixed at certain directions showing a higher coercivity than bulk materials as a consequence of the non existence of domains.

---

[1]K is the effective anisotropy constant of the bulk material and A is the exchange stiffness constant

Figure 1.4: Calculated magnetic moments for atom–centred (plus signs, a), bridge–centred (crosses, b) and icosahedral (triangles, c) with corresponding experimental results for Fe clusters, as a function of the number of atoms. The dotted line corresponds to the bulk magnetic moment of $2.2\,\mu_B$ (reprinted from [Sattler, 2010b]).
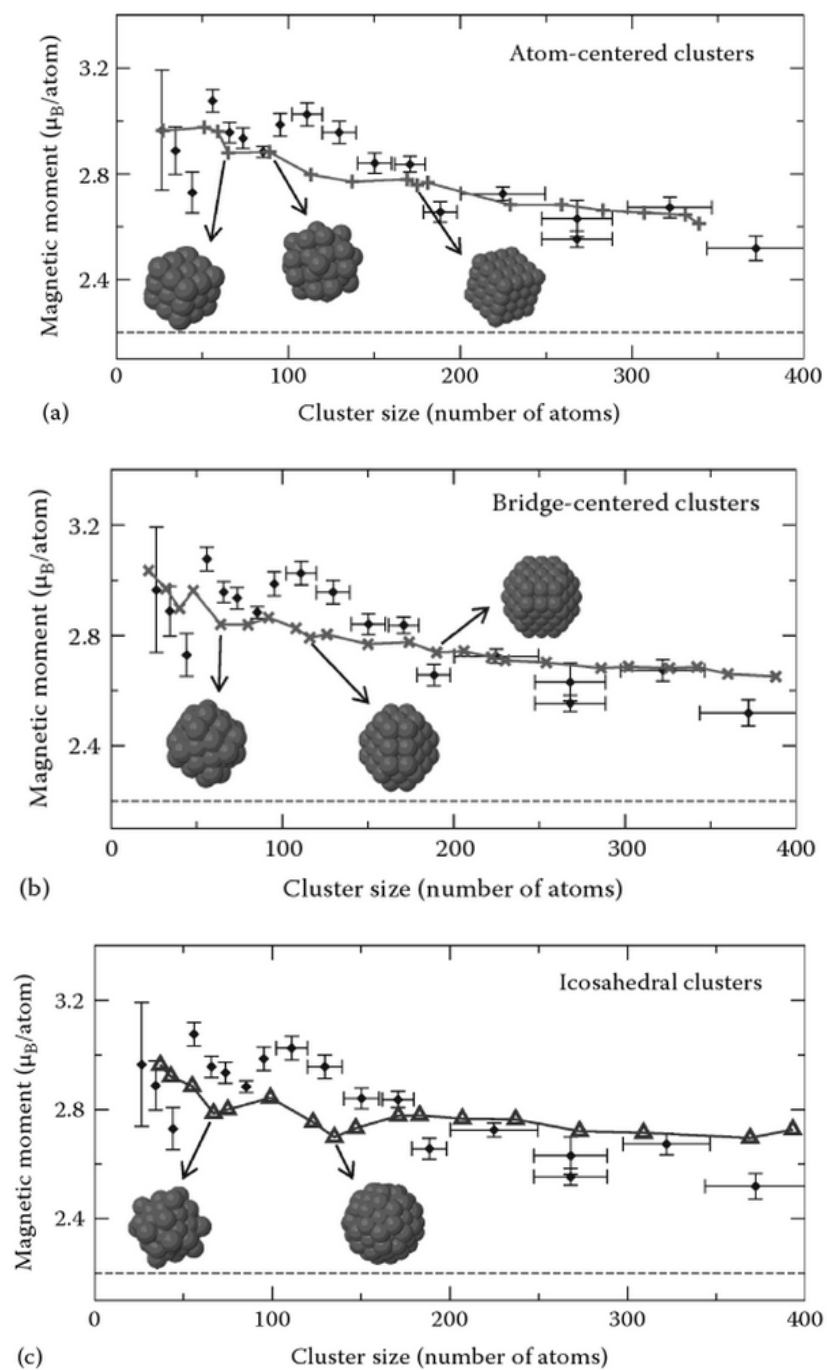
Figure 1.5: Schematic representation of (a) single–domain nanoparticle showing no magnetic domains and large demagnetising field and (b) Ferromagnetic nanoparticle showing two magnetic domains divided by a diametral plane, reducing demagnetising fields and thus, magnetostatic energy.
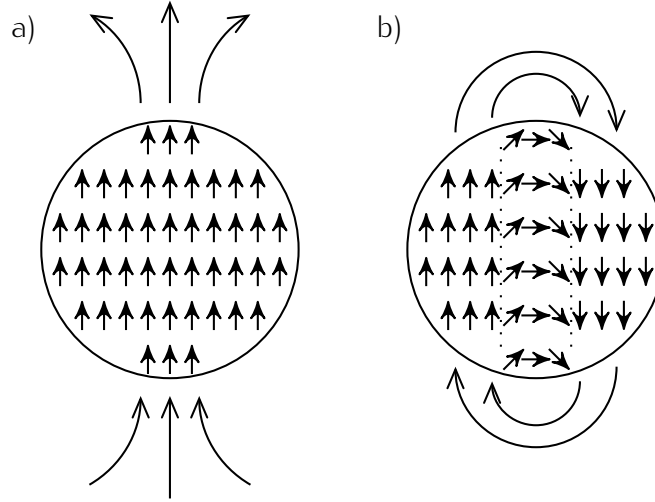
Remanent magnetisation for nanoparticle systems is observed to decay exponentially with time, $M(t) = M_0 e^{-t/\tau}$, as a consequence of the effect of thermal activation. Louis Néel in 1949 [Néel, 1949] studied the spontaneous magnetic relaxation in magnetic grains and showed that the relaxation time was described by an Arrhenius law as follows (eq. 1.7),

$$\tau = \tau_0 e^{E_b/k_B T} \tag{1.7}$$

where E_b is the energy barrier required to reverse the magnetisation, k_B the Boltzmann constant, T the temperature and τ_0, is an intrinsic time, $10^{-12} - 10^{-9}$ s, inversely proportional to the jump attempt frequency of the magnetic moment.

Therefore the classification in these two regimes can be either blocked or superparamagnetic state, which will depend on the temperature and the time window of the experiments. If experimental techniques use larger time scales than the relaxation time, the nanoparticle will present superparamagnetic behaviour, otherwise, nanoparticle will be observed as blocked in certain directions. In Mössbauer spectroscopy the time window is 10^{-8} s, whereas in SQUID measurements, the time window is larger, about 100 s [Knobel et al., 2008]. For nanoparticles showing high surface anisotropy magnetisation, the magnetisation flipping occurs as a successive switching of individual spins inside the particle, and the assumption of one–spin per nanoparticle is not longer valid and other interpretations up to present [Kachkachi and Garanin, 2005].

Figure 1.6: Schematic drawing showing the dependence of intrinsic coercivity H_{ci} with particle diameter D. D_c corresponds to the single–domain particle critical diameter and D_P corresponds to the superparamagnetic particle critical diameter. For iron, D_c is around 15 nm and D_P is around 9 nm at room temperature [Gangopadhyay et al., 1992].
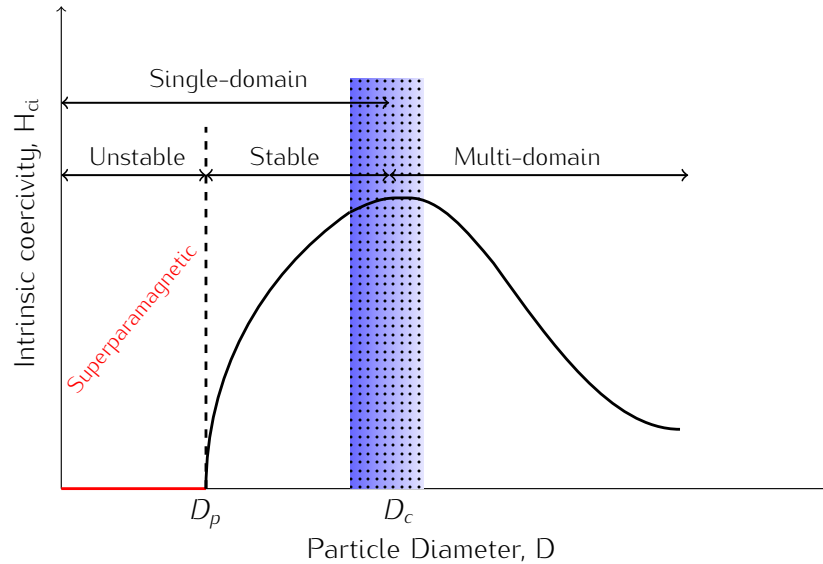
1.1.4 DLVO theory

In nanoparticle systems other forces different than those for macroscopic systems come into play, this is the case of gravitational force, which will become less important than other forces such as the electrostatic or van der Waals. DLVO theory, developed in 1940s by Boris Derjaguin and Lev Landau and independently by Evert Verwey and Theo Overbeek [Derjaguin and Landau, 1993, Verwey, 1947], described the behaviour of nanoparticles in liquid (colloidal solutions) due to the competition of different interactions, based on the attraction potential due to van der Waals forces and repulsion potential due to electrostatic forces. These results will define the colloidal stability of the nanoparticles in liquid (adhesion and aggregation, or highly dispersed nanoparticles). The DLVO theory fails in the explanation of the short–distance interactions (highly concentrated solutions) or when other forces come into play, such as, hydrophobic forces, hydration forces or steric repulsive forces [Israelachvili, 2011a].

Brownian motion has an important role in nanoparticle systems. At higher temperatures, small nanoparticles in suspension undergo higher random thermal motion (brownian motion), increasing the chances that two nanoparticles make an approach and collide. There is no difference between diffusion and brownian motion, since both describes the same thermal motion and the terms can refer to particles, atoms or molecules. The diffusion coefficient or diffusivity is a parameter that indicates the mobility of the particles, atoms or molecules. In 1905 Albert Einstein used the Fourier's heat equation to explain the Brownian motion considering the

position of the Brownian particles as a probability density function [Einstein, 1905]. He found that the diffusion coefficient was given by $D = k_B T / f$ where $k_B T$ was the thermal energy and f was a function of the friction coefficient of the particle. Stokes studied the mobility of spherical nanoparticles and described $f = 6\pi\eta R$, where η was the viscosity of the media and R was the radius of the particle [Lindgren, 1999]. The Stokes-Einstein equation (eq. 1.8) is used to define the self-diffusion coefficient for translation motion of isolated Brownian spheres [Kholodenko and Douglas, 1995],

$$D = \frac{k_B T}{6\pi\eta R} \tag{1.8}$$

where, k_B is the Boltzmann constant, T is the temperature of the system, v is the viscosity of the media and R the radius of the spherical particle. As we describe in chapter of Characterisation Methods (section 2.6), the rotational Brownian motion $D = k_B T / 8\pi\eta R^3$ permits to determine the radius of a spherical particle under from diffusion measurements under an external field. We should mention that the diffusion equation is an approximation of the the time evolution of the probability density function of the particle under Brownian motion. For more realistic studies, the Langevin function is used, which gives the time evolution of the position of a Brownian particle under taking into account the brownian motion, an inertial motion, driving forces and drag forces [Lemons and Gythiel, 1997].

Electrostatic forces avoid the collision of particles due to Brownian motion. The repulsive potential depends on the particle charge, size and the concentration of mobile ions. In order to study this potential, the electrical double layer model is used [Lyklema, 1995].

In 1879, Helmholtz developed the mathematical treatment of a single layer assuming a similar behaviour than a simple capacitor. Counter-ions (opposite charge) strongly bounded on the surface as immobile charges and balanced the charge of the electrode surface. The capacitance of two planar surfaces is equal to $C = \epsilon/4\pi d$, where d is the distance between surfaces and ϵ the dielectric constant of the media. That implied the potential was independently of the distance.

Gouy (1910) and Chapman (1913) pointed out that the potential decreased exponentially with distance and associated this behaviour with the diffusion of the counter-ions, and hence introducing the concept of a diffuse double layer. The concentration of counter-ions was greater at the electrode surface and decreased exponentially until a homogeneous distribution appeared in the bulk electrolyte, c_i^0, following a Boltzmann distribution, $c_i(z) = c_i^0 \exp(-\Delta E_i(z)/k_B T$, where $\Delta E_i(z)$ is the electrostatic energy of ion i, $e_i V_i(z)$ referenced to the bulk energy [Anderson, 1999, Hellebusch et al., 2010]. The Poisson's equation describes the electrostatic potential related to a charge density ρ, $\Delta V = -\rho/\epsilon$. The combination of Poisson's equation and the Boltzmann distribution, results into the Poisson-Equation equation 1.9 [Hunter, 2001],

$$\epsilon \frac{d^2 V(z)}{dz^2} = -\sum_i e_i C_i^0 \exp\left(\frac{e_i V_i(z)}{k_B T}\right) \tag{1.9}$$

This model, however, failed in the explanation of highly charged surfaces, assumed an invariant dielectric constant and considered that ions behaved as point charges as well as that there were no limitations for the ions in their approach.

In 1924, Stern combined both models, Helmholtz and Gouy-Chapman, and proposed the electrical double layer model, consisted in an inner layer, where interactions are strong considering adsorption of ions onto the surfaces (Helmholtz or Stern layer), and an outer layer, where the potential decays exponentially with distance [Chang, 2000]. In order to calculate the potential as a function of the distance, for low charged spherical particles (less than 25 mV) the Debye-Hückel approximation is applied, yielding the following expression,

$$V(r) = V_d \frac{a}{r} e^{-\kappa(r-a)} \tag{1.10}$$

where a is the radius of the charged particle and κ is defined as $\kappa \equiv \sqrt{\frac{\rho e^2}{\varepsilon k_B T}}$. The associated length $\lambda_D = 1/\kappa$ is called the Debye length. Considerations of the particle radius, larger or smaller than the Debye length, will be very useful for theoretical calculations.

Unfortunately, the potential at the Stern layer, V_d was not possible to be measured. However, a very useful experimental parameter that can be measured is a potential located between the solvated layer and the bulk liquid known as zeta potential ζ [Hunter, 1981]. Fig. 1.7 shows a schematic drawing of the surface potential (negative surface charge of the particle), the stern potential and the zeta potential ζ of a particle [Tscharnuter, 2000].

The responsible for the long-range attractive interaction is associated to van der Waals forces. In 1873, van der Waals realised that real gases do not obey the ideal gas law, $pV = nRT$, he pointed out that intermolecular attraction was ignored and some corrections terms of the pressure (due to attraction of molecules) and volumes (due to the finite size of molecules) should must be done. The equation proposed was (eq. 1.11) [Gosh, 2009],

$$\left(p + \frac{n^2 a}{V^2}\right)(V - nb) = nRT \tag{1.11}$$

where a and b are different constants related with short-rage repulsive forces and long-range attractive forces.

Intermolecular forces were studied separately by different people, dispersion forces were described by London in 1930, dipole-dipole interaction by Keesom in 1912, but the total intermolecular attractions are known as van der Waals forces [Clarck, 2007]. Total van der Waals interaction contains three terms which contribute to the the total long-range interaction between polar molecules [Israelachvili, 2011b]: the induction force due to interaction between two

Figure 1.7: Schematic drawing of the electrical double layer.
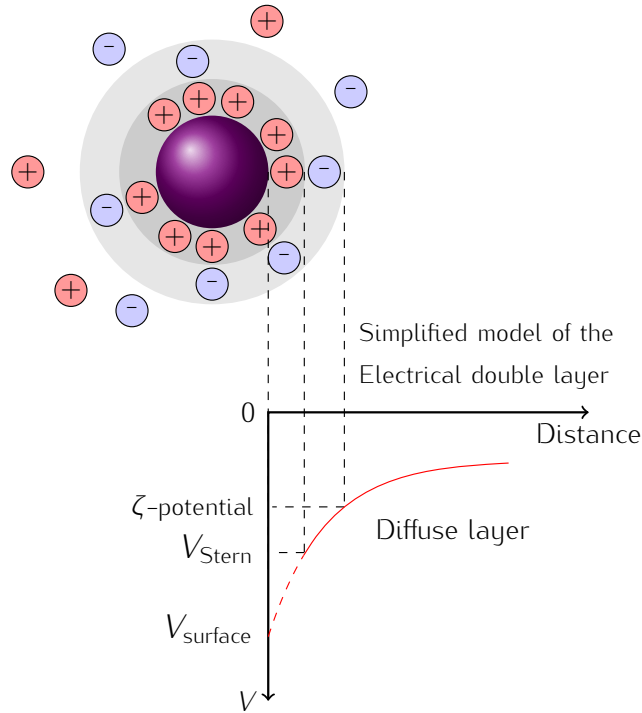
induced dipoles (London dispersion force), the orientation force due to the interaction between two permanent dipoles (Keesom orientation force) and the dispersion force due to the interaction between one permanent dipole and one induced dipole (Debye induction force), eq. 1.12.

$$U_{VDW} = -C_{VDW}/r^6 = -[C_{ind} + C_{orient} + C_{disp}]/r^6 \qquad (1.12)$$

The most widely used approximation of van der Waals potential to describe the attractive interaction between two particles is based on the attractive London interaction calculated considering two infinite planes separated at a distance d,

$$U_R = -\frac{A_H}{12\pi d^2} \qquad (1.13)$$

where A_H is the Hamaker constant, which contains the information of the dielectric properties of the intervening medium. The van der Waals interaction depends on the shape of the two bodies, Parsegian [Parsegian, 2005] presented in his book the van der Waals interaction energies corresponding for two spheres with different radii, a sphere and planar half-space, two cylinders among others.

The DLVO theory describes the potential of a particle as a sum of two contributions, the attraction potential due to the van der Waals forces and the repulsion potential due to the electrostatic repulsions. An example of a DLVO potential in comparison with the thermal energy

is depicted in Fig 1.8. Depending on the shape of the DLVO potential, one can predict the colloidal stability. If the barrier potential is negative, there is a fast coagulation. On the contrary, if the potential barrier is high enough, the colloid is stable. If there is a second minimum and the potential barrier is still high, there colloid is kinetically stable, and if the potential barrier is small, there is slow coagulation.

Figure 1.8: DLVO theory describes the total potential as a result of the sum of the attraction potential and the repulsion potential.
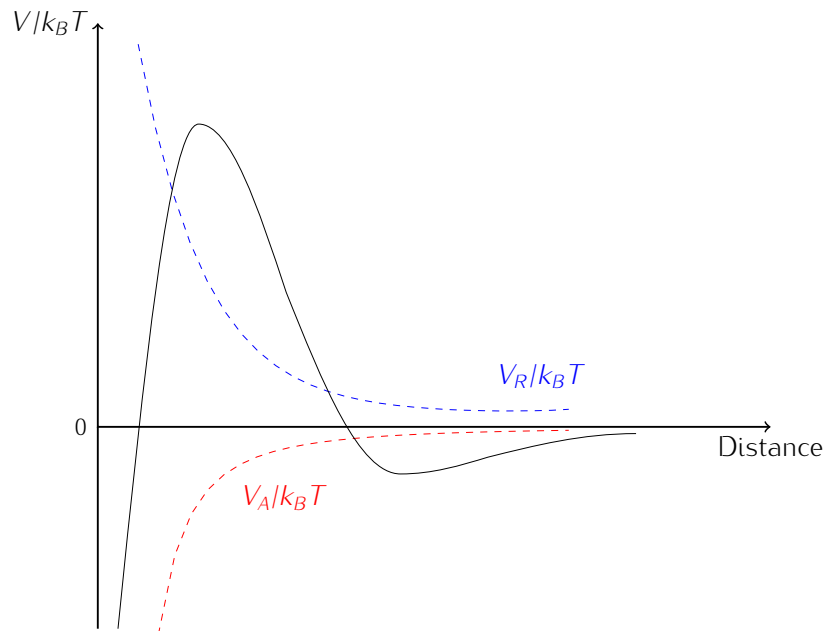
1.2   Particle formation and growth

The main techniques for the production of carbon–encapsulated magnetic nanoparticles are based on a gas–to–solid condensation process, which consists of vaporising a source material until reaching a supersaturation regime where vapour condensates into small nanoparticles. The establishment of supersaturation is a requirement to generate nanoparticles. We need to work under conditions in which the pressure of vaporised atoms of the material (atomic cloud) is greater than its vapour pressure at the temperature maintained in the cloud. These conditions can be achieved by cooling of the atoms/clusters using for example a cooler gas (in plasma reactors) or by chemical reactions initiated by the increasing of temperature (in laser, flame reactors) [Kruis et al., 1997].

The nanoparticle formation process is separated into several steps: supersaturation, nucle–ation, particle growth (crystallisation), particle coagulation and coalescence (Fig. 1.9) [Gustch et al., 2002].

Figure 1.9: Main steps present in the formation of nanoparticles.
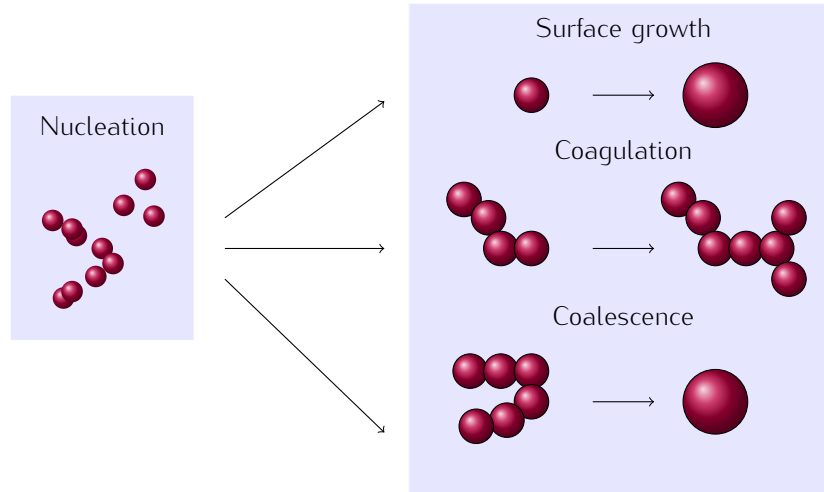
1. **Nucleation**: Nucleation is the process where metastable nuclei are formed by the collision of vaporised atoms. The nucleation process can be *homogeneous* or *heterogeneous*. The *homogeneous nucleation* is characterised by the formation of nuclei in a homogeneous system, both reactant and surroundings are the same phase. The *heterogeneous nucleation* is more likely to occur, since nuclei are formed in preferable sites (heterogeneities such as impurities, surfaces), which require less energy to overcome the particle barrier formation.

In this section, the homogeneous nucleation is described following the classical theory developed by Becker and Döring [Becker and Döring, 1935]. Some controversies exist on some assumptions made in the classical theory, for instance translational and rotational energies of the droplet as it moves through the system might be significant contributions in the energy formation of the nanoparticle [Lothe and Pound, 1962, Moody and Attard, 2002]. However, for practical purposes, classical nucleation theory is the only means of predicting nucleation rates and critical cluster sizes [Vehkamäki, 2006].

The classical expression for the homogeneous nucleation rate depends on the supersaturation ratio, S, which is defined as the relation between the partial pressure of the gaseous reactant p_i, and the corresponding saturated vapour pressure $p_s(T)$ (eq. 1.14). When S is larger than unity, the nucleation process may occur [Chazelas et al., 2006].

$$S = \frac{p_i}{p_s(T)} \tag{1.14}$$

The free energy ΔG_j required to form a new spherical phase nucleus consisting of j atoms with radius R_j is determined by two terms [Pomogailo and Kestelman, 2005] (eq. 1.15).

The first term (ΔG_{Vj}) is related to the creation of volume due to the difference in the chemical potential between the new phase nucleus (n) and the environment phase (e), $\Delta\mu = k_B T \ln S$, and the second term (ΔG_{Sj}) is the energy due to the formation of a new surface.

$$\Delta G_j = \Delta G_{Vj} + \Delta G_{Sj} = -\frac{4\pi}{3V_a}R_j^3\Delta\mu + 4\pi R_j^2\gamma \tag{1.15}$$

$$\Delta G_{Vj} = -j\Delta(\mu_e - \mu_n) = -j\Delta\mu = -\frac{4\pi}{3V_a}R_j^3\Delta\mu = -\frac{4\pi}{3V_a}R_j^3 k_B T \ln S \tag{1.16}$$

$$\Delta G_{Sj} = 4\pi R_j^2\gamma \tag{1.17}$$

where k_B is the Boltzmann's constant, T the temperature in the environment phase, S the supersaturation ratio, V_a is the atomic volume of the nucleus, and γ is the specific free surface energy.

2. **Particle growth (crystallisation)**: The nuclei formed during nucleation process become stable when their critical energy barrier is overcome ΔG_{cr}. The value of the critical size for a stable nucleus R_{cr} is determined by $d(\Delta G)/dR = 0$ (eq. 1.18). Table 1.1 shows some examples of critical radius R_{cr} to form stable metal crystallites.

$$R_{cr} = \frac{2\gamma V_a}{\Delta\mu} = \frac{2\gamma V_a}{k_B T \ln S} \tag{1.18}$$

The profile of the free Gibbs energy for a homogeneous nucleation and particle growth is depicted in Fig. 1.10. The two thermodynamic contributions of volume and surface terms define a threshold in a critical size which establishes the minimum size of the nanoparticle.

3. **Particle coagulation** is the mechanism that occurs at high particle concentrations when particles are randomly distributed and collide due to Brownian motion. This collision promotes the aggregation of nanoparticles due to strong adhesive forces or chemical bonds, among others [Gustch et al., 2002]. In plasma reactors, the residence time, which is the time that nanoparticles are located in the plasma region, determines the level of aggregation. To avoid aggregation, it is important that the residence time was as short as possible [Kruis et al., 1997].

4. **Coalescence** is another kind of agglomeration, but in this case, implies nanoparticles with similar sizes that merge into a bigger particle.

There is also another mechanism, called **Ostwald ripening**, which is observed during the formation of nanoparticles when there is an ensemble of nanoparticles with slightly different

Table 1.1: Several metal examples of critical nucleus R_{cr} and the corresponding number of constituent atoms j_{cr} during metal crystallisation from the melt [Pomogailo and Kestelman, 2005].

Metal	$\gamma \cdot 10^7$ [J / cm^2]	$V_a \cdot 10^{-23}$ [cm^3]	R_{cr} [nm]	j_{cr}
Fe	204	1.21	1.17	553
Co	234	1.12	1.07	457
Ni	255	1.13	1.07	453
Cu	177	1.21	1.14	512
Au	126	1.75	1.27	483
Al	93	1.67	1.23	466

Figure 1.10: Schematic representation of the free energy as a function of nanoparticle size for a homogeneous nucleation and growth process.
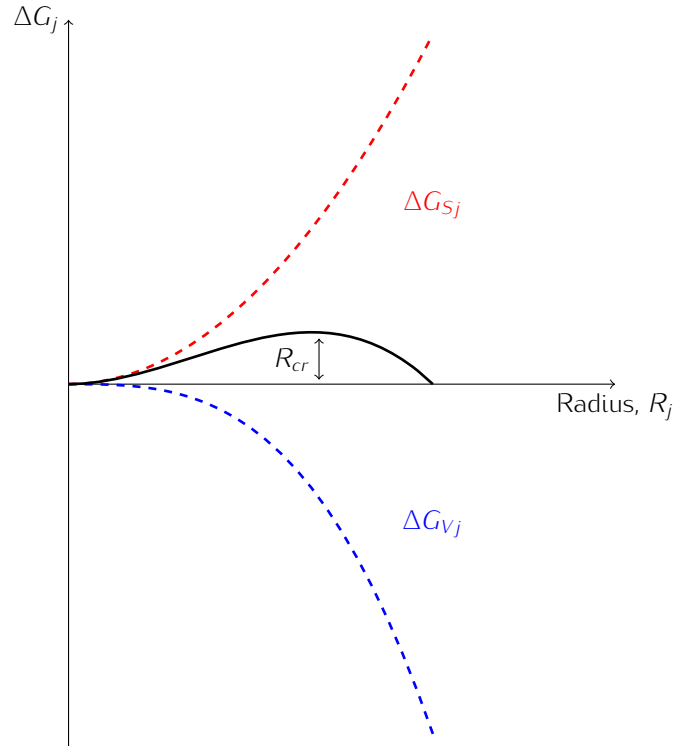
sizes [Lifshitz and Slyozov, 1961]. This mechanism favours the formation of larger nanoparticles by the exchange matter produced by the atom transfer from smaller crystals to bigger ones. It can occur in solid, liquid or gas phase [Mokari et al., 2005, Hornyak et al., 2008].

1.2.1   Carbon coating formation mechanism: state of the art

There are several theories about the carbon–coating formation in carbon–encapsulated magnetic nanoparticles. Many of these theories are developed from the suggested mechanisms about the formation of carbon nanotubes (CNTs), since typically they use metal nanoparticles as cata-lysts for their growth [Ding et al., 2004]. However, there are different mechanism explanations depending on the deposition method used to produce CNTs [Laurent et al., 1998, Kumar, 2011].

In case of the CVD method, the most popular theory for the explanation of CNTs growth is the vapor–liquid–solid (VLS) model proposed by Baker and co–workers in the 1970s [Baker et al., 1972, Baker, 1989]. According to this model, the metal nanoparticle acts as a catalyst for the decomposition of hydrocarbons (carbon source) at lower temperatures than the spontaneous required. The carbon atoms then diffuse through the nanoparticle (in liquid state) and due to a carbon supersaturation and a temperature gradient (caused by the exothermic decomposition), the carbon precipitates on the substrate and causes the formation and growth of carbon fila-ments. Oberlin and co–workers. [Oberlin et al., 1976] proposed another model where the carbon diffuses on the surface of the catalytic particle and dissociates at the contact angle between the particle and the surface to form the tubes. Ding et al. [Ding and Bolton, 2006] showed by thermodynamic analysis that a metal particle only needs to be highly carbon supersaturated to nucleate carbon islands (Fig. 1.11).

For the arc–discharge plasma method, Saito et al. [Saito et al., 1994] proposed a growth model where carbon and metal catalysts are evaporated together and as the catalytic particles cool, the carbon atoms are segregated onto the surface because of the decreasing of solubility of carbon with the decreasing temperature. The addition of carbon atoms from the vapour phase helps the growth of tubular structures.

Regarding the formation of carbon–encapsulated magnetic nanoparticles by arc–discharge plasma methods, there are several hypotheses.

Saito and co–workers [Saito, 1995] explained that there is correlation between the vapour pressure of metal and the graphite encapsulation. They studied a wide range of composite materials and found that volatile elements are not encapsulated. Based on those observations, they proposed that NPs grow at the cathode with a liquid core coated by a graphite shell, which then segregates and solidifies. For this reason, volatile elements are not encapsulated since they hardly condense on the cathode and diffuse far away from where carbon condenses.

Majetich and co–workers [Majetich et al., 1995, Scott et al., 1995] suggested that firstly magnetic material and carbon are atomised in the plasma. They collide and nucleate into clusters in the supersaturated vapour until they grow to their characteristic sizes. Finally, particles are deposited on surfaces within the reactor, and by phase segregation the carbon coating on the particle exterior is formed. Moreover, they reasoned that size distribution of the samples depends on the steepness of the cooling curve that nanoparticles follow during their

growth (Fig. 1.12).

Seraphin and co-workers [Seraphin et al., 1996] studied 20 elements as metal source in order to study the carbon shell formation. They separated the elements into four categories depending on their tendency to form carbides. They observed that enthalpy of the carbide formation has an important role in the carbon encapsulation, since if the carbide is not formed, then the encapsulation is not observed and the opposite, if the formation of carbide is too aggressive, there is no carbon shell. However, there are some exceptions for some element behaviours.

Recently, Bystrzejewski and co-workers [Bystrzejewski et al., 2009] thought that it was improbable to form α-Fe from the vapour phase under a dominating presence of carbon. They expected the NPs to emerge from liquid droplets and then solidify in the cold zone. Finally, these liquid droplets are covered by a graphite layer of carbons in the vapour phase.

Figure 1.11: Graph of the first steps of SWNTs nucleation and growth obtained by molecular dynamics simulations (Figure from Ref. [Ding and Bolton, 2006]).
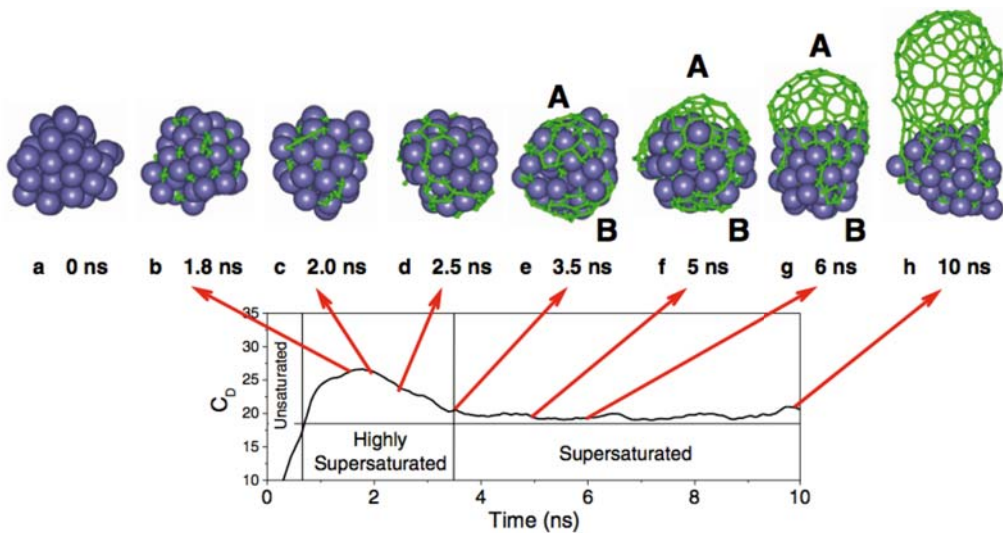
Despite all the suggested models previous mentioned, there are still some disaccording points, for example, the state of the catalytic particle (vapour, liquid or solid), the kind of carbon diffusion (volume or surface), and so on. More research is required for a clear understanding of these mechanisms.

Figure 1.12: Formation of the carbon coating of CEMNPs by phase segregation during the cooling of the liquid metal nanoparticle (figure adapted from Fig. 3 of reference [Majetich et al., 1995]).

Carbon + Metal atoms

Carbon segregation during cooling
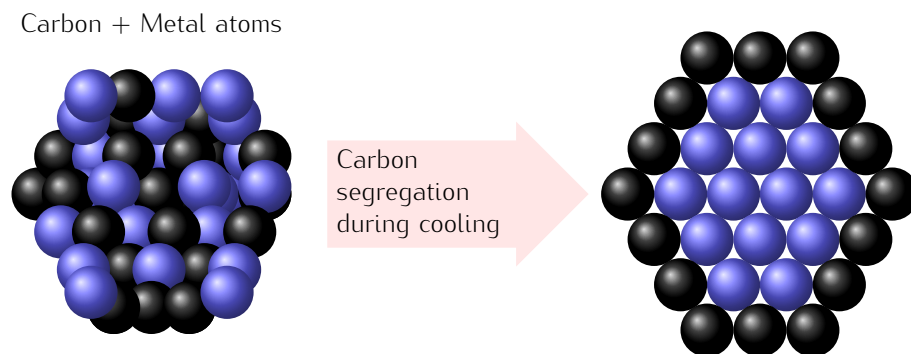
1.3   Fabrication techniques

There are two kinds of fabrication methods to produce nanostructured materials: the *top–down* and the *bottom–up* manufacturing processes. The *top–down* method consists of the formation of new nanomaterials from bulk materials that are reduced until the desired nanostructure is achieved. The *bottom–up* is characterised by the synthesis of nanomaterials from smaller starting subunits that react with chemical or physical forces and form the desired nanostructures. There is also the *hybrid fabrication* that is a combination of both, *top-down* and *bottom–up*, processes.

We will focus on the techniques for the production of carbon–encapsulated magnetic nanoparticles. Most of this technology came from the first techniques used to generate carbon nanostructures, such as, MWCNTs, SWCNTs or fullerenes. The most common methods used nowadays are: arc–discharge plasma (ADP), chemical vapour deposition (CVD), laser ablation and spray pyrolysis.

These methods are based on the gas phase synthesis, which allows the generation of core@shell nanostructures in a single step, thus avoiding the oxidation and chemical degradation of the magnetic cores. This is an advantage in comparison with other techniques (sol–gel, precipitation methods) commonly used to produce inorganic (silica, gold) or organic (polymers) coatings, which require several steps and even the combination of different methods to generate first the magnetic core and afterwards the corresponding encapsulation [Tartaj et al., 2003]. In addition, these techniques require less chemical species and process steps, obtaining a high quality product with high purity, environmentally friendly, and solubility problems of precursors are avoided. However, in comparison with other methods based on liquid–phase synthesis, some nanoparticle aggregation can occur and the yield is lower and thus, increasing the cost for production.

1.3.1 Arc Discharge Plasma (ADP) method

The ADP method is the first method used for the production of carbon nanotubes [?] and is widely used as well as for the synthesis of carbon-encapsulated magnetic nanoparticles [Bystrzejewski et al., 2005, Bera et al., 2006, qiang Wei et al., 2011, Aguiló-Aguayo, 2007]. This method consists of forming a high-temperature plasma between two electrodes facing each other and connected to a DC, AC or RF power source (Fig. 1.13). A high-energy spark is produced between the close electrodes and plasma is formed due to the ionisation of a gas supply consisting mainly of inert gases (He, Ar). One of the electrodes provides the metal source and due to the high temperature of the plasma (about 3000 K or higher), the vaporisation of precursors is achieved. The carbon source can be supplied by electrodes made of graphite or the carbon generated from the decomposition of inserted reactive gases. In this technique, the inert atmosphere, the high temperatures used and the high cooling rates assure the production of high purity nanoparticles with good surface activity and very small sizes due to the very short residence times of the nuclei formed in the plasma. However, the uniformity of the cooling rates could deteriorate the uniformity of the nanoparticles. This is the technique used in our experimental set-up.

Figure 1.13: Schematic drawing of a ADP reactor.
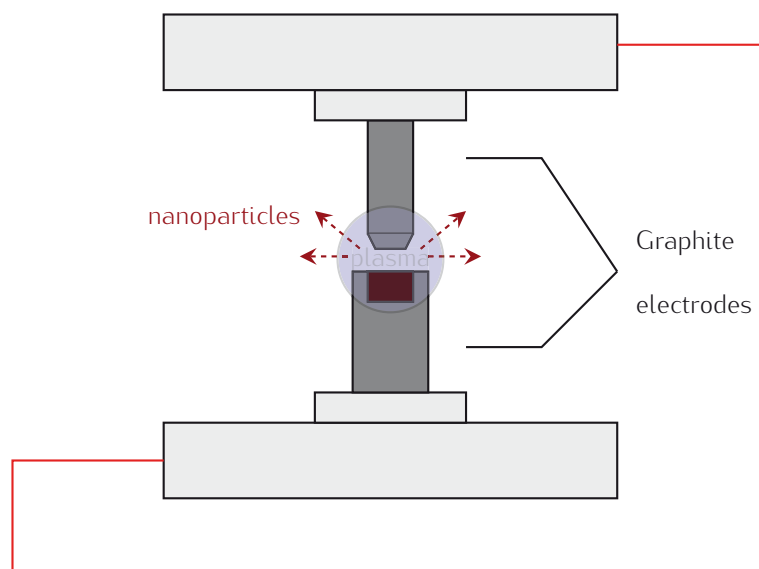
1.3.2 Chemical Vapour Deposition (CVD) method

The CVD reactor is based on a horizontal quartz glass tube located inside a furnace heated at temperatures around 600-1000° (Fig. 1.14). The synthesis of nanoparticles commonly consists of two steps. First, the magnetic precursor is introduced in the controlled-temperature furnace in a liquid, gas or solid state and decompose. Then, a gas mixture of the carrier gas (Ar, N_2) and the

carbon gas supply (xylene, acetylene) is introduced into the furnace at temperatures in the range 600–1000° in a continuous flow about 50-800 sccm. The reaction chamber is kept at pressures in the range 40–100 Pa. Nanoparticles are collected from the walls of the reaction chamber. CVD produces highly dense and pure materials, the deposition temperatures are relatively low which implies a reasonable processing cost, and a wide range of chemical precursors is available. However, it is difficult to achieve a a sufficiently high yield of nanoparticles for commercial use [Liu et al., 2001, Choy, 2003].

Figure 1.14: Experimental setup of the chemical vapour deposition technique, image modified from [Marikani, 2009].
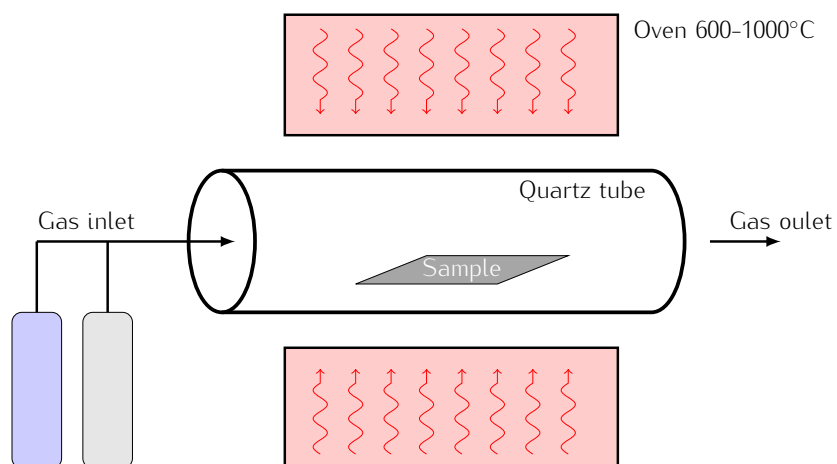
1.3.3   Laser ablation method

This process was first developed at Rice University for the production of MWCNTs [Guo et al., 1995]. The apparatus consisted of a quartz tube heated in a temperature-controlled furnace, of about 1200° (Fig. 1.15a). A graphite target was placed in the furnace and heated to outgas the target. Afterwards, a Nd:YAG laser irradiated the graphite sample in an uniform way providing 10 ns, 250 mJ pulses at 10 Hz . The resulting product was dragged out of the furnace by a carrier inert gas (Ar).

In order to produce nanoparticles with various compositions, such as carbon–encapsulated magnetic nanoparticles, besides the use of laser ablation in a flow reactor [Dumitrache et al., 2004], the method was also modified to be used in liquid medium [Yang, 2007, Park et al., 2008, Kwong et al., 2010, Zeng et al., 2012]. A pulsed laser irradiates a bulk target (cobalt, iron) located inside a container filled with the liquid carbon source (i.e., toluene) or irradiates a solution based on metalocene powder (ferrocene, nickelocene, cobaltocene) in the liquid carbon source (i.e., xylene). Nanoparticles can be collected using a magnet or directly obtained in a colloidal solution (Fig. 1.15b). The shape and evolution of the plasma plume controls

the fabrication of nanoparticles. Complex nanoparticles can be obtained due to the chemical reactions of the target atoms with the environmental molecules. In addition, laser ablation in liquid avoids agglomeration of nanoparticles. However, nanoparticles are produced in a range of 10–100 nm, larger nanoparticles are not possible to fabricate, and it is a costly technique, since requires expensive lasers and has a high power requirement.

Figure 1.15: (a) Schematic diagram of a pulsed laser ablation (PLA) system and (b) in the liquid medium (PLAL).
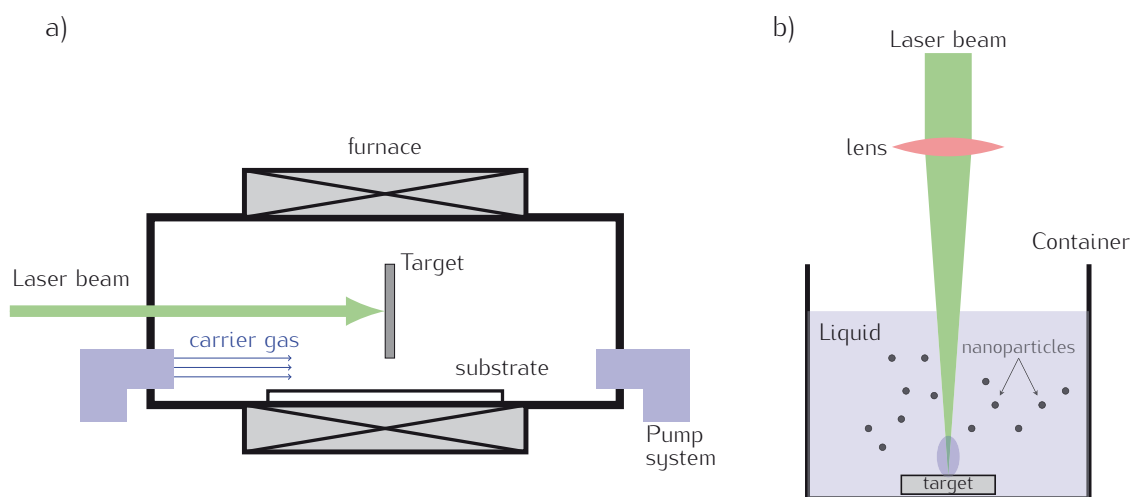
1.3.4   Spray pyrolysis method

This technique is also known as aerosol thermolysis, evaporative decomposition, plasma va- porisation of solutions or aerosol decomposition [Jackson and Hargreaves, 2009]. This method consists of atomising a reaction solution by means of a spray nozzle containing a capillary tube that has an inner diameter less than 0.4 mm. The solution supplies the carbon and the magnetic materials sources, for instance ethanol (C_2H_6O) as carbon source and iron pentacar- bonyl ($Fe(CO)_5$) as iron precursor. The solution precursor is carried by a gas into the reactor, where the decomposition of the precursor undergoes in the hot zone of a electrical furnace heated at temperatures around 500–900° (Fig. 1.16). Nanoparticles are collected at the bottom of the reactor. This method offers the possibility to use different type of precursors in gas or liquid phase and the amount of the resulting nanoparticles can be determined by controlling the flow of the precursor. However, hollow structures or fractured particles can be obtained and there is some difficulty of scaling-up the production due to the high amount of the required solvents [Wang et al., 2007b, Jung et al., 2010, Atkinson et al., 2011].

We should mention that other techniques employ a combination of the methods described above, such as laser–assisted chemical vapour deposition (LCVD) [Westberg et al., 1992, Widenkvist

et al., 2011] or arc–plasma assisted CVD [Li et al., 2009b] or laser–assisted spray pyrolysis [Jäger et al., 2006].

Figure 1.16: Experimental setup of a spray pyrolysis technique, image modified from [Wang et al., 2007a].
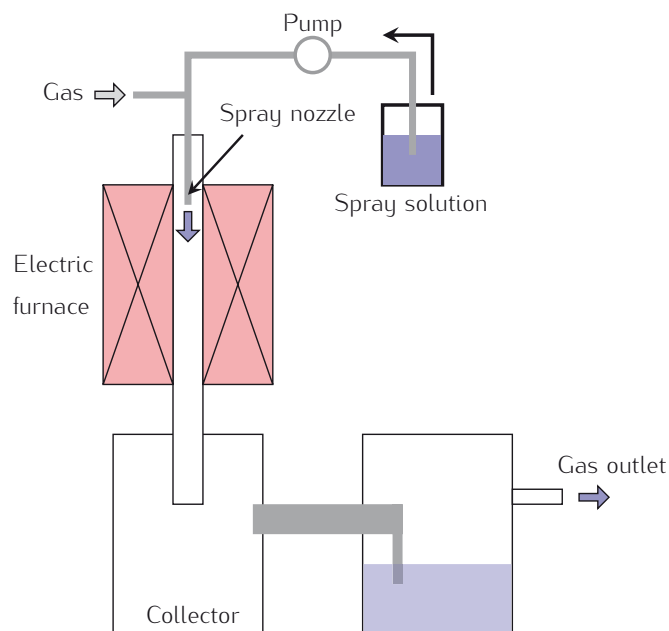
1.4   Applications of Fe@C NPs

Core–shell Fe@C nanoparticles show a wide range of applications due to the whole character-istics from both, magnetic behaviour of the tiny Fe cores and their carbon–shell protection. Their applications covered a wide range of different fields, from biomedicine, electronics, automotive, environmental, military to agriculture and food industry. In the following, we will describe some of the most important applications in each field.

1.4.1   Biomedicine field

The controlled generation of nanoparticles has been very important specially for biomedical applications, since for the first time we could control objects with sizes of 1-100 nm range com-parable to biological entities being able to interact with biological structures. The size as well as novel properties which are presented in nanoparticles spread their use in several applica-tions, such as drug delivery (labelling and therapy), gene delivery (transfection), diagnosis and monitoring (disease markers), diagnosis (devices and labelling) and detection (imaging) [McNeil, 2005].

Magnetic nanoparticles can be used as magnetic biosensors. Magnetic nanoparticles are used to study the Brownian relaxation when biomolecules bind to the surface of the particles [Imego, 2005]. Magnetic nanoparticles are also used as electrochemical biosensors to detect biomolecules and cells. The use of magnetic nanoparticles in DNA and protein sensors provides the magnetic separation by isolating cells and removing unwanted impurities, and hence a highly sensitive and reliable detection technology [Hsing et al., 2007].

Carbon–encapsulated iron nanoparticles are used as local heat sources in hyperthermia in order to destroy tumour cells as a localised therapy [Taylor et al., 2010]. When an AC magnetic field is applied with a specific frequency, magnetic nanoparticles generate heat due to the magnetic losses produced during the magnetisation reversal. There are different mechanisms of magnetic losses depending on the magnetic properties of the nanoparticles. The magnetic losses from superparamagnetic nanoparticles are due to Néel or Brown relaxation, whereas in ferromagnetic nanoparticles the heating is caused by hysteresis. In addition, there is a torque moment associated with the remanent magnetisation due to the rotating magnetic field, and thus frictional looses in viscous suspensions are also produced [Hergt et al., 2006].

Superparamagnetic nanoparticles are employed as well as contrast agents in Magnetic Resonance Imaging (MRI). These nanoparticles provide a local magnetic field, which interacts with the hydrogen nucleus in water molecules in the body and thus, achieve a contrast enhancement. The signal of the MR image is obtained from the proton density, the concentration of protons that comes from water and macromolecules, such as proteins, fat and so on; the T_1 longitudinal relaxation time that can be affected by the interactions of spins with the lattice; the T_2 transversal relaxation time that is determined by the spin–spin interactions; and finally the flow, the high arterial blood can introduce some noise to the final signal. The contrast and signal intensity are determined by the T_1 and T_2 relaxation times [Hesselink, 2012]. Seo and co–workers [Seo et al., 2006a] used FeCo@C nanoparticles in MRI and observed a maximum magnetic coupling to surrounding spins and hence, exhibiting higher T_1 and T_2 relaxivities than conventional Gd and iron–oxide–based contrast agents opening new possibilities in MRI.

1.4.2   Electronics

Magnetic nanoparticles showing a thermally blocked state due to their high remanent magnetisation, they are used in data storage systems such as mobiles, smaller devices which requires high storage density. Magnetic nanoparticles spontaneously self–organise on a surface providing several terabits per square centimetres much more larger than the storage density of 35 gigabits cm^{-2} in advanced computer hard drives or larger than the 0.4 gigabits cm^{-2} in DVDs [Reiss and Hutter, 2005, Chen et al., 2006].

Carbon–encapsulated magnetic nanoparticles show giant magnetoresistance, a property where the electrical resistance changes when an external magnetic field is applied, very useful

for new emerging electronic applications, in the so–called spintronics field, this new technology is widely used as read heads in hard drives, magnetic sensors or memory–storage cells [We-growe et al., 2002, Szczytko et al., 2007, Zhou et al., 2009].

Superparamagnetic nanoparticles are also used in credit cards since they show large magnetic moments and using a weak applied field nanoparticles can be easily magnetised [CNEM, 2012].

1.4.3 Environmental and food applications

It is observed that superparamagnetic nanoparticles show potential applications for extraction of bacterial genomic DNA from contaminated food and environmental samples [Basu et al., 2012]. In addition, carbon–encapsulated magnetic nanoparticles can be used to remove heavy metals in wasterwater. Carboxylic functional groups present on the surface benefit the adsorption of heavy metals. Zhang and co–workers [Zhang et al., 2010] observed that core@shell Fe@C nanoparticles could effectively used for environmental remediation, they adsorbed hexavalent chromium Cr(VI) with a removal percentage of 95 wt% without sacrificing the Fe cores. Sun and co–workers [Sun et al., 2006] investigated that Fe@C nanoparticles are a good adsorbent for the removal of pollutants in water by magnetic separation. Lai and co–workers [Lai et al., 2009] showed that carbon–coated iron nanoparticles could be successfully employed in biosensors for the amperometric determination of H_2O_2, which is very suitable in fields such as food, industry, environmental protection or clinical control.

1.4.4 Mechanical applications

The outer carbon layers of the carbon–encapsulated magnetic nanoparticles are very suitable for several mechanical applications due to their good tribological properties, offering wear-resistance, low–friction and good lubricant [Kramer, 2007, Kovács et al., 2004]. This kind of nanoparticles can act as solid lubricants for brake discs, to reduce corrosion in turbo housings and exhaust manifolds or in diesel engine blocks [Foundry, 2012].

Part II

Nanotools

2
Characterisation methods

In this chapter, we will describe the characterisation techniques used to investigate the morphological, compositional and structural properties as well as the magnetic behaviour of our samples based on carbon–encapsulated iron nanoparticles.

Microscopy observations, such as high–resolution and transmission electron microscopy (HRTEM, TEM) were mainly used to observe the crystalline structure and determine the size distributions of the iron cores. Total nanoparticle sizes, including the carbon shell, were characterised by scanning electron microscopy (SEM) and atomic force microscopy (AFM). Analytical techniques, such as energy dispersive X–ray microanalysis (EDX) or electron energy loss spectroscopy (EELS) were used to determine the chemical composition of the nanoparticles and detect the presence of non–desirable elements. The crystallinity of the iron cores was identified by selected–area–electron diffraction (SAED) and X–ray diffraction (XRD). The structural order/disorder of the carbon encapsulation was determined by Raman. Elemental analysis (EA) based on the complete and controlled combustion of carbon was used to better quantify the carbon content present in the nanoparticles. Size distributions and colloidal stability of nanoparticles dispersed in aqueous solution were also determined by photon correlation spectroscopy (PCS), analytical disc centrifuge (CPS) and zeta (ζ) potential measurements. Finally, magnetic properties (hysteresis loops and Zero–Field–Cooled and Field–Cooled responses) were investigated by using superconducting–quantum–interference–device (SQUID) magnetometer. In addition, optical emission spectroscopy (OES) was applied to characterise in situ the arc–discharge plasma in order to measure its temperature and identify the excited species which might be present.

2.1   Electron microscopy

During 1930s, electron microscopes were developed to overcome resolution limitations of light microscopes (200 nm). Nowadays, electron microscopes are important scientific instruments, widely used to observe and characterise materials from microscale to nanoscale range by means of sample irradiation with high–energy electron beam.

As a consequence of the electron beam interaction with the specimen, different types of elastic and inelastic scattering can occur (Fig. 2.1) making possible to collect different information about the sample: topography (surface features), morphology (shape and size), composition or the crystalline structure [Park, 2008].

Figure 2.1: Schematic representation of electron–specimen interaction. To detect transmitted electrons, specimen thickness has to be less than 100 nm.
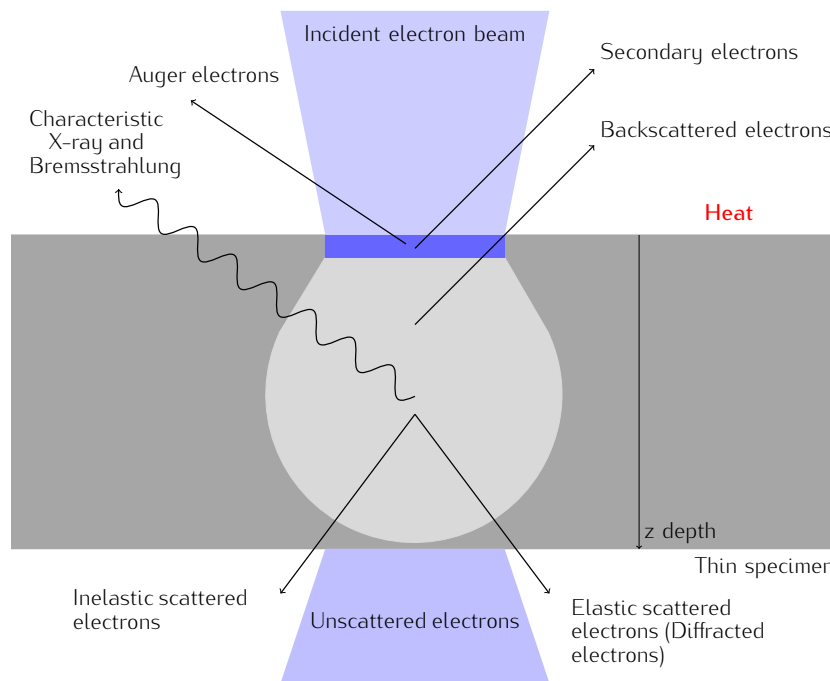
The most widely used electron sources are based on the thermionic emission in tungsten or LaB_6 cathodes, and the field emission.

The thermionic emission consists of heating up the material at temperatures high enough to overcome the work function and extract electrons from the cathode. In the electron gun, electrons are accelerated by applying voltages about 20 to 400 kV during operation. The tungsten filament bent in a hairpin shape with a V–shaped tip is heated up to 2700° and provides high current densities about $5 \cdot 10^4 \, Am^{-2}$. When brightness is increased, the filament is abruptly consumed. However it is relatively non–expensive and its properties are well understood. The LaB_6 cathode

requires lower temperatures than tungsten to overcome its work function (about 1500 K). As a consequence of this, the lifetime of the source is longer and it provides higher brightnesses (more than 10 times) at the same accelerating voltage and density currents. However, the material is very chemically reactive and can be only operated in good vacuum [Joy et al., 1986, EMS, 2011].

The field emission gun (FEG) is based on another principle. The cathode is commonly made of tungsten and has a rod shape with a very sharp point at the end (about 100 nm or less), when the accelerating voltage is applied, high electric fields are produced in this sharp point ($> 10^7$ V/cm) and electrons can pass through the barrier by tunneling effect and leave the cathode without any thermal energy [Joy et al., 1986] The field emission guns are very expensive, but provide higher brightnesses (1000 times greater) and greater current densities ($1 \cdot 10^6$ Am^{-2}) and thus, are commonly used for high resolution imaging and analysis [FEI, 2012].

2.1.1   Scanning Electron Microscopy (SEM)

Scanning Electron Microscope (SEM) can provide topography, morphology, composition and crystallographic information about a sample depending on specific detectors. We should mention that SEM is routinely used to obtain high–resolution images of the shape of objects, showing features down to 20 nm in size.

The equipment recorded topography information by the collection of secondary electrons (SE). When an incident electron beam with low energy 100 eV passes near the specimen atoms, SE (50 eV or less) are generated by the ejection of electrons from the lower energy shell (K–shell) or by substantial energy–losses due to collisions with the nucleus. Its low energy makes that they can only exit from the surface and thus, provide information about the topography of the sample. The collector consists of a photomultiplier, that recorded the radiation generated by the SE when they are accelerated onto a scintillator [Reimer, 1998].

In addition, backscattered electrons (BS), produced when incident electron is scattered 180°, provide information about the composition of the sample (the contrast changes depending on the atomic number of the element) as well as the surface topography. Diffracted backscattered electrons (EBSD) can be used to determine the crystal structure of the sample. An electron dispersive X–ray detector (SEM–EDX) installed in the microscope column can provide quantitative information about the composition of the sample (see subsection 2.1.4).

Samples in SEM must be prepared to have a conductive surface so electrons can move from surface to the ground and thus, avoid the accumulation of electrons which might diverge the incident beam. A previous thin carbon or gold film can be deposited on an insulating sample to solve this problem. The maximum dimensions of the sample are usually 10 cm in length and 40 mm in length [Goldstein, 2003].

In this thesis, a HITACHI S–4100 FE operated at 20 kV at Scientific and Technological Centres of Universitat de Barcelona, was used to observe the morphology of nanoparticles (shape) and

determine primary size distributions.

2.1.2   High–Resolution and Transmission Electron Microscopy (HRTEM, TEM)

For High–Resolution and Transmission Electron Microscopy (HRTEM, TEM), samples must be prepared to have a thickness below 100 nm to allow the transmission of the electron beam. A schematic drawing about the TEM equipment is shown in Fig. 2.2. Electrons are provided by the electron gun, the emitted electron beam is confined by the condenser lens, passes through the sample, then through the objective lens and finally an image is projected onto the phosphorescent screen or CCD camera. Aberrations of the lens must be corrected during operation. Several apertures (objective and selected area aperture) are located between the sample and the screen in order to select the elastically scattered electrons that will form the image [Reimer and Kohl, 2008]. The objective aperture located at the back focal plane of the image improves the contrast of the image 2.2 and selected aperture is located at the back focal plane of the objective to obtain diffraction patterns of selected areas of the sample (see subsection 2.1.3).

Figure 2.2: Schematic drawing of a TEM equipped with EDX and EELS detectors.
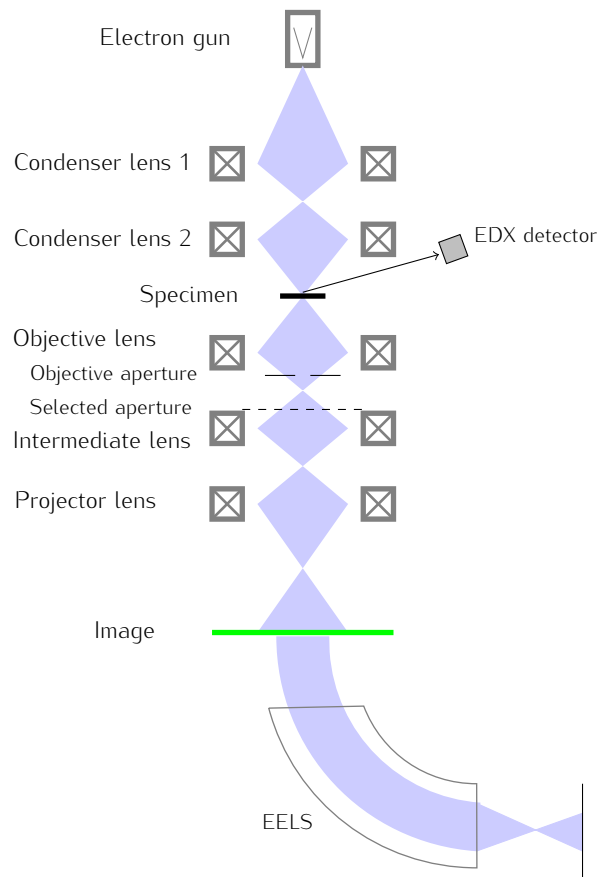
The resolution of TEM is limited to about 0.2 nm. Using HRTEM, one can identify even atomic planes. It is a powerful technique to obtain information about morphology, topography, crystal structure and composition of a specimen. There are two imaging modes: bright–field contrast (electrons scattered at angles larger than the objective aperture) and dark–field con-trast (primary beam falls on the objective aperture). Both modes may provide complementary information about crystal orientation, electronic structure, regular absorption, among others.

In this thesis, samples were deposited on holey carbon TEM grids and analysed by dif-ferent TEM equipments: a Philips CM30 operating at 300 kV, a Jeol 2100 operating at 200kV equipped with a Oxford INCAx–sight Si(Li) detector for EDX and a Jeol 2010F FEG operating at 200kV equipped with a Gatan Image Filter (GIF). Equipments provided by the Scientific and Technological Centres of Universitat de Barcelona.

Other studies were performed at University of Pittsburgh using a JEM 200 CX modified with a charge–couple device (CCD) for video recording.

2.1.3   Selected Area Electron Diffraction (SAED)

When the incident electron beam of a TEM passes through a crystalline specimen, the diffracted electrons (elastic scattered electrons) provide information about the crystal structure of the sample. The technique used to determine the crystal structure is called selected area electron diffraction (SAED or SAD). Diffraction patterns are formed in the back focal plane of the objective (selected aperture in Fig. 2.2) and the intermediate lens is focused in this plane to project a diffraction pattern onto the screen. The magnification of the pattern is controlled by the projector lenses and described by the effective camera length of the system [Goodhew et al., 2001]. In order to observe the pattern of a selected smaller area, an aperture is placed in the back focal plane (selected aperture).

The diffraction is produced due to the arrangement of atoms in the crystal (same phenomenon as X–ray diffraction, see section 2.3). Diffraction only occurs when atomic planes satisfy the Bragg condition (eq. 2.3) or in other words, when the scattering vector $\Delta \mathbf{k}$ (difference between the diffracted wave vector $\mathbf{k}'$, and the incident wave vector $\mathbf{k}$) is equal to a particular reciprocal lattice vector $\mathbf{G}$, $\Delta \mathbf{k} = \mathbf{G}$ (Ewald's sphere, Fig. 2.3).

The diffraction intensities depend on the structure factor S_G,

$$S_G = \sum_f f_j \exp\left(-i\mathbf{G} \cdot \mathbf{r_j}\right) \tag{2.1}$$

where f_j is the atomic form factor and $\mathbf{r}_j$ is vector position of each atom j. The atomic form factor depends on the electron density and distribution and measures the scattering power of jth atom in the unit cell. The reciprocal lattice vector, $\mathbf{G}$, is the sum of three integers of three primitive vectors $\mathbf{G} = hx_j + ky_j + lz_j$, known as Miller indices of a plane (hkl). Depending on the

Figure 2.3: Ewald's sphere is a graphical representation of the diffraction condition.
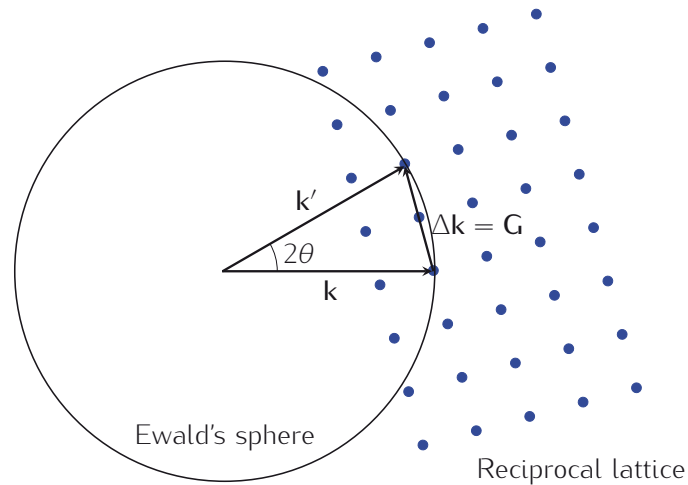
symmetry of the crystal lattice, that is to say, the crystal lattice structure (body–centered cubic, bcc; face–centered cubic, fcc; and so on), the structure presents extinction conditions where the diffraction intensities are zero [Kittel, 1971].

The diffracted patterns correspond to the Fourier transform of the periodic crystal lattice (reciprocal lattice) and can show a ring pattern (polycrystalline sample) or a spot pattern (single crystal). The acquired pattern must be indexed to a previously calculated database of patterns and thus, crystalline information of the specimen (orientation of the crystal, crystalline phases, lattice parameters) is obtained. [Williams and Carter, 1996]. Kikuchi lines (diffraction of inelastically scattered electrons) can also be observed in thicker specimens and help to determine the zone axis as well as some lattice defects.

Figure 2.4: SAED pattern of an oxidised Fe core of a nanoparticle from sample 27K08 (left image). Schematic representation of electron diffraction of a single crystal (right image).
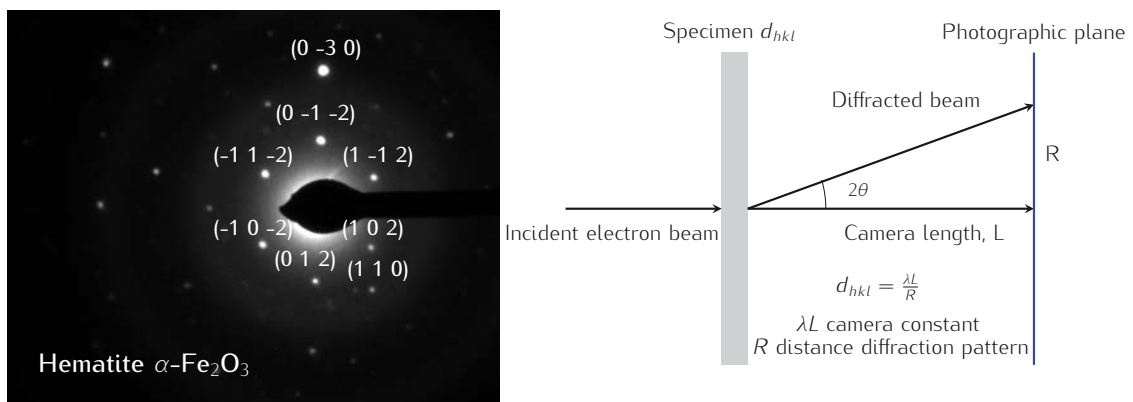
In this thesis, SAED patterns were used to determine the iron phases present in the cores of the nanoparticles. Fig. 2.4 shows an example of a SAED pattern of an iron core which was oxidised to α-Fe_2O_3 (hematite). The identification of planes was done by using Carine Crystallography 3.1. The Bragg angles are so small that we can use the small–angle approximation, $\sin \theta \approx \tan \theta$, we can write the Bragg's law as $d_{hkl} = \lambda R/L$. We should notice that interplanar distances can slightly differ from the bulk material due to the surface tension of nanoparticles [Qi and Wang, 2005, Huang et al., 2007].

2.1.4   Energy Dispersive X-ray Microanalysis (EDX)

The Energy Dispersive X–ray microanalysis (EDX) provides the rapid elemental composition of the specimen by means of the detection of the emitted X–rays when the sample is irradiated with high–energy electrons (inelastic scattering). EDX detectors can be installed on microscopes in order to use the irradiation source provided by the electron beam, using a scanning electron microscope (SEM–EDX) or a scanning transmission electron microscope (STEM–EDX).

The interaction of the irradiation electron beam with specimen atoms is described in Fig. 2.5. The energy of the emitted X–rays (emission lines K_α, K_β or L_α) is characteristic of the specimen atomic number and is used to identify the elemental composition of the sample. A typical XRD spectrum shows a list of peaks corresponding to the characteristic X–rays (emission lines) as well as a background (without useful information) coming from the continuous emission of X–rays (Bremmstrauhlung radiation) due to the deceleration of the electron beam in the field surrounding the atomic nucleus and inner–shell electrons. However, not all the ionisation events result in X–ray emission, sometimes some electrons (Auger electrons) can be ejected by the reabsorption of characteristic X–ray by an outer shell electron [Goldstein, 2003].

The most common EDX detector is based on a Lithium doped Silicon crystal Si(Li). Some artifacts can appear during the detection, such as a peak broadening, silicon X–ray escape peaks, silicon internal fluorescence peaks, silicon and gold absorption edges or other peaks contributions from the environment of the sample [of Standards et al., 1980].

In this thesis, nanoparticles were analysed by STEM–EDX using a Jeol 2100 operating at 200kV equipped with a Oxford INCAx–sight Si(Li) detector for EDX at Scientific and Technological Centres of Universitat de Barcelona.

An important element presents in our nanoparticles is Fe ($Z = 26$) with energy 6.4 keV corresponding to K_α and 0.70 keV corresponding to L_α. Elements with low atomic number ($Z < 11$) are not detected or only with limited sensitivity, this is the case of carbon ($Z = 6$).

In the present work, the use of STEM–EDX was really important to detect desirable and non–desirable elements in the sample. For example, by using EDX, we could identify some calcium nanoparticles coming from a contamination of the TEM grids (provided by the fabricant) that we would otherwise have considered as our nanoparticles (Fig. 2.6).

Figure 2.5: Schematic representation of the characteristic radiation detected by EDX.
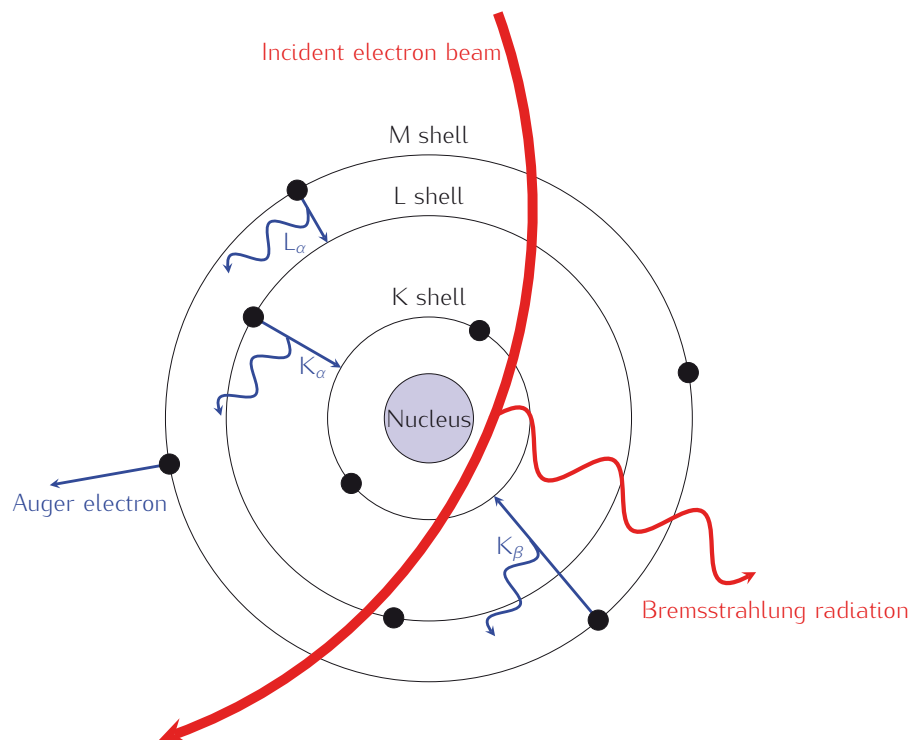
Figure 2.6: EDX spectra (left image) and TEM image (right image) of Ca nanoparticles, Ca K_α (3.69 keV) and Ca K_β (4.012 keV), nanoparticle contamination coming from some TEM grids provided by the fabricant. Some artifacts are also observed (Cu, C, Cl, Mn, Si).
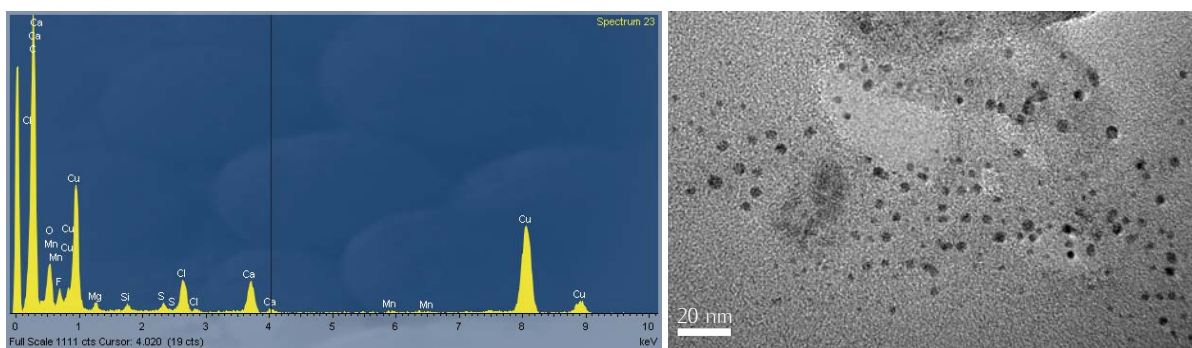
2.1.5   Electron Energy Loss Spectroscopy (EELS)

Electron Energy Loss Spectroscopy (EELS) is an analytical technique also available on an electron microscope and similar to EDX but can provide structural and chemical information with higher energy resolution (about 1 eV) allowing the detection of low–Z elements. The

analysis of the specimen is done by the inelastic scattering of the electron beam (energies between 100 keV and 300 keV) with electrons from inner and outer shells of the specimen atoms. The detector is located at the bottom of the same microscope (see Fig. 2.2).

A typical EELS spectrum in a range of 1000 eV shows a series of peaks useful to obtain chemical information about the specimen. A *zero–loss* region, without useful information, represents the transmitted electrons without energy loss or lower than the experimental energy resolution. A *low–loss* region, in the range of 4–40 eV, represents the inelastic scattering from outer–shell electrons (plasmons). The beam interaction with outer–shell electrons generates plasmons with energy [Egerton, 2009],

$$E_p = 2\pi f_p = \omega_p = \left(\frac{ne^2}{\epsilon_0 m} \right)^2 \tag{2.2}$$

where n is the density of the outer–shell electrons and m their effective mass. The EELS spectrum shows peaks at energies E_p and its multiples. The number and intensity of these peaks increase with the thickness of the specimen. Finally, the *high–loss region* (> 100 eV), where peaks represent inner–shell excitation. They take the form of edges rather than peaks and the sharp rise occurs at ionisation threshold. The ionisation edges are unique for each element and thus, energy–loss spectrum can identify the elements present in the specimen. A quantitative elemental study can be done by measuring the area under the corresponding ionisation edge, making allowance for the underlying background [Egerton, 2011].

Figure 2.7: Energy-loss spectrum of three allotropes of carbon: diamond, graphite and amorphous carbon (printed from [Egerton, 2011]).
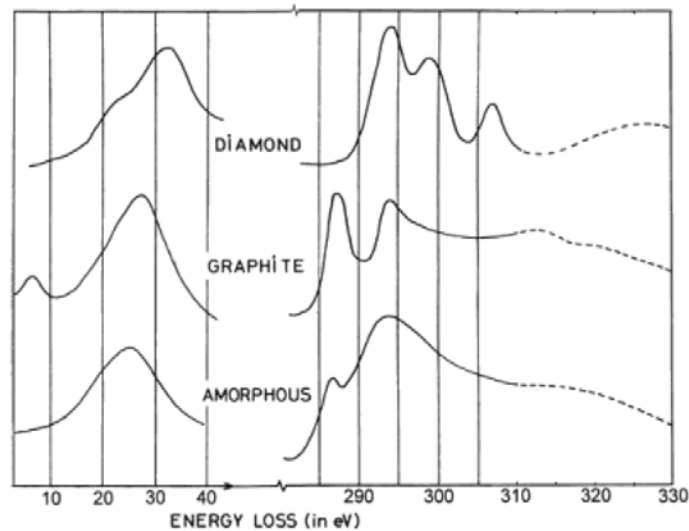
EELS technique is used to identify allotropes of carbon (Fig. 2.7), where low-loss and K-ionisation regions are well known. Plasmon peaks occur at different energies due to the different electron densities for each allotrope: 33 eV in diamond, 27 eV in graphite and 25 eV in amorphous carbon.

In this thesis, EELS was used to identify several elements present in the nanoparticles and create elemental maps. EELS was done at Scientific and Technological Centres of Universitat de Barcelona using a Jeol 2010F FEG operating at 200kV equipped with a Gatan Image Filter (GIF).

2.2   Atomic Force Microscopy (AFM)

The development of the Atomic Force Microscopy (AFM) in 1986 came from the necessity to characterise all kind of samples (polymers, ceramics, biological samples), at the time the Scanning Tunneling microscopy (STM) could only determine the surface topology of metals and semiconductors.

The STM instrument uses a sharp tip that approaches the surface specimen at very small distances, around 2-4 atomic diameters. At these distances, a tunneling current appears when a voltage is applied to the specimen. The voltage is controlled by a piezoelectric element attached to the tip, and thus the distance between the tip and specimen can be kept constant [Wiesendanger, 1994].

In the AFM, the cantilever tip is not fixed and softly touches the surface of the specimen (Fig. 2.8). The AFM measures the force between the tip and the surface instead of the tunneling current, and thus insulating materials can also be analysed. The forces are measured by an optical system based on a laser that detects the angular deflections of the cantilever. The measured forces do not surpass a few picoNewtons, in principle not enough to damage either the tip or the surface.

Figure 2.8: Schematic representation of AFM.
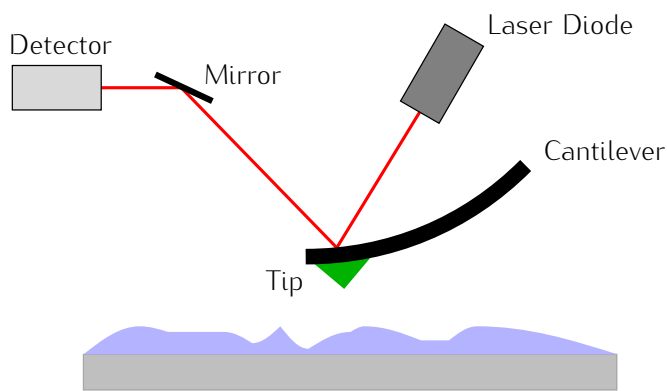
There are different AFM imaging modes depending on the applications, and are usually classified as contact or non–contact modes. The contact mode is based on the deflection of the cantilever while it is scanning the surface specimen (as we mentioned above), and non–contact mode employs a piezo element to make the cantilever oscillate at its resonance frequency. The changes in the oscillations vary in frequency, providing a surface map of the specimen. There is also another widely used mode called *tapping mode*, which consists of lifting the tip up and down just tapping the surface. The changes in the oscillation amplitude are used to measure surface features [Ricci and Braga, 2003].

Aside from topographic characterisation, the AFM can be also used to measure the dynamic behaviour of living and fixed cells, obtain a compositional mapping of polymers or for nanotribological studies.

In this thesis, AFM was used to determine the morphology of primary nanoparticles (shape, sizes) and surface topography of nanoparticle agglomeration. However, we should note that we were interested in the characterisation of Fe and AFM does not allow the visualisation of the nanoparticle cores. The measurements were performed at the Scientific and Technological Centres of Universitat de Barcelona in a Multimode AFM (Bruker) attached to a Nanoscope IV electronics. All topographic measurements were performed in tapping mode using rectangular AFM probes with a nominal spring constant of 40nN/nm (VistaProbes). Images were acquired at minimum vertical force in order to preserve the integrity of the sample and the AFM probe apex.

2.3   X–Ray Diffraction (XRD)

The X-ray diffraction (XRD) is a powerful non–destructive technique for structural, physical and chemical characterisation of materials. Sample to be characterised can be a single crystal (perfect aligned cells extended in a pattern), polycrystalline or powder (crystallites are randomly distributed). The sample placed in a holder, in a horizontal position, mounted in a goniometer and bombarded with a X-rays source at a fixed wavelength. The incident X-rays are diffracted by the atomic arrangement (unit cells into a lattice) of the crystalline sample when the Bragg's law is satisfied (eq. 2.3).The X-ray tube is fixed and detector is motorised and moves through the angular range of 2θ [Cullity and Stock, 2001] (Fig. 2.9).

The elastic scattering of X-rays with the crystal structure follows the Bragg's law (eq. 2.3):

$$2d_{hkl} \sin \theta = n\lambda_0 \qquad\qquad (2.3)$$

where the d_{hkl} is the interplanar spacing (distance between parallel planes of the lattice) and hkl are the Miller indices of each lattice plane, θ is half the angle between incident and scattered beam, n the order of reflection and λ_0 the X-ray wavelength.

Figure 2.9: Schematic representation of a powder X-ray diffractometer.
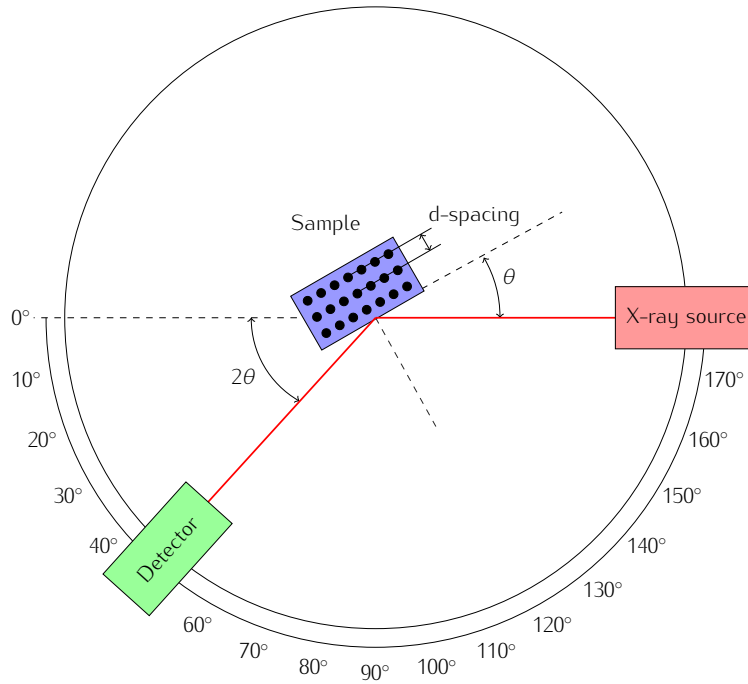
Each crystalline substance has a unique XRD pattern. The number of peaks is related to the symmetry of the unit cell, for instance cubic crystals (bcc lattice) present the highest symmetry and show fewest peaks. The peaks are identified with hkl Miller (the set of lattice planes $\{hkl\}$ responsible for the diffraction peak) and thus, the crystal structure and its lattice parameters can be determined.

The XRD is used for several applications, such as the crystal phase identification, polymer crystallinity, stress or texture analysis [Inc., 1999].

In nanophase materials, the XRD pattern exhibits significant line–broadening to respect bulk material. The peak widths can be used to provide an estimation of the average crystallite size by using the Scherrer equation [Scherrer, 1918, Langford and Wilson, 1978],

$$D_{\mathrm{hkl}} = \frac{K\lambda}{B_{hkl}\cos\theta} \tag{2.4}$$

where λ is the X-ray wavelength, β is the full width at half maximum intensity (FWHM), K is a shape factor and θ is the Bragg's angle. The peak broadening due to the instrumentation must be subtracted.

In carbon–based materials, XRD allows to identify different carbon allotropes and polytypes and to determine the crystalline degree departs from the ideal graphite structure. Using the Scherrer modified Warren equation to the (002) and (10) peaks, one can determine the height (L_c) and width (L_a) of the graphite–like crystallites present in the sample [Bottani and Tascón,

2008].

In this thesis, the crystal structure of nanoparticles was analysed by low–angle X–ray diffraction (LAXRD) with a PANalytical X'Pert PRO MPD (model DY 3197) equipped by a Cu X–ray source ($K_{\alpha1,\alpha2}$, $\lambda = 1.5418\,\text{Å}$) at the Scientific and Technological Centres of Universitat de Barcelona. Samples were prepared by depositing drops of nanoparticle solution (Fe@C nanoparticles dispersed in ethanol) onto a silicon wafer until a thin film of nanoparticles is observed.

2.4   Raman spectroscopy

Raman spectroscopy is one of the most widely used characterisation methods in order to determine the crystallisation degree of carbon–based nanomaterials. This technique is very interesting because of its non–invasive nature and provides global information of the material in contrast with electronic microscopy techniques.

The Raman effect is a scattering phenomenon produced when an incident monochromatic electromagnetic wave (photon) in the range of visible, near infrared or near ultraviolet interacts with the electric dipole of a molecule or with the crystal lattice from a solid. During the interaction, the molecules or the phonons from the lattice may gain or lose energy depending on their energetic initial state. These energies are lower than the electronic state energies and are known as virtual states. Finally, the incident photons are scattered at different frequencies from the initial one. The resulting inelastic scattering of photons corresponds to the Raman spectrum observed from a sample. If there is non inelastic scattering, the process is called Rayleigh (Rayleigh–Debye) or Mie scattering, and no Raman effect is observed.

The spectrum of the scattered photons consists of a strong line corresponding to the excitation frequency of the incident light with other lines at shift frequencies. Two kind of lines exists depending on the scattered frequency of the photons. The Stokes lines are generated when the shift frequencies are lower than the excitation one and Anti-Stokes lines, the other way around (Fig. 2.10).

In carbon–based nanomaterials, such as fullerene, graphene, SWCNT, MWCNT or CEMNPs, the different lines observed in the Raman spectra allow us to characterise them. In figure 2.11 is depicted a typical spectra from these nanomaterials in order to identify the most important lines [Marsh and Rodríguez–Reinoso, 2006].

Graphitic materials are characterised to present two main vibrational modes corresponding to D and G bands. For visible excitation, these peaks are located around 1360 and 1560 cm $^{-1}$ respectively. They are dominated by the sp^2 sites, since visible excitation always resonates with the π states [Ferrari, 2007].

Figure 2.10: Energy level diagram corresponding to elastic scattering (Rayleigh) and in-elastic scattering (Stokes and Anti-Stokes Raman signal).
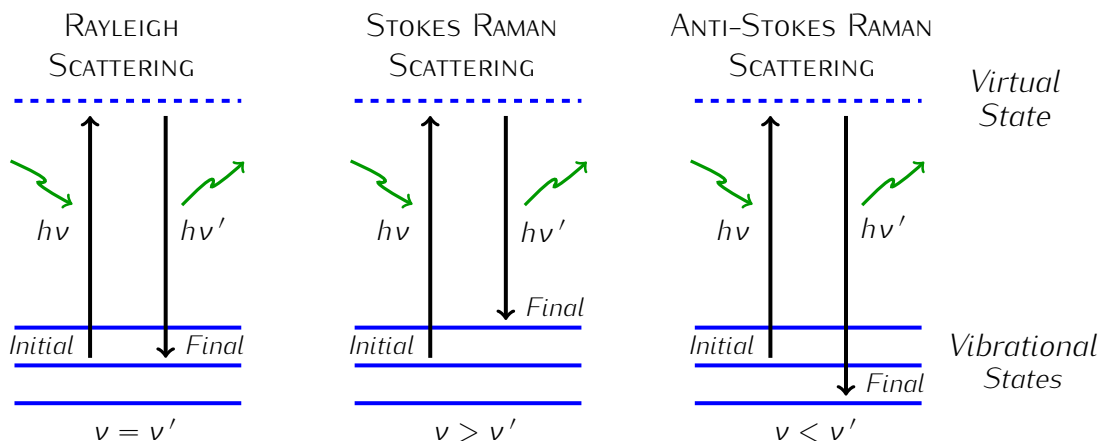
The D peak is due to the A_{1g} breathing mode of sp^2 atoms in rings. It is forbidden in perfect graphite and it is related to the disordered amorphous of the structure. The G peak is due to the bond stretching of all pairs of sp^2 atoms in both rings and chains and corresponds to the mode with E_{2g} symmetry of perfect graphite. Figure 2.12 is showing the corresponding carbon motions for both modes. The intensity ratio $I(D)/I(G)$ gives us information about the crystallinity degree. The lower the ratio, the higher crystallinity presents the sample. In order to calculate this ratio a fitting is required. Gaussian and Lorentzian fittings are the most common used and the $I(D)/I(G)$ corresponds to the ratio of the peaks areas or the peak heights, respectively [Ferrari and Robertson, 2000].

In addition to D and G bands, all kind of graphitic materials exhibit a strong Raman band in the range 2500-2800 cm^{-1}. Fig. 2.13 shows a comparison spectra of graphene and graphite measured at 514.5 nm [Ferrari, 2007]. The *2D* or *D**band, which corresponds to the overtone of the D band is clearly observed in graphene and graphite (Fig. 2.13b) while in amorphous carbon is not obtained.

In this thesis, nanoparticles were characterised by micro-Raman spectrometer (Labram HR 800, Horiba Jobin Yvon) using an ion-Ar laser excitation of 514.4 nm, an objective magnification of 50x and an incident power of 1.8 mW, at the Scientific and Technological Centres of Universitat de Barcelona. Samples were prepared by depositing some drops of nanoparticle solution (Fe@C nanoparticles dispersed in ethanol) onto a clean glass coverslip.

Figure 2.11: Raman spectra for different carbon–based materials. Most important lines are identified.
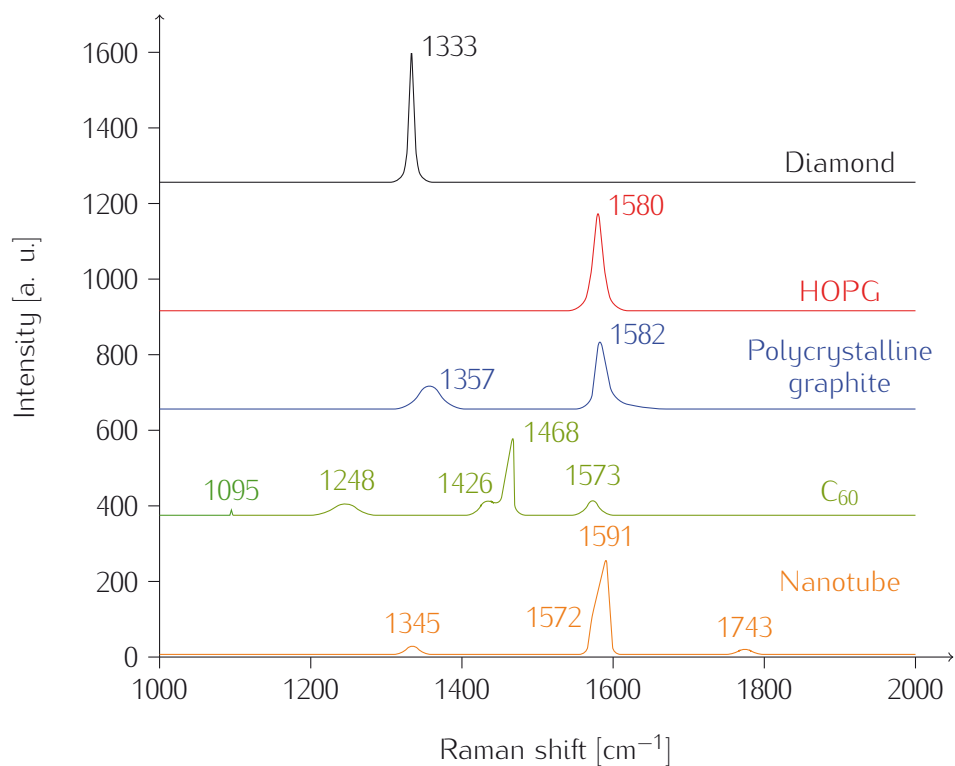
Figure 2.13: Comparison Raman spectra of graphite and graphene measured with excitation wavelength 514.4 nm (reprinted from [Ferrari, 2007]).
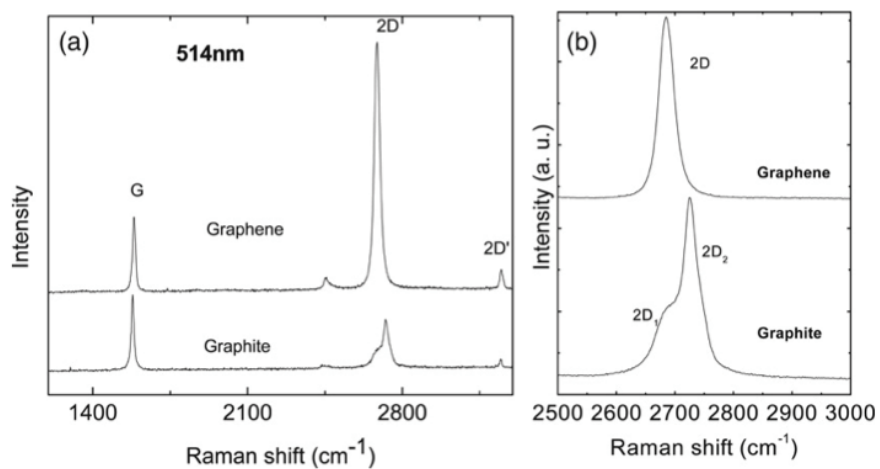
Figure 2.12: Schematic illustrations of the motion of carbon atoms in the D and G vibrational modes.

A_{1g} D breathing mode E_{2g} G mode
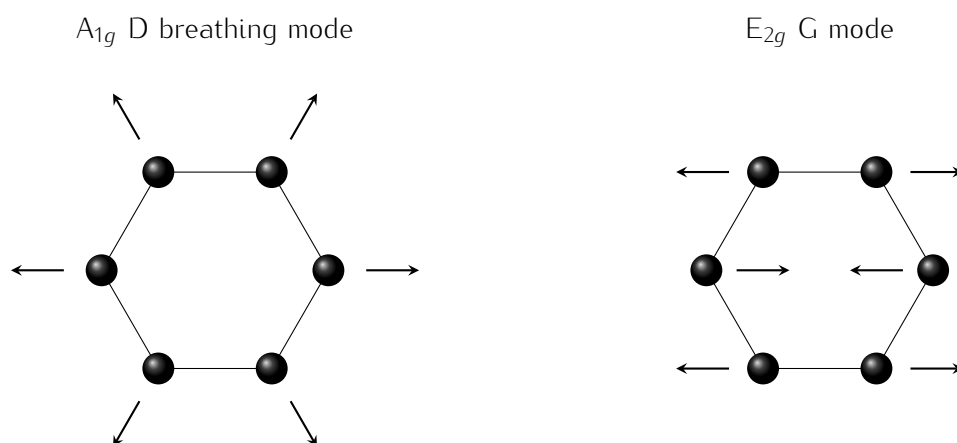
2.5   Elemental analysis (EA)

The Elemental analysis is used to quantify the elemental composition of organic compounds, such as carbon, nitrogen, hydrogen or sulphur, by means of controlled combustion at high temperatures around 1800 °C in a pure oxygen stream (dynamic system). Subsequently, the resulting gases generated from the oxidation reactions, C to CO_2, H to H_2O or N to N_2, are separated and detected through a gas chromatography column. A thermal conductivity detector provides a signal with different peaks corresponding to the studied elements. The integrated areas of each peak are proportional to the amount of each element in the sample. The sample to analyse has a mass of about 1–2 mg and is deposited on a tin container to improve ignition and combustion of the sample [Hemming, 2007, Instruments, 2006].

Our samples were analysed at Scientific and Technological Centres of the Universitat de Barcelona using an elemental organic analyser Thermo EA 1108 (Thermo Scientific, Milan, Italy) working in standard conditions recommended by the supplier of the instrument (helium flow at 120 ml/min, combustion furnace at 1000 °C, chromatographic column oven at 60 °°C, oxygen loop 10 ml at 100 kPa.

2.6   Photon Correlation Spectroscopy (PCS) and ζ-potential

The Photon Correlation Spectroscopy (PCS) also know as Dynamic Light Scattering, is a technique used to characterise and determine the hydrodynamic size and size distribution of nanoparticles, in a range of about 5 nm to 3 μm. All the information is contained in a correlation function, which is mathematically treated to find the size distribution (Fig. 2.14). Nanoparticles dispersed in a liquid solution undergo random thermal fluctuations (Brownian motion) and when

Figure 2.14: Schematic drawing with the basics of PCS.
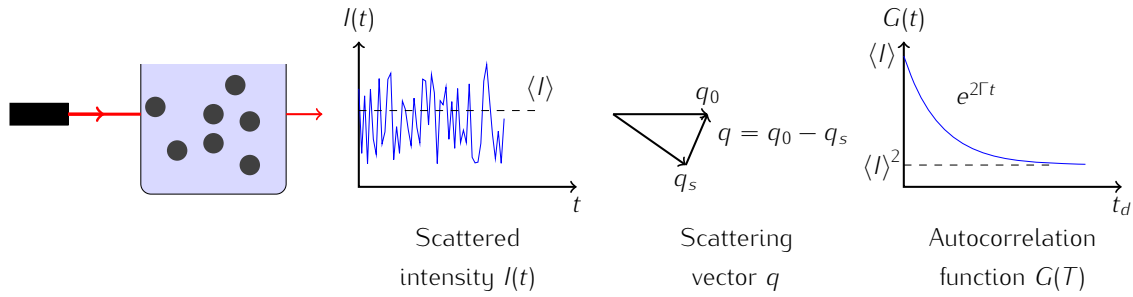
pass through the laser beam, the scattered light intensity is detected. The intensity fluctuates in time (rapid timescale $10^{-6} - 10^{-3}$ s) and its mean value $\langle I(q) \rangle$ is the quantity that can be measured[Bowen, 2002, Tscharnuter, 2006].

$$\langle I(q) \rangle = KNM^2P(\Theta)B(c) \tag{2.5}$$

$$q = \frac{4\pi n}{\lambda_0 \sin(\Theta/2)} \tag{2.6}$$

$$G(t_d) = \frac{1}{N} \sum_{i=1}^{N} I(t_i - t_d) \tag{2.7}$$

where $\langle I(q) \rangle$ is the mean scattered intensity in terms of particle parameters, K is an optical constant, N is the number of scattering particles, M is the mass of a particle, $P(\Theta)$ is the particle form factor and $B(c)$ is the concentration factor. The q is the magnitude of the scattering vector, Θ the scattering angle, n the refractive index of the suspending liquid and λ_0 the wavelength of the laser. The autocorrelation function, $G(t_d)$ depends on the number of samples N and the time delay t_d between samples.

The terms M^2 and $P(\Theta)$ are particularly important to determine the size distributions. M^2 is proportional to the sixth power of the diameter, and thus large particles will overwhelm the signal from smaller ones. In addition, shape information contained in $P(\Theta)$ is not easily obtained.

The diffusion coefficient of the particles can be calculated from the scattered intensity and thus, the hydrodynamic diameter can be obtained. For spherical nanoparticles, the diffusion coefficient D_0 is directly related to the hydrodynamic diameter d_h as follows,

$$D_0 = \frac{k_B T}{3\pi\eta(T)d_h} \tag{2.8}$$

where k_B is the Boltzmann constant, T the absolute temperature and $\nu(T)$ the viscosity of the suspending media. The hydrodynamic diameter is usually larger than the diameter obtained from dry nanoparticles, since it takes into account the *electrical double layer* to be formed

around the nanoparticles (see subsection 2.6.1). In the surroundings of the electrical double layer, it is considered that the liquid moves together with the particles.

This technique presents several advantages, for instance, measurements are very fast and small amount of nanoparticles can be measured. However, the correlation function can be approximated by different models and the resulting histograms do not show high–resolution size distributions.

2.6.1 ζ-potential

Zeta (ζ) potential measurements give an idea of the electrostatic repulsion between nanoparticles dispersed in liquid and determine the colloidal stability of the suspension. The technique consists of applying a DC or low frequency AC electric field to the suspension, and detect the frequency of the scattered laser light due to the movement of the charged nanoparticles towards the positive or negative pole of the applied field [Dukhin, 2010]. The resultant movement is called electrophoresis. Equilibrium is reached when viscous forces opposes to the movement and nanoparticles move with constant velocity. By measuring the Doppler frequency shift, given the laser wavelength and the scattering angle, the electrophoretic mobility ($m^2V^{-1}s^{-1}$), μ_e can be obtained.

Zeta potential is related to the electrophoretic mobility by the following equation 2.9,

$$\mu_e = \frac{\zeta \epsilon f(\kappa a)}{\eta(T)} \tag{2.9}$$

where $v(T)$ is the viscosity, T the absolute temperature, ϵ the dielectric constant of the media; and $f(\kappa a)$ is a function of the radius of the particle, a, and the electrical double layer thickness, κ. Depending on the dispersions, this function can be established as $f(\kappa a) = 1.5$, known as Smoluchowski relationship or $f(\kappa a) = 1$ (for nonpolar media), the so–called Hückel relationship. For intermediate values, the function should be evaluated numerically.

The zeta potential is not directly the surface charge of the nanoparticles, since it exists a layer (Stern layer) where ions are strongly bound on the nanoparticle surface and at the same time, a diffuse screening layer is formed by counter-ions. The complete structure is called *double layer* and its thickness is the Debye length. More information is provided in subsection 1.1.4.

High values of zeta potential represent stable dispersions and the opposite, unstable. The threshold of stability is usually established when zeta potential equals 25–30 mV, except when the stabilisation is achieved by steric repulsions.

The pH of the solution has an important effect on the zeta potential. The zeta potential is commonly depicted as a function of pH. The more alkali the suspension is, the more negative charged acquires the nanoparticles. The opposite way, the more acid the suspension is, the positive charged is reached. The point at which the zeta potential is zero, is called isoelectric

and provides practical information about the colloidal stability of the system.

In this thesis, PCS as well as zeta–potential measurements were performed at École Poly-technique Fédérale de Lausane (EPFL) using a Brookhaven ZetaPALS instrument equipped with a BI–9000AT digital autocorrelator, a laser diode at $\lambda = 661$ nm as a light source and the de-tector aligned at 90°. More details are described elsewhere [Bowen, 2002]. The measurements were done using the Smoluchowski model, adding the viscosity of water and the corresponding refractive index of carbon at 633 nm of $n_R = 2.73$ and $n_i = 1.42$.

2.7   CPS: disc Centrifuge Particle Size analyser

The CPS disc centrifuge is another technique used to measure size distributions of nanoparticles in a solution, in the size range of approximately 5 nm to 75 µm, using gravity and centrifugal forces (Fig. 2.15). It consists of a disc which rotates at different speeds depending on the size range to detect. The detection is done by means of absorption of visible light or x-rays.

The rate of sedimentation is given by Stokes' law [Stokes et al., 1904]. The main assumption is the sphericity of the particles, since the theory describes the drag force in terms of the viscosity of the fluid, the velocity of the movement and the diameter of a spherical particle moving through a fluid.

Figure 2.15: Schematic diagram of a disc centrifuge.
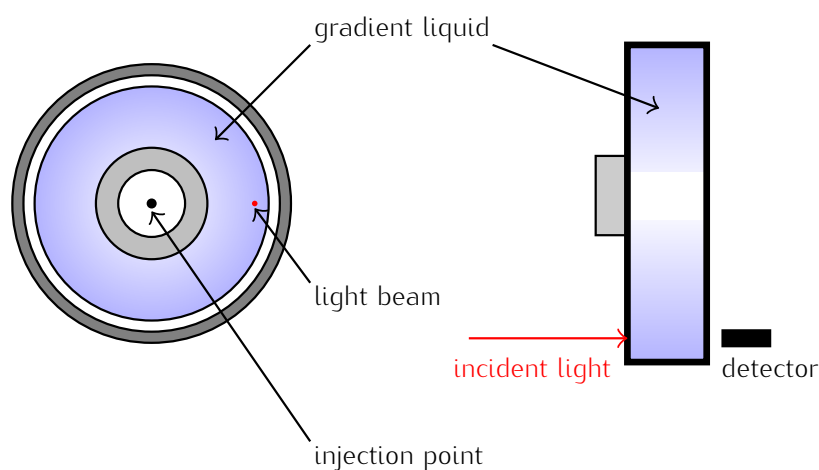
The drag force acting on a particle is given by the particle diameter D, the fluid viscosity v and the settling velocity V as follows (eq. 2.10):

$$F_D = 3\pi D v V \tag{2.10}$$

The gravitational force in a constant field depends on the particle diameter D, the particle density ρ_P, the fluid density ρ_f and the gravitational acceleration g (eq. 2.11):

$$F_G = \frac{\pi}{6}D^3(\rho_p - \rho_f)g \tag{2.11}$$

When both are equal, and the time required for the particle to move from the surface of the fluid to a known distance X is given by $t = X/V$, the diameter of a particle can be determined by measuring the time required to sediment (eq. 2.12):

$$D = \frac{X18\nu}{(t(\rho_p - \rho_f)g)^{1/2}} = \frac{K}{t^{1/2}} \tag{2.12}$$

K is established as a constant, since several parameters in eq 2.12 can be determined. Although, we are not considering the centrifugal acceleration inside the disc, for those conditions, the same equation $D = K/t^{1/2}$ is also valid to describe the process [CPSmanual,]. Two sucrose solutions (8 wt% and 24 wt%) are injected onto the disc in order to provide a density gradient inside the disc and to ensure a stable sedimentation process. In addition, in order to avoid evaporation a low density oil such as dodecane or tetradecane is also used.

In this thesis, particle size measurement (number and volume weighted distributions) from analytical disc centrifuge was carried out at École Polytechnique Fédérale de Lausanne (EPFL) with a CPS Instruments Europe at 17633 rpm, a density of 2.2 g/ml, an absorption coefficient of $K = 0.7$ and the theoretical carbon refractive index ($n = 2.67$).

2.8   Superconducting-quantum-interference-device (SQUID) magnetometer

The SQUID magnetometer is a high resolution equipment employed to measure magnetic moments in the range $10^{-10} - 10^3$ Am^2 [Buschow and Boer, 2003].

It is based on the Josephson effect occurring in Josephson junctions consisting of two parallel superconductors separated by an insulating layer at very low temperatures. At these conditions, a Cooper pair can flow through the insulating barrier by quantum tunneling having the same wavelength and phase, generating an electric current without any external electric field. This is known as DC Josephson effect. The current is proportional to the phase difference of the wavefunction of the Cooper pair. When a DC voltage is applied, then an oscillating current can flow through the junction, the so-called AC Johnson effect. The frequency is proportional to the applied voltage and can be obtained with very high accuracy. The voltage oscillations allow to determine the flux change and thus, the associated magnetic field.

The conventional SQUID magnetometer-susceptometry is used to measure the magnetic response of samples depending on the applied magnetic field and temperature. A sample of a

few millimetres in size is introduced inside a first or second–order superconducting gradiometer (Fig. 2.16). The movement of the magnetic sample induces an electric current in the detection coil system. This change in the current produces variations in the SQUID output voltage proportional to the magnetic moment of the sample, providing highly accurate measurements [Clarke and Braginski, 2007].

The magnetic characterisation of our samples has been done by using a SQUID MPMS–XL Quantum Design (5 T) provided by Scientific and Technological Centres of Universitat de Barcelona. The system is cooled by liquid helium and allows the magnetic study in the temperature range from 1.7 K to 350 K, and applied magnetic fields up to 5.5 T.

Figure 2.16: (a) Schematic drawing of SQUID magnetometer–susceptometer. (b) Calibrated output from SQUID electronics, recorded as a function of position (modified from [Clarke and Braginski, 2007])
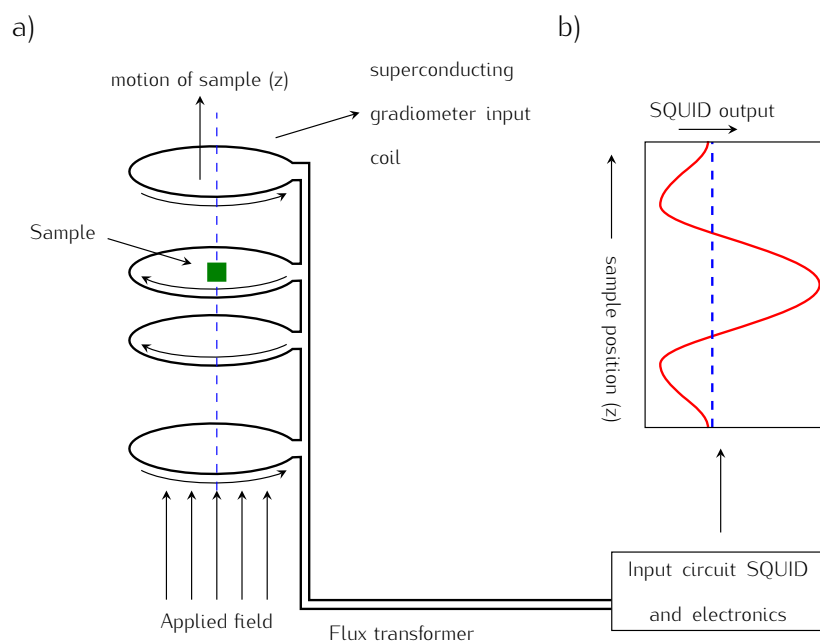
2.9   Optical Emission Spectroscopy (OES)

The Optical Emission Spectroscopy (OES) is a diagnostic technique for plasma characterisation, providing information about the excited species present in the plasma, by means of the ultraviolet–visible light emission. A plasma is based on the collective movement of neutral, positively and negatively charged particles[1]. Electrons are the lightest particles in movement

---

[1]In this case, we use the name particles referring to elemental particles instead of nanoparticles.

and the easiest to be accelerated (the most energetic), causing collisions and thus, ionisation or dissociation of the molecules of the gas. The collisions of electrons and heavy targets can be elastic or inelastic depending on whether the targets are excited to a higher energy level. The energy transfer between electrons and targets can be less than 0.1 eV (rotational excitation) or more than 10 eV (ionisation) [Chapman, 1980].

From OES spectra, principal species present in plasma can be identified by their character-istic emission lines (see Table 2.1).

Table 2.1: Emission lines of principal species present during plasma processing tech-niques [Biederman, 2004]

Species	Transition	Wavelength (nm)
H_α Balmer system	n:3→2	656.2
H_β	n:4→2	486.1
H_γ	n:5→2	434.0
H_δ	n:6→2	410.2
C	$^1D \rightarrow {}^1P$; $^1S \rightarrow {}^1P$	193.1; 247.8
C_2 Swan band system	$d3\Pi_g \rightarrow a3\Pi_u$	Bandhead: 516.5
CH	$A^2\Delta - X^2\Pi$	Bandhead: 431.4
OH	$A^2\Sigma \rightarrow X^2\Pi$	Bandhead: 306.4
O	$3p\,^3S \rightarrow 3s\,^3S$	Bandhead: 844.0

Under certain conditions, theoretical calculations based on the assumption that plasma is in thermodynamic equilibrium or local thermodynamic equilibrium (LTE) can be applied in order to determine several characteristic parameters, for instance the ionic and electronic temperature or ionic and electronic densities, among others. In a perfect thermodynamic equilibrium, all radiation emitted is reabsorbed at the same rate. When this occurs, the plasma radiation can be described by the blackbody Planck's law [Irvine, 1967] and the plasma temperature is identical to the temperature of this blackbody radiation.

$$B_\nu(T) = \frac{2h\nu^3}{c^2} \frac{1}{\exp\left(h\nu/k_B T\right) - 1} \tag{2.13}$$

In a laboratory, a perfect thermodynamic equilibrium is not possible since reabsorption of radiation is usually low [Cooper, 1966]. However, LTE is assumed when the energy exchange is collision dominated (i.e. at sufficiently high particle density) [Gundel et al., 1991].

In this thesis, OES was applied to determine the temperatures of the plasma generated by applying different currents in the modified arc-discharge plasma (mADP) reactor. In addition, the chemical elements present in the plasma were also identified. The spectrometer used was a Stellarnet EPP2000 spectrometer in a UV-VIS range of 190–850 nm.

3

Experimental set-up

Nowadays, there are several techniques to produce carbon–encapsulated magnetic nanoparticles as we mentioned in section 1.3. The most commonly used are: laser ablation [Dumitrache et al., 2004, Park et al., 2008], pyrolysis [Lu et al., 2005], arc discharge [Bystrzejewski et al., 2005], chemical vapour deposition (CVD) [Lee et al., 2005] and derivatives (plasma–enhanced CVD, catalytic CVD) [Yang et al., 2009, Wang et al., 2007a], among others. Actually, most of this technology becomes from the processes originally used for obtaining carbon–based nanomaterials, such as SWCNTs, MWCNTs or fullerenes [Mostofizadeh et al., 2010]. These techniques were based on the thermal decomposition of hydrocarbons or the erosion of graphite at high temperatures [Bhushan, 2004].

In our case, the technique used was the arc–discharge plasma method. In comparison with other processes, the equipment is relatively simple and is not so expensive (high vacuum is not required, no lasers are needed), nanoparticles are obtained in high purity as well as the parameters to control the fabrication of nanoparticles can be easily modified, such as chemical input (working gas), pressure range (from 0.1 Pa to atmospheric pressures), the discharge configuration (size and composition of electrodes) or the temporal behaviour (DC plasma, pulsing plasma) [Bogaerts et al., 2002]. Besides the advantages that this technique presents, it was also the first widely used technology, sometimes known as Krätschmer method [Krästchmer et al., 1990], for the production of fullerenes, SWCNTs and MWCNTs. Moreover, our research group has a widely experience in plasma technologies for the production of carbon–based nanostructures.

3.1   Conventional arc–discharge plasma method (ADP)

3.1.1   ADP technology: Previous studies

The conventional arc–discharge plasma is a technique used for the synthesis of nanomaterials that consists of forming an arc column (plasma) between two electrodes using DC, AC or RF power sources. A gas stream is inserted to supply the plasma and an arc is generated between the electrodes which ionises the inserted gas [Ushio, 1988]. With the purpose of synthesising carbon–encapsulated magnetic nanoparticles, electrodes are usually made of pure graphite rods, which provide the carbon source, and one of them is drilled and filled with the magnetic material in solid state. The experiments are carried out in a vacuum chamber under pressure ranges of 50 mbar–1000 mbar and in an inert atmosphere (He, Ar) or reactive gases (N_2, H_2, CO, ethanol, methanol). The discharge current used is usually between 20-200 A.

Several authors have been working on this technique for the synthesis of nanoparticles. Dravid and co-workers [Dravid et al., 1995] were the first who reported carbon–coated ferromagnetic nanoparticles made of Fe, Co and Ni from 7 to 14 nm in diameter, encapsulated by graphitic shells. They used a modified arc discharge method with a helium gas jet direct through the arc in order to control the mean particle size by increasing the quench rate of the metal vapour [Teng et al., 1995]. Jiao et Seraphin [Jiao and Seraphin, 1998] continued the study of Dravid and co-workers and changed the size of the graphite anodes in order to study the effect of the rate of carbon and metal supply on the size distribution of the nanoparticles. They observed that using a larger crucible with a larger amount of metal source, the size of the particles also increased. Bonard et al. [Bonard et al., 2001] studied also the effect of chamber pressure on the size of carbon–encapsulated cobalt nanoparticles. They studied three different pressures (50 mbar, 200 mbar and 500 mbar) and observed that lower chamber pressures cause a decrease of the mean cobalt diameter from 26 to 9 nm.

Other authors tried to change the carbon or metal source. Dong et al. [Dong et al., 1999] synthesised this kind of nanoparticles by using methane in the gas state as a supply of carbon instead of using carbon anode, which was made of Fe-Co alloy, while a carbon rod served as the cathode. Seraphin et al. [Seraphin et al., 1996] used different elements as metal sources in order to study the carbon encapsulation mechanism. They showed that elements that form stable carbides promotes the graphitic encapsulation. However, carbon cages could also be observed even when there are no carbides, but when the carbide formation is too aggressive, no carbon cages are found.

Bystrzejewski et al. [Bystrzejewski et al., 2005] studied the C_{60} yield in the collected soot from the walls of the reactor during the production of carbon–encapsulated FeNdB nanoparticles. They found that the production of C_{60} is hampered by the formation of nanoparticles, therefore no presence of fullerenes is found where the content of FeNdB is maximum.

Despite all this studies, the parameters that affect the growth mechanism of this kind of

nanoparticles are not yet clear and nanoparticles are obtained in a dispersed size range, making their use for several applications very difficult. In addition, they are found in an agglomerated state and it is also remarkable the amount of sub-products that can be obtained during their synthesis, such as carbon nanotubes, fullerenes or carbon nanoparticles.

3.1.2   First experimental set-up: A Conventional ADP reactor

According to the previous studies, we designed a new conventional ADP reactor in order to study the different parameters involved in the formation of carbon-encapsulated magnetic nanoparticles (see chapter 4). The experimental setup was developed during the Master's thesis [Aguiló-Aguayo, 2007].

The reactor consisted of three main parts (Fig. 3.1):

Figure 3.1: Schematic drawing of the conventional ADP reactor used in our experiments (chapter 4) for the production of Fe@C nanoparticles.
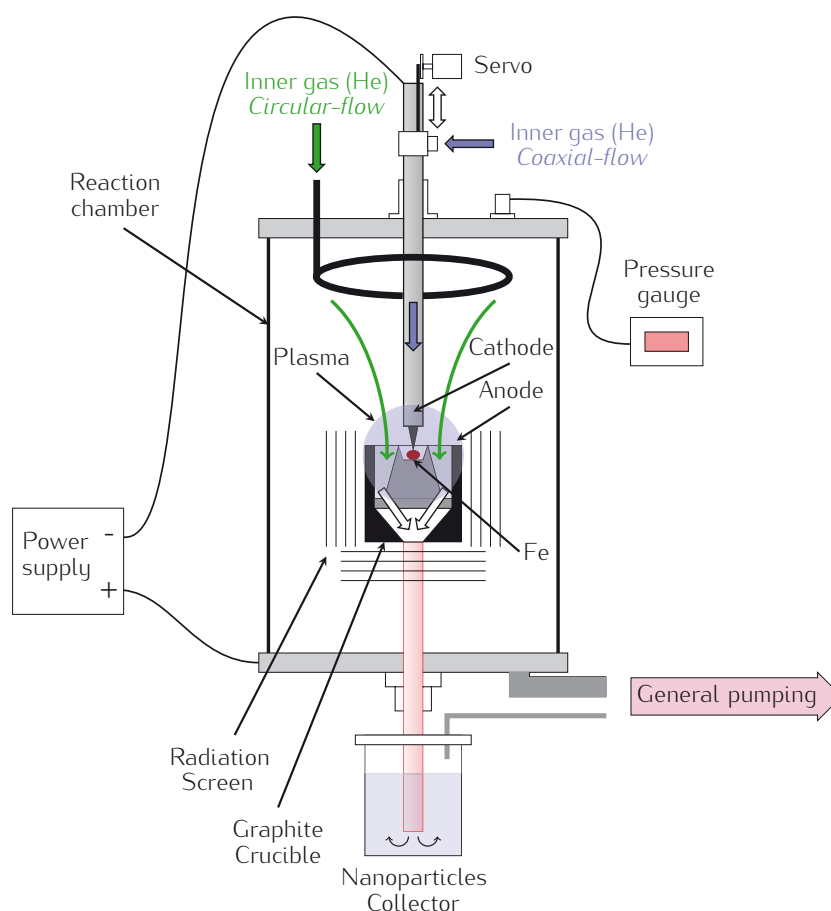
1. **Cathode-Anode configuration:**
   Two vertically aligned electrodes made of pure graphite were faced to each other in order

to ignite the arc and form the plasma.

Multiple foils of iron (purity 99.99 %) as raw material were tightly fixed in a hole of the graphite column which was grounded and used as the anode.

2. **The gas injection configuration:**

   Two configurations of gas injection were used: *surrounding gas flow (circular-flow)* and *gas flow coaxial nozzle (coaxial-flow).*

   The coaxial configuration worked as a jet of gas going through the plasma area. The circular configuration allowed to introduce the gas into the reaction chamber but not directly to the plasma area.

3. **A pressure system:**

   The pressure system consisted of a vacuum pump and different valves in order to use different chamber pressures and force the gas flow to drag the nanoparticles to the collection chamber. However, nanoparticles were also obtained from the walls of the reactor chamber.

The results obtained by using this system are explained in chapter 4. Nanoparticles were obtained with large sizes and broad size distributions, and different iron composition. Moreover, the yield of nanoparticles was very low, for same experiments of about $100\,\mu$g during $5\,$min plasma duration. In addition, nanoparticle manipulation by the user was complex and a safest operating procedure was required. For those reasons, we decided to design a new ADP method in order to overcome the mentioned problems.

3.2   A modified ADP method

A common problem with the arc method is the instability in the arc, which caused the formation of large particles [Teng et al., 1995]. In order to improve the stability of the plasma, which was crucial to obtain smaller core sizes as well as smaller standard deviations, we decided to use a metal precursor made of an organometallic compound in a liquid state instead of solid Fe precursor.

The precursor injection in our system was completely new in the ADP technology and allowed us to improve the quality of nanoparticles (smaller sizes, narrowest size distribution), to better control the Fe composition and carbon encapsulation, to obtain higher yield of nanoparticles than the previous reactor (of about $5\,$mg for $5\,$min plasma duration) as well as to work at atmospheric pressures and thus reducing the costs related to the vacuum system. In addition, we improved the operation procedure to collect nanoparticles and manipulate them in solution, which is the safest mode.

However, as we discussed in section 5.1, other aspects must be improved, such as the production of nanoparticles that is not high enough for commercial use, some agglomeration of nanoparticles is still present, and the cleaning procedure of the reactor and nanoparticles is time–consuming. We should mention that during this last year a third reactor has been designed and developed within a thesis master of the FEMAN group [Chaitoglou, 2012] in order to overcome the drawbacks from the present technology.

The apparatus used to produce carbon–coated nearly monodisperse superparamagnetic NPs (Fig. 3.2) consists of four parts:

Figure 3.2: Schematic drawing of the modified ADP experimental set–up used in our experiments (section 5.1) for the production of Fe@C NPs.
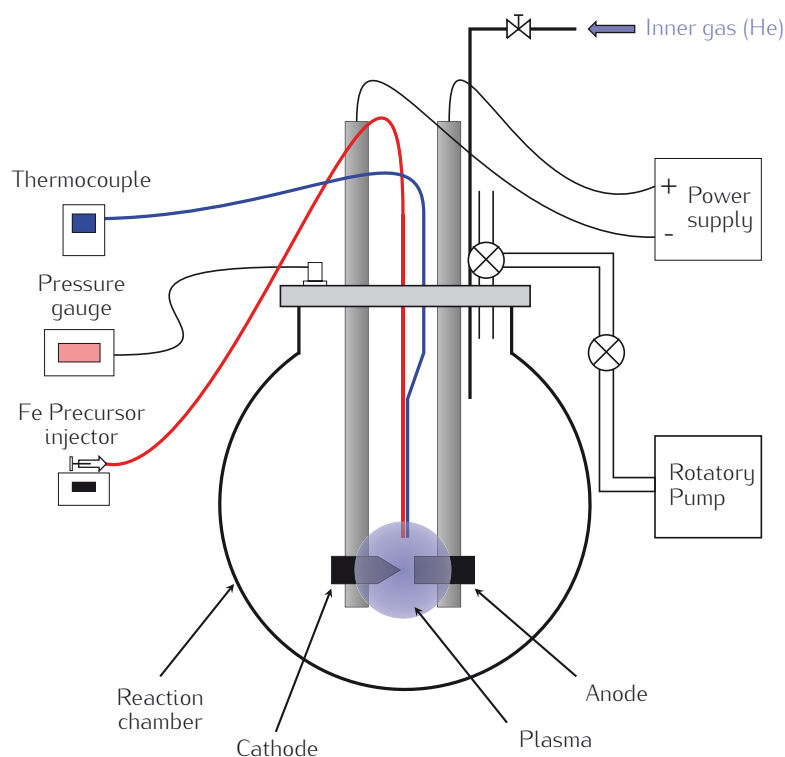
1. **The reaction chamber:**
   The reaction chamber is composed of a semi–spherical borosilicate glass chamber with a capacity of 4 L and a sealed stainless steel upper tap, immersed in a water bath. When plasma is formed, thermophoretic and convection forces act on NPs depositing them on the cooled glass chamber. Afterwards NPs can be directly collected and dispersed in different liquid solvents such as water, ethanol, acetone or methanol among others, depending on the desired application. This procedure provides clean and safe manipulation of NPs by the user.

2. **The gas entrance and vacuum control:**

Helium is the gas employed to form the plasma. Its low electrical breakdown strength stabilises the plasma, even at low direct current and its non–reactive nature helps preventing non–chemical reactions during the NPs formation. In addition, helium is the most commonly used gas to obtain high–quality carbon coating in plasma processes. A micrometer valve is used to regulate the flow rate of the gas. Another valve links the system to the outside, which allows maintaining atmospheric pressure inside the reactor chamber. Rotary vane pump is used to obtain an initial vacuum of 0.1–1.0 Pa in order to ensure, before the generation of NPs, a low oxygen content inside the chamber at the same level as He impurities (He N5) of about 10 ppm. However, no further vacuum is required during the process, decreasing the costs for industrial production. A pressure gauge is used to measure the total pressure of the chamber. Vacuum is maintained during the process by a mechanical gauge (Digitron VAP445) at a pressure of 100 Pa.

3. **A pair of electrodes anode–cathode:**

The power supply is turned on and electrodes are faced to form an arc and ionise the helium. The power supply can provide currents ranging from 5 to 200 A. The electrodes are composed of two vertical 12 mm diameter and 400 mm length stainless steel rods. Each piece has an attached horizontal graphite rod (99.9 % purity) of 12 mm diameter and 50 mm length, and facing each other at an angle of 90º. This allows a rotational movement of the electrodes during the plasma formation and distance control between anode and cathode (of about 1–5 mm), thus preventing plasma quenching due to the consumption of graphite electrodes, which supplies the carbon coating for the NPs. In addition, the anode has a sharp end of 36º for better arc ignition 3.3.

4. **Precursor injector:**

The precursor injector is the most important part of the system. Its configuration allows the direct introduction of the precursor in the plasma area and a continuous input of source material for the formation of NPs. The injector consists of two parts. Firstly, a syringe pump controls the flow rate (up to hundredths of ml/min) and the final volume of the precursor. Secondly, a vertical nozzle allows the release of the precursor by gravity drip directly to the plasma area. In addition, a thermocouple is tied to the precursor nozzle, and both can be placed at different distances of the electrodes in order to control the precursor temperature.

In our case, the precursor used to produce Fe@C is a solution of ferrocene diluted in isooctane. The ferrocene is an organometallic compound commonly used in the synthesis of carbon nanotubes or carbon–encapsulated magnetic nanoparticles in processes such as, CVD, laser ablation, pyrolysis, among others, due to its catalytic effect in the formation of carbon nanostructures [Sen et al., 1997, Hou et al., 2002]. The dilution of ferrocene

Figure 3.3: 3D schematic drawing of the modified ADP reactor. The reaction chamber is immersed in a water bath. A detailed image of the configuration of anode–cathode electrodes and precursor injector is represented.
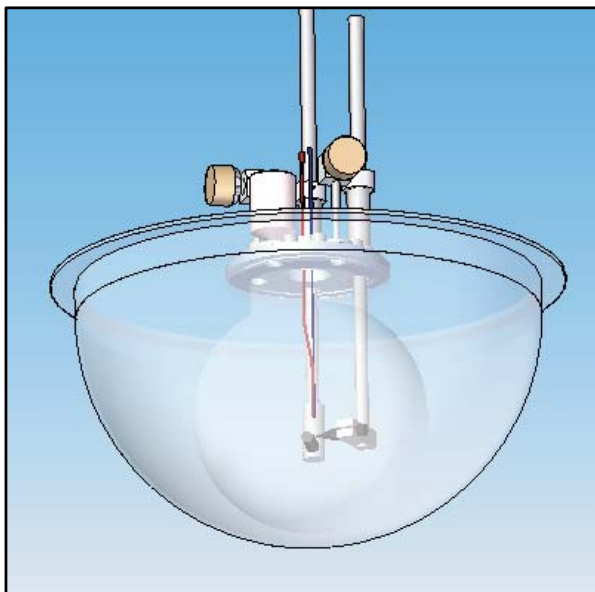
in isooctane allows us to work in a liquid phase and at lower temperatures, around 200ºC, for the decomposition of the precursor (lower than the decomposition temperature of ferrocene, $>500\,°C$ [Xiong et al., 2004]). In addition, isooctane does not cause an immediate damage to human health and to the reactor system (plastic components of the reactor) in comparison with other compounds such as toluene or benzene.

Part III

RESULTS

AVÍS IMPORTANT

El text d'aquest capítol ha estat retirat seguint instruccions de l'autora de la tesi,
en existir participació d'empreses, existir conveni de confidencialitat o existeix
la possibilitat de generar patents

AVISO IMPORTANTE

*El texto de este capítulo ha sido retirado siguiendo instrucciones de la autora, al
existir participación de empresas, convenio de confidencialidad o la posibilidad
de generar patentes.*

IMPORTANT NOTICE

The text of this chapter has been withdrawn on the instructions of the author, as
there is participation of undertakings, confidentiality agreement or the ability to
generate patent

Part IV

CONCLUSIONS

9
Conclusions

- A modified arc–discharge plasma method was designed and developed in order to obtain carbon–encapsulated superparamagnetic iron nanoparticles showing narrow size distributions in core and primary total diameters. The controlled generation of this kind of nanoparticles allowed us the systematic study of their morphological, structural and magnetic properties and therefore, the understanding of important points in the nanoscience field, such as the growth mechanisms involved in the nanoparticle formation or the study of size–dependent properties.

- Preliminary results obtained in a conventional arc–discharge plasma reactor allowed us to design the modified arc–discharge plasma reactor in order to overcome several common drawbacks present in this technology:

  - The generation of nanoparticles at the expense of other structures, such as carbon nanotubs or carbon nanoparticles, among others.

  - The production of nanoparticles with narrow size distributions showing uniformity in their magnetic properties.

  - The high quality of the nanoparticles showing uniformity in their composition.

- Plackett–Burman statistical design was conducted in the conventional ADP reactor in order to evaluate the most significant reactor parameters to control iron core size distributions. Results showed that the arc current was the most influential reactor parameter. OES studies for the plasma characterisation in the modified ADP reactor pointed out the relation of the plasma temperature to the arc current used. The results showed the importance of the temperature in this kind of technology and its important role on the growth of nanoparticles, determining the cooling rate and hence, the residence time of nanoparticles.

- The effect of the arc current and thus, plasma temperature on the formation of Fe@C nanoparticles in the mADP reactor was studied from the morphological characterisation of the nanoparticles under microscopy observations:

  - Different growth mechanisms in the Fe core formation were identified depending on the plasma temperature (arc current used). Smaller Fe cores $< 6\,\text{nm}$ obtained by using lower arc currents ($< 30\,\text{A}$) seemed to grow by condensation of the iron atoms on the core surface (surface growth), while the growth of larger Fe cores obtained by using higher arc currents were mainly driven by coagulation and coalescence of two Fe cores. The increase of the Fe core diameters was associated to a plasma volume expansion when the arc current was increased, providing lower cooling rates and thus, longer residence times of the iron cores. At that point, Brownian collisions are more likely to occur promoting the coagulation and coalescence of Fe cores.

  - Concerning the carbon coating, elemental analysis results showed that carbon content increased exponentially with plasma temperature (with arc currents). Primary total size was observed to linearly increase with the plasma temperature (arc current). From both results, a critical Fe diameter for the formation of the carbon coating was determined ($D_{\text{cr,core}} \approx 4.8\,\text{nm}$).

  - We concluded that Fe@C nanoparticles in the mADP reactor were generated by both homogeneous and heterogeneous nucleation. First, the homogeneous nucleation of the Fe cores until a critical diameter was reached followed by the growth of the carbon coating. During this process, condensation, coagulation and coalescence occurred depending on the reactor parameter used.

- The effect of increasing the He flow rates was also studied. An increase of the cooling rate was observed due to the increase of the He flow rate. Despite some studies proposing that a high cooling rate promoted smaller nanoparticles, our results pointed out that a controlled quenching was more beneficial to produce high quality nanoparticles than rapid quenching in agreement with Joshi and cowokers [Joshi et al., 1990]. An increase of the geometric standard deviation was observed in Fe cores when the He flow rate was increased. In addition, the rapid quenching also affected the formation of the carbon coating promoting lower degree of carbon crystallinity (results found by Raman spectroscopy) and smaller total primary diameters.

- The effect of increasing ferrocene content was also investigated. Increasing ferrocene content at lower He flow rates (1.6 l/min) promoted larger iron cores. This was in agreement with theoretical studies carried out by Tashiro and coworkers [Tashiro et al., 2010], who observed that increasing the Fe vapours caused nucleation of iron nanoparticles occurred at higher temperatures. Nucleation at higher temperatures promoted longer

residence times for the iron cores resulting into larger diameters. At higher He flow rate (6.7 l/min) similar core size distributions were obtained avoiding the effect of nucleation at high temperatures. This was in agreement with theoretical studies from Aristizabal and coworkers [Aristizabal et al., 2006], who proposed that high He flow rates promoted the decrease of the metal vapour concentration by dilution, mixing the iron vapour with He gas.

- Magnetic studies of Fe@C nanoparticles obtained by the mADP confirmed results found in the morphological characterisation described above.

  - Nanoparticles presented superparamagnetic behaviour confirming the smaller Fe core diameters (< 10 nm) determined by microscopy observations.

  - The study of the magnetic properties as a function of the Fe core sizes confirmed the narrow size distribution of the samples obtained in the mADP reactor.

  - The determination of saturation magnetisation M_s=109 Am^2/kg, larger than values from iron oxides, from the size–dependence of the magnetic moments per Fe core using Langevin model, confirmed the protection of the iron cores from oxidation due to the carbon coating.

  - Variation of the magnetic moments for each sample agreed with the growth mechanisms observed in each case. Samples which grew by condensation (surface growth) showed a linear increase of the magnetic moment per Fe core with the Fe core size. Samples which mainly grew by coagulation of two Fe cores did not present any increase of the magnetic moment. Finally, samples grew by coalescence also showed an increase of the magnetic moment but the linear tendency was not clearly observed, pointing out the need to introduce an anisotropy energy and the Langevin model was not longer valid.

  - The size–dependence of coercivity at 5 K confirmed the single–domain behaviour of the Fe cores. Giant coercivity forces were not observed, confirming the assumption that Fe cores behaved as a single spin (Stoner–Wohlfarth model).

  - The ZFC curves fit to the Gittleman's model considering uniaxial Fe cores showed a linear increase of the blocking temperature with Fe core sizes, providing an anisotropy energy constant of about $5.4 \cdot 10^4$ J/m^3 very close to the Fe bulk value ($K_1 = 4.8 \cdot 10^4$ J/m^3), confirming the mainly composition of α-Fe of the cores. Some samples did not follow this dependence, due to the simplicity of the model. For instance, nanoparticles with lower amount of carbon and thus, lower distance among Fe cores, could present higher magnetic dipolar interactions, which are not considered in the Gittleman's model.

● The comparison of Fe@C nanoparticles obtained from the mADP and a chemical vapour deposition (CVD) were carried out. Some differences were observed related to the characteristics of the synthesis process. Concerning the iron core, CVD method produced nanoparticles with higher Fe size polydispersity than the mADP method. Concerning the carbon coating, nanoparticles from the CVD method presented higher degree of ordered carbon. However, we observed that after annealing, nanoparticles from mADP presented less significant changes in their properties, proving to be highly stable.

● A heat–treatment was conducted to nanoparticles produced by the mADP and CVD methods. A size–dependant behaviour was identified during the experiments. Fe cores showing diameters lower than 10 nm increased their size by Ostwald ripening, while Fe cores larger than 10 nm increased by coalescence. Those observations provided interesting features to take into account in future investigations about the growth mechanisms of nanoparticles.

● A first approach to biomedical applications was also carried out. First, an improvement of the Fe@C colloidal stability in aqueous solution was achieved by using polyvinyl–alcohol (PVA). Results from analytical disc centrifuge and microscopy observations agreed in the measurement of primary diameters of about 50 nm. Nanoparticles presented spherical shape of 50 nm containing several Fe cores, showing interesting characteristics for bio-magnetic applications. First studies about the internalisation of the nanoparticles into HeLa cells were also presented. Interactions of the nanoparticles with the cell membrane were better observed as we increased the positive surface charge of the nanoparticles. Although further studies are required, we could conclude that these first studies pointed that this kind of nanoparticles presents interesting characteristics for biomedical applications.

Bibliography

[Aguiló-Aguayo, 2007] Aguiló-Aguayo, N. (2007). Síntesi i caracterització de nanoestructures fe@c. Master's thesis, Universitat de Barcelona.

[Alcock et al., 1984] Alcock, C. B., Itkin, V. P., and Horrigan, M. K. (1984). Vapor pressure of the metallic elements. *Canadian Metallurgical Quarterly*, 23(3):309–313.

[Alekseyev and Dyuzhev, 2003] Alekseyev, N. and Dyuzhev, G. (2003). Fullerene formation in an arc discharge. *Carbon*, 41(7):1343–1348.

[Alim et al., 2005] Alim, K. A., Fonoberov, V. A., and Balandin, A. A. (2005). Origin of the optical phonon frequency shifts in zno quantum dots. *Applied Physics Letters*, 86(5):053103.

[Amer et al., 2010] Amer, M., O'Brien, P., Craighead, H., and Kroto, H. (2010). *Raman Spectroscopy, Fullerenes and Nanotechnology*. Rsc Nanoscience & Nanotechnology. Royal Society of Chemistry.

[Anderson, 1999] Anderson, A. J. (1999). The temperature dependence of the formal potential and the rate constant of the heterogeneous electron-transfer reaction of myoglobin. http://www.phattimes.com/myoglobin/index.html.

[Aristizabal et al., 2006] Aristizabal, F., Munz, R. J., and Berk, D. (2006). Modeling of the production of ultra fine aluminium particles in rapid quenching turbulent flow. *Journal of Aerosol Science*, 37:162–186.

[Atkinson et al., 2011] Atkinson, J. D., Fortunato, M. E., Dastgheib, S. A., Rostam-Abadi, M., Rood, M. J., and Suslick, K. S. (2011). Synthesis and characterization of iron-impregnated porous carbon spheres prepared by ultrasonic spray pyrolysis. *Carbon*, 49(2):587–598.

[Baker, 1976] Baker, R. (1976). *Graphite Ablation Chemistry Nonequilibrium Effects*. Defense Technical Information Center.

[Baker, 1989] Baker, R. (1989). Catalytic growth of carbon filaments. *Carbon*, 27(3):315–323.

[Baker et al., 1972] Baker, R., Barber, M., Harris, P., Feates, F., and Waite, R. (1972). Nucleation and growth of carbon deposits from the nickel catalyzed decomposition of acetylene. *Journal of Catalysis*, 26(1):51–62.

[Banhart et al., 1997] Banhart, F., Füller, T., Redlich, P., and Ajayan, P. (1997). The formation, annealing and self-compression of carbon onions under electron irradiation. *Chemical Physics Letters*, 269(3-4):349–355.

[Banhart et al., 1998] Banhart, F., Redlich, P., and Ajayan, P. (1998). The migration of metal atoms through carbon onions. *Chemical Physics Letters*, 292(4-6):554–560.

[Basu et al., 2012] Basu, S., Chatterjee, S., Bandyopadhyay, A., and Sarkar, K. (2012). Potential application of superparamagnetic nanoparticles for extraction of bacterial genomic dna from contaminated food and environmental samples. *Journal of the Science of Food and Agriculture*, pages 1–6.

[Batlle and Labarta, 2002] Batlle, X. and Labarta, A. (2002). Finite-size effects in fine particles: magnetic and transport properties. *Journal of Physics. D, Applied physics*, 35(6):R15–R42.

[Bean and Livingston, 1959] Bean, C. and Livingston, J. (1959). Superparamagnetism. *Journal of Applied Physics*, 30(4):120S–129S.

[Becker and Döring, 1935] Becker, R. and Döring, W. (1935). Kinetische behandlung der keimbildung in übersättigten dämpfen. *Annalen der Physik*, 416(8):719–752.

[Bera et al., 2006] Bera, D., Johnston, G., Heinrich, H., and Seal, S. (2006). A parametric study on the synthesis of carbon nanotubes through arc-discharge in water. *Nanotechnology*, 17(6):1722–1730.

[Bhushan, 2004] Bhushan, B., editor (2004). *Handbook of Nanotechnology*. Springer, Berlin.

[Biederman, 2004] Biederman, H. (2004). *Plasma Polymer Films*. Imperial College Press.

[Bilodeau et al., 1998] Bilodeau, J.-F., Pousse, J., and Gleizes, A. (1998). A mathematical model of the carbon arc reactor for fullerene synthesis. *Plasma Chemistry and Plasma Processing*, 18:285–303. 10.1023/A:1021658717860.

[Bilodeau and Proulx, 1996] Bilodeau, J.-F. and Proulx, P. (1996). A mathematical model for ultrafine iron powder growth in a thermal plasma. *Aerosol Science and Technology*, 24(3):175–189.

[Bogaerts et al., 2002] Bogaerts, A., Neyts, E., Gijbels, R., and van der Mullen, J. (2002). Gas discharge plasmas and their applications. *Spectrochimica Acta Part B: Atomic Spectroscopy*, 57(4):609–658.

[Bonard et al., 2001] Bonard, J., Seraphin, S., Wegrowe, J., Jiao, J., and Châtelain, A. (2001). Varying the size and magnetic properties of carbon–encapsulated cobalt particles. *Chemical Physics Letters*, 343(3–4):251–257.

[Bottani and Tascón, 2008] Bottani, E. and Tascón, J. (2008). *Adsorption By Carbons*. Chemical, Petrochemical & Process. Elsevier.

[Bowen, 2002] Bowen, P. (2002). Particle size distribution measurement from millimeters to nanometers and from rods to platelets. *Journal of Dispersion Science and Technology*, 23(5):631–662.

[Boyer and Meunier, 2012] Boyer, P. and Meunier, M. (2012). Modeling solvent influence on growth mechanism of nanoparticles (au, co) synthesized by surfactant free laser processes. *The Journal of Physical Chemistry C*, 116(14):8014–8019.

[Brown, 1994] Brown, S. (1994). *Basic Data of Plasma Physics: The Fundamental Data on Electrical Discharges in Gases*. American Vacuum Society Classics. American Institute of Physics.

[Buschow and Boer, 2003] Buschow, K. and Boer, F. (2003). *Physics of Magnetism and Magnetic Materials*. Focus on biotechnology. Kluwer Academic/Plenum Publishers.

[Butt et al., 2006] Butt, H., Graf, K., and Kappl, M. (2006). *Physics and Chemistry of Interfaces*. Physics textbook. John Wiley & Sons.

[Byeon and Kim, 2010] Byeon, J. H. and Kim, J.-W. (2010). Production of carbonaceous nanostructures from a silver–carbon ambient spark. *Applied Physics Letters*, 96(15):153102:1–3.

[Bystrzejewski et al., 2005] Bystrzejewski, M., Huçzko, A., and Lange, H. (2005). Arc plasma route to carbon–encapsulated magnetic nanoparticles for biomedical applications. *Sensors and Actuators B: Chemical*, 109(1):81–85.

[Bystrzejewski et al., 2009] Bystrzejewski, M., Pyrzynska, K., Huczko, A., and Lange, H. (2009). Carbon–encapsulated magnetic nanoparticles as separable and mobile sorbents of heavy metal ions from aqueous solutions. *Carbon*, 47(4):1189–1206.

[Byszewski et al., 1997] Byszewski, P., Lange, H., Huczko, A., and Behnke, J. F. (1997). Fullerene and nanotube synthesis. plasma spectroscopy studies. *Journal of Physics and Chemistry of Solids*, 58(11):1679–1683.

[Cao et al., 2000] Cao, Y., Chen, X., Li, J., Lan, Y., and Liang, J. (2000). Observation of a quantum-confinement effect with gan nanoparticles synthesized through a new gas reaction route. *Applied Physics A: Materials Science & Processing*, 71:229–231.

[Castaño-Bernal, 2008] Castaño-Bernal, J. (2008). Desarrollo y optimización de un reactor de depósito químico en fase vapor para la producción de nano-estructuras de carbono. Master's thesis, Universitat de Barcelona.

[Chaitoglou, 2012] Chaitoglou, S. (2012). Arc-discharge synthesis of fe@c nanoparticles for general applications. Master's thesis, Universitat de Barcelona.

[Challa et al., 2011] Challa, S. R., Delariva, A. T., Hansen, T. W., Helveg, S., Sehested, J., Hansen, P. L., Garzon, F., and Datye, A. K. (2011). Relating rates of catalyst sintering to the disappearance of individual nanoparticles during ostwald ripening. *Journal of the American Chemical Society*, 133(51):20672–20675.

[Chang, 2000] Chang, R. (2000). *Physical Chemistry for the Chemical and Biological Sciences*. University Science Books.

[Chapman, 1980] Chapman, B. (1980). *Glow discharge processes: sputtering and plasma etching*. Wiley-Interscience publication. Wiley.

[Chastellain et al., 2004] Chastellain, M., Petri, A., and Hofmann, H. (2004). Particle size investigations of a multistep synthesis of pva coated superparamagnetic nanoparticles. *Journal of Colloid and Interface Science*, 278(2):353–360.

[Chazelas et al., 2006] Chazelas, C., Coudert, J., Jarrige, J., and Fauchais, P. (2006). Synthesis of ultra fine particles by plasma transferred arc: Influence of anode material on particle properties. *Journal of the European Ceramic Society*, 26(16):3499–3507.

[Chen et al., 1998] Chen, C., Kitakami, O., and Shimada, Y. (1998). Particle size effects and surface anisotropy in fe-based granular films. *Journal of Applied Physics*, 84(4):2184–2188.

[Chen et al., 2009] Chen, D., Sanchez, A., Taboada, E., Roig, A., Sun, N., and Gu, H. (2009). Size determination of superparamagnetic nanoparticles from magnetization curve. *Journal of Applied Physics*, 105(083924):1–6.

[Chen et al., 2006] Chen, M., Kim, J., Liu, J. P., Fan, H., and Sun, S. (2006). Synthesis of fept nanocubes and their oriented self-assembly. *Journal of the American Chemical Society*, 128(22):7132–7133.

[Choi et al., 2002] Choi, C., Tolochko, O., and Kim, B. (2002). Preparation of iron nanoparticles by chemical vapor condensation. *Materials Letters*, 56(3):289–294.

[Choy, 2003] Choy, K. (2003). *Chemical vapour deposition of coatings*. Progress in materials science. Pergamon.

[Cifuentes et al., 2010] Cifuentes, Z., Custardoy, L., de la Fuente, J. M., Marquina, C., Ibarra, M. R., Rubiales, D., and de Luque, A. P. (2010). Absorption and translocation to the aerial part of magnetic carbon–coated nanoparticles through the root of different crop plants. *Journal of Nanobiotechnology*, 8(26):1–8.

[Clarck, 2007] Clarck, J. (2007). Intermolecular bonding – van der waals forces. http://www.chemguide.co.uk/atoms/bonding/vdw.html.

[Clarke and Braginski, 2007] Clarke, J. and Braginski, A. (2007). *The Squid Handbook: Applications of Squids and Squid Systems*, volume 2. John Wiley & Sons.

[CNEM, 2012] CNEM, m. (2012). Superparamagnetic nanoparticles. http://cnem.chem.ufl.edu/tinytech0015.html.

[Cooper, 1966] Cooper, J. (1966). Plasma spectroscopy. *Reports on Progress in Physics*, 29(1):35.

[CPSmanual,] CPSmanual. Cps disc centrifuge operating manual.

[Cullity and Graham, 2009] Cullity, B. and Graham, C. (2009). *Introduction to magnetic materials*. John Wiley & Sons, Inc., Hoboken, New Jersey, 2nd edition.

[Cullity and Stock, 2001] Cullity, B. and Stock, S. (2001). *Elements of x-ray diffraction*. Pearson education. Prentice Hall.

[Delalande et al., 2012] Delalande, M., Guinel, M. J.–F., Allard, L. F., Delattre, A., Le Bris, R., Samson, Y., Bayle–Guillemaud, P., and Reiss, P. (2012). L10 ordering of ultrasmall fept nanoparticles revealed by tem in situ annealing. *The Journal of Physical Chemistry C*, 116(12):6866–6872.

[Derjaguin and Landau, 1993] Derjaguin, B. and Landau, L. (1993). Theory of the stability of strongly charged lyophobic sols and of the adhesion of strongly charged particles in solutions of electrolytes. *Progress in Surface Science*, 43(1–4):30–59.

[Ding and Bolton, 2006] Ding, F. and Bolton, K. (2006). The importance of supersaturated carbon concentration and its distribution in catalytic particles for single–walled carbon nanotube nucleation. *Nanotechnology*, 17(2):543–548.

[Ding et al., 2004] Ding, F., Bolton, K., and Rosen, A. (2004). Iron–carbide cluster thermal dynamics for catalyzed carbon nanotube growth. *Journal of Vacuum Science Technology A: Vacuum, Surfaces, and Films*, 22(4):1471–1476.

[Dong et al., 1999] Dong, X., Zhang, Z., Jin, S., and Kim, B. (1999). Carbon-coated fe-co(c) nanocapsules prepared by arc discharge in methane. *Journal of Applied Physics*, 86(12):6701–6706.

[Dravid et al., 1995] Dravid, V., Host, J., Teng, M., Hwang, B., Johnson, D., Mason, T., and Weertman, J. (1995). Controlled-size nanocapsules. *Nature*, 347(6523):602.

[Du et al., 2010] Du, K., Ernst, F., Pelsozy, M., Barthel, J., and Tillmann, K. (2010). Expansion of interatomic distances in platinum catalyst nanoparticles. *Acta Materialia*, 58(3):836–845.

[Duffy and Blackman, 1998] Duffy, D. M. and Blackman, J. A. (1998). Magnetism of $3d$ transition-metal adatoms and dimers on graphite. *Physical Review B*, 58:7443–7449.

[Dukhin, 2010] Dukhin, A. (2010). Zeta potential.

[Dumitrache et al., 2004] Dumitrache, F., Morjan, I., Alexandrescu, R., Morjan, R., Voicu, I., I.Sandu, and et al. (2004). Nearly monodispersed carbon coated iron nanoparticles for the catalytic growth of nanotubesynanofibres. *Diamond and Related Materials*, 13(2):362–370.

[Egerton, 2009] Egerton, R. (2009). Electron energy-loss spectroscopy in the tem. *Reports on Progress in Physics*, 72(016502):1–25.

[Egerton, 2011] Egerton, R. (2011). *Electron Energy-Loss Spectroscopy in the Electron Microscope*. SpringerLink : Bücher. Springer.

[Einstein, 1905] Einstein, A. (1905). Über die von der molekularkinetischen theorie der wärme geforderte bewegung von in ruhenden flüssigkeiten suspendierten teilchen. *Annalen der Physik*, 322(8):549–560.

[EMS, 2011] EMS, E. M. S. (2011). Hamm - handbook of analytical methods for materials.

[Endo et al., 1998] Endo, M., Kim, C., Karaki, T., Tamaki, T., Nishimura, Y., Matthews, M. J., Brown, S. D. M., and Dresselhaus, M. S. (1998). Structural analysis of the b-doped mesophase pitch-based graphite fibers by raman spectroscopy. *Physical Review B*, 58:8991–8996.

[Fan and Ishigaki, 1997] Fan, X. and Ishigaki, T. (1997). Critical free energy for nucleation from the congruent melt of mosi2. *Journal of Crystal Growth*, 171(1-2):166–173.

[Fan et al., 2012] Fan, Z., Tao, X., Cui, X., Fan, X., Zhang, X., and Dong, L. (2012). Metal-filled carbon nanotube based optical nanoantennas: bubbling, reshaping, and in situ characterization. *Nanoscale*, 4:5673–5679.

[Fauth et al., 2004] Fauth, K., Gold, S., Hebler, M., Schneider, N., and Schütz, G. (2004). Cluster surface interactions: small fe clusters driven nonmagnetic on graphite. *Chemical Physics Letters*, 392(4-6):498–502.

[FEI, 2012] FEI (2012). An introduction to electron microscopy.

[Ferguson et al., 2004] Ferguson, F. T., Nuth, J. A., and Johnson, N. M. (2004). Thermogravimetric measurement of the vapor pressure of iron from 1573 k to 1973 k. *J. Chem. Eng. Data*, 49(3):497–501.

[Ferrari, 2007] Ferrari, A. (2007). Raman spectroscopy of graphene and graphite: Disorder, electron–phonon coupling, doping and nonadiabatic effects. *Solid State Communications*, 143(1-2):47–57.

[Ferrari and Robertson, 2000] Ferrari, A. and Robertson, J. (2000). Interpretation of raman spectra of disordered and amorphous carbon. *Physical Review B*, 61(20):14095–14107.

[Flagan and Lunden, 1995] Flagan, R. C. and Lunden, M. M. (1995). Particle structure control in nanoparticle synthesis from the vapor phase. *Materials Science and Engineering: A*, 204(1-2):113–124. Proceedings of the Symposium on Engineering of Nanostructured Materials.

[Foundry, 2012] Foundry, D. (2012). Compacted (vermicular) graphite iron castings. http://www.castironcastings.com/compacted-graphite-iron.html.

[Fridman, 2008] Fridman, A. (2008). *Plasma Chemistry*. Cambridge University Press.

[Fukuhara, 2003] Fukuhara, M. (2003). Lattice expansion of nanoscale compound particles. *Physics Letters A*, 313(5-6):427–430.

[Gangopadhyay et al., 1992] Gangopadhyay, S., Hadjipanayis, G., Dale, B., Sorensen, M., Klabunde, K., Papaefthymiou, V., and Kostikas, A. (1992). Magnetic properties of ultrafine iron particles. *Physical Review. B, Condensed Matter*, 45(17):9778–9787.

[Gfroerer, 2006] Gfroerer, T. H. (2006). *Photoluminescence in Analysis of Surfaces and Interfaces*. John Wiley & Sons, Ltd.

[Ghosh., 2011] Ghosh., S. K. (2011). Kubo gap as a factor governing the emergence of new physicochemical characteristics of the small metallic particulates. *Assam University Journal of Science and Technology*, 7:229–231.

[Gibbs et al., 1902] Gibbs, J., Bumstead, H., Van Name, R., and Longley, W. (1902). *The collected works of J. Willard Gibbs*, volume 2 of *The Collected Works of J. Willard Gibbs*. Longmans, Green and Co.

[Girshick and Chiu, 1989] Girshick, S. and Chiu, C. (1989). Homogeneous nucleation of particles from the vapor phase in thermal plasma synthesis. *Plasma Chemistry and Plasma Processing*, 9:355–369. 10.1007/BF01083672.

[Girshick et al., 1993] Girshick, S., Chiu, C.-P., Muno, R., Wu, C., Yang, L., Singh, S., and McMurry, P. (1993). Thermal plasma synthesis of ultrafine iron particles. *Journal of Aerosol Science*, 24(3):367–382.

[Girshick et al., 1988] Girshick, S. L., Chiu, C.-P., and McMurry, P. H. (1988). Modelling particle formation and growth in a plasma synthesis reactor. *Plasma Chemistry and Plasma Processing*, 8:145–157. 10.1007/BF01016154.

[Gittleman et al., 1974] Gittleman, J. I., Abeles, B., and Bozowski, S. (1974). Superparamagnetism and relaxation effects in granular ni–sio$_2$ and ni–al$_2$o$_3$ films. *Physical Review B*, 9:3891–3897.

[Goldfarb and Fickett, 1985] Goldfarb, R. and Fickett, F. (1985). Magnetic units.

[Goldstein, 2003] Goldstein, J. (2003). *Scanning Electron Microscopy and X-Ray Microanalysis*. Kluwer Academic/Plenum Publishers.

[Goodhew et al., 2001] Goodhew, P., Humphreys, F., and Beanland, R. (2001). *Electron Microscopy and Analysis*. Taylor & Francis.

[Gosh, 2009] Gosh, P. (2009). *Colloid And Interface Science*. Prentice-Hall Of India Pvt. Limited.

[Granqvist and Buhrman, 1976] Granqvist, C. and Buhrman, R. (1976). Log–normal size distributions of ultrafine metal particles. *Solid State Communications*, 18(1):123–126.

[Granqvist et al., 2004] Granqvist, C., Kish, L., and Marlow, W. (2004). *Gas Phase Nanoparticle Synthesis*. Kluwer Academic Publishers.

[Grass et al., 2007] Grass, R., Athanassiou, E., and Stark, W. (2007). Covalently functionalized cobalt nanoparticles as a platform for magnetic separations in organic synthesis. *Angewandte Chemie International Edition*, 46(26):4909–4912.

[Gratton et al., 2008] Gratton, S. E. A., Ropp, P. A., Pohlhaus, P. D., Luft, J. C., Madden, V. J., Napier, M. E., and DeSimone, J. M. (2008). The effect of particle design on cellular internalization pathways. *Proceedings of the National Academy of Sciences*, 105(33):11613–11618.

[Gubarevich et al., 2003] Gubarevich, A. V., Kitamura, J., Usuba, S., Yokoi, H., Kakudate, Y., and Odawara, O. (2003). Onion-like carbon deposition by plasma spraying of nanodiamonds. *Carbon*, 41(13):2601–2606.

[Gubin, 2009] Gubin, S., editor (2009). *Introduction to magnetic materials*. Wiley-VCH Verlag GmbH & Co. KGaA, Weinheim, Germany.

[Gundel et al., 1991] Gundel, H., Hantzsche, E., and Hess, H. (1991). Low temperature plasmas. *European Journal of Physics*, 12(1):39.

[Guo et al., 1995] Guo, T., Nikolaev, P., Rinzler, A. G., Tomanek, D., Colbert, D. T., and Smalley, R. E. (1995). Self-assembly of tubular fullerenes. *The Journal of Physical Chemistry*, 99(27):10694–10697.

[Gustch et al., 2002] Gustch, A., Krämer, M., Michael, G., Mühlenweg, H., Pridöhl, M., and Zimmermann, G. (2002). Gas-phase production of nanoparticles. *KONA: Powder and Particle Journal*, 20:24–37.

[Hailstone et al., 2009] Hailstone, R. K., DiFrancesco, A. G., Leong, J. G., Allston, T. D., and Reed, K. J. (2009). A study of lattice expansion in ceo2 nanoparticles by transmission electron microscopy. *The Journal of Physical Chemistry C*, 113(34):15155–15159.

[Hansen and Morup, 1999] Hansen, M. and Morup, S. (1999). Estimation of blocking temperatures from zfc/fc curves. *Journal of Magnetism and Magnetic Materials*, 203(1-3):214–216.

[Hellebusch et al., 2010] Hellebusch, D., Manthiram, K., and Webb, M. (2010). Ion distribution near a liquid-liquid interface. http://www.cchem.berkeley.edu/molsim/teaching/fall2010/iondistribution/models.htm.

[Hemming, 2007] Hemming, P. (2007). Chn micro-analysis: a comparative review of the effects of instrument design on analytical performance.

[Hendriksen et al., 1994] Hendriksen, P., Linderoth, S., Oxborrow, C., and Morup, S. (1994). Ultrafine maghemite particles: Ii. the spin-canting effect revisited. *Journal of Physics. Condensed Matter*, 6(16):3091–3100.

[Hergt et al., 2006] Hergt, R., Dutz, S., Müller, R., and Zeisberger, M. (2006). Magnetic particle hyperthermia: nanoparticle magnetism and materials development for cancer therapy. *Journal of Physics: Condensed Matter*, 18(38):S2919.

[Hesselink, 2012] Hesselink, J. R. (2012). Basic principles of mr imaging. http://spinwarp.ucsd.edu/neuroweb/Text/br-100.htm.

[Hornyak et al., 2008] Hornyak, G., Dutta, J., Tibbals, H., and Rao, A. (2008). *Introduction to Nanoscience*. CRC press/Taylor & Francis Group, Boca Raton, Florida, US.

[Host et al., 1998] Host, J. J., Block, J. A., Parvin, K., Dravid, V. P., Alpers, J. L., Sezen, T., and LaDuca, R. (1998). Effect of annealing on the structure and magnetic properties of graphite encapsulated nickel and cobalt nanocrystals. *Journal of Applied Physics*, 83(2):793–801.

[Hou et al., 2002] Hou, H., Schaper, A., Weller, F., and Greiner, A. (2002). Carbon nanotubes and spheres produced by modified ferrocene pyrolysis. *Chemistry of Materials*, 14(9):3990–3994.

[Hsing et al., 2007] Hsing, I.-M., Xu, Y., and Zhao, W. (2007). Micro- and nano- magnetic particles for applications in biosensing. *Electroanalysis*, 19(7-8):755–768.

[Huang et al., 2007] Huang, Z., Thomson, P., and Di, S. (2007). Lattice contractions of a nanoparticle due to the surface tension: A model of elasticity. *Journal of Physics and Chemistry of Solids*, 68(4):530 – 535.

[Huczko et al., 1997] Huczko, A., Lange, H., Byszewski, P., Poplawska, M., and Starski, A. (1997). Fullerene formation in carbon arc: Electrode gap dependence and plasma spectroscopy. *The Journal of Physical Chemistry A*, 101(7):1267–1269.

[Hunter, 1981] Hunter, R. (1981). *Zeta Potential in Colloid Science: Principles and Applications*. Colloid science. Academic Press.

[Hunter, 2001] Hunter, R. (2001). *Foundations of Colloid Science*. Foundations of Colloid Science. Oxford University Press, USA.

[Imego, 2005] Imego (2005). Magnetic nanoparticles. http://www.imego.com/Expertise/electromagnetic-sensors-and-systems/magnetic-nanoparticles.aspx.

[Inc., 1999] Inc., S. (1999). Chapter 7: Basics of x-ray diffraction.

[Instruments, 2006] Instruments, C. (2006). Elemental combustion system chns-o.

[Irvine, 1967] Irvine, T. (1967). *Advances in Heat Transfer*, volume 4 of *Serial Publication Series*. Elsevier Science.

[Israelachvili, 2011a] Israelachvili, J. (2011a). *Intermolecular and Surface Forces: Revised Third Edition*. Academic Press. Elsevier Science.

[Israelachvili, 2011b] Israelachvili, J. (2011b). *Intermolecular and Surface Forces: Revised Third Edition*. Academic Press. Elsevier Science.

[Jackson and Hargreaves, 2009] Jackson, S. and Hargreaves, J. (2009). *Metal Oxide Catalysis*, volume 2 of *Metal Oxide Catalysis*. Wiley-VCH.

[Jiang et al., 2009] Jiang, J., Oberdörster, G., and Biswas, P. (2009). Characterization of size, surface charge, and agglomeration state of nanoparticle dispersions for toxicological studies. *Journal of Nanoparticle Research*, 11:77–89.

[Jiao and Seraphin, 1998] Jiao, J. and Seraphin, S. (1998). Carbon encapsulated nanoparticles of ni, co, cu, and ti. *Journal of Applied Physics*, 83(5):2442–2448.

[José-Yacamán et al., 2005] José-Yacamán, M., Gutierrez-Wing, C., Miki, M., Yang, D. Q., Piyakis, K. N., and Sacher, E. (2005). Surface diffusion and coalescence of mobile metal nanoparticles. *The Journal of Physical Chemistry B*, 109(19):9703–9711. PMID: 16852169.

[Joshi et al., 1990] Joshi, S. V., Liang, Q., Park, J. Y., and Batdorf, J. A. (1990). Effect of quenching conditions on particle formation and growth in thermal plasma synthesis of fine powders. *Plasma Chemistry and Plasma Processing*, 10:339–358. 10.1007/BF01447135.

[Joy et al., 1986] Joy, D., Romig, A., and Goldstein, J. (1986). *Principles of Analytical Electron Microscopy*. Plenum Press.

[Jung et al., 2010] Jung, D., Park, S., and Kang, Y. (2010). Design of particles by spray pyrolysis and recent progress in its application. *Korean Journal of Chemical Engineering*, 27:1621–1645. 10.1007/s11814-010-0402-5.

[Jäger et al., 2006] Jäger, C., Mutschke, H., Huisken, F., Alexandrescu, R., Morjan, I., Dumitrache, F., Barjega, R., Soare, I., David, B., and Schneeweiss, O. (2006). Iron–carbon nanoparticles prepared by co_2 laser pyrolysis of toluene and iron pentacarbonyl. *Applied Physics A: Materials Science & Processing*, 85:53–62. 10.1007/s00339-006-3665-2.

[Kachkachi and Garanin, 2005] Kachkachi, H. and Garanin, D. A. (2005). In Fionari, D., editor, *Surface effects in magnetic nanoparticles*, chapter Magnetic nanoparticles in many–spin systems. Springer Science+Business Media, Inc., New York, USA.

[Kahlweit, 1965] Kahlweit, M. (1965). Ageing of precipitates by ostwald ripening. *Angewandte Chemie International Edition in English*, 4(5):444–445.

[Kelly et al., 1984] Kelly, T., Cohen, M., and vander Sande, J. (1984). Rapid solidification of a droplet-processed stainless steel. *Metallurgical and Materials Transactions A*, 15:819–833. 10.1007/BF02644556.

[Kholodenko and Douglas, 1995] Kholodenko, A. L. and Douglas, J. F. (1995). Generalized stokes-einstein equation for spherical particle suspensions. *Physical Review E*, 51:1081–1090.

[Kiang et al., 1995] Kiang, C.-H., III, W. A. G., Beyers, R., and Bethune, D. S. (1995). Carbon nanotubes with single–layer walls. *Carbon*, 33(7):903–914.

[Kirkwood, 1979] Kirkwood, T. (1979). Geometric means and measures of dispersion. *Biometrics*, 35:908–909.

[Kittel, 1971] Kittel, C. (1971). *Introduction to solid state physics*. Wiley.

[Kneller and Luborsky, 1963] Kneller, E. F. and Luborsky, F. E. (1963). Particle size dependence of coercivity and remanence of single-domain particles. *Journal of Applied Physics*, 34(3):656–658.

[Knobel et al., 2008] Knobel, M., Nunes, W., Socolovsky, L., Biasi, E. D., Vargas, J., and Denardin, J. (2008). Superparamagnetism and other magnetic features in granular materials: a review on ideal and real systems. *Journal of Nanoscience and Nanotechnology*, 8(6):2836–2857.

[Kodama, 1999] Kodama, R. (1999). Magnetic nanoparticles. *Journal of Magnetism and Magnetic Materials*, 200(1-3):359–372.

[Kovács et al., 2004] Kovács, G., Sáfrán, G., Geszti, O., Ujvári, T., Bertóti, I., and Radnóczi, G. (2004). Structure and mechanical properties of carbon‚Äìnickel and cnx‚Äìnickel nanocomposite films. *Surface and Coatings Technology*, 180-181(0):331–334.

[Kramer, 2007] Kramer, C. (2007). *Fullerene Research Advances*. Nova Science Publishers.

[Kruis et al., 1997] Kruis, F., Fissan, H., and Peled, A. (1997). Synthesis of nanoparticles in the gas phase for electronic, optical and magnetic applications - a review. *Journal of Aerosol Science*, 29(5/6):511–535.

[Krästchmer et al., 1990] Krästchmer, W., Lamb, L., and Fostiropoulos, K. (1990). Solid c_{60}: a new form of carbon. *Nature*, 347:354–357.

[Kubo, 1962] Kubo, R. (1962). Electronic properties of metallic fine particles. i. *Journal of the Physical Society of Japan*, 17(6):975–986.

[Kumar, 2011] Kumar, M. (2011). Carbon nanotube synthesis and growth mechanism. In Yellampalli, S., editor, *Carbon Nanotubes - Synthesis, Characerization, Applications*, pages 147–170. InTech.

[Kumar et al., 511] Kumar, N., Dash, S., Tyagi, A., and Raj, B. (493-511). Dynamics of plasma expansion in the pulsed laser material interaction. *Sadhana-academy proceedings in engineering sciences*, 35.

[Kwong et al., 2010] Kwong, H. Y., Wong, M. H., Leung, C. W., Wong, Y. W., and Wong, K. H. (2010). Formation of core/shell structured cobalt/carbon nanoparticles by pulsed laser ablation in toluene. *Journal of Applied Physics*, 108(3):034304.

[Lai et al., 2009] Lai, G.-S., Zhang, H.-L., and Han, D.-Y. (2009). Amperometric hydrogen peroxide biosensor based on the immobilization of horseradish peroxidase by carbon-coated iron nanoparticles in combination with chitosan and cross-linking of glutaraldehyde. *Microchimica Acta*, 165:159–165.

[Lai et al., 2012] Lai, L. M. H., Goon, I. Y., Chuah, K., Lim, M., Braet, F., Amal, R., and Gooding, J. J. (2012). The biochemiresistor: An ultrasensitive biosensor for small organic molecules. *Angewandte Chemie International Edition*, 124(26):6562–6565.

[Lane, 2006] Lane, D. M. (1993-2006). Chapter 18 measuring effect size.

[Lange, 1997] Lange, H. (1997). Spectral diagnostics of helium–carbon arc plasma during carbon nanostructure formation. *Fullerene Science and Technology*, 5(6):1177–1201.

[Lange et al., 1999a] Lange, H., Huczko, A., Noworyta, K., and Byszewski, P. (1999a). Carbon-iron arc plasma: Characterization and novel applications. *Czechoslovak Journal of Physics*, 49:933–940. 10.1023/A:1021472818324.

[Lange et al., 1999b] Lange, H., Saidane, K., Razafinimanana, M., and Gleizes, A. (1999b). Temperatures and c 2 column densities in a carbon arc plasma. *Journal of Physics D: Applied Physics*, 32(9):1024.

[Langford and Wilson, 1978] Langford, J. I. and Wilson, A. J. C. (1978). Scherrer after sixty years: A survey and some new results in the determination of crystallite size. *Journal of Applied Crystallography*, 11(2):102–113.

[Laplaze et al., 2002] Laplaze, D., Alvarez, L., Guillard, T., Badie, J., and Flamant, G. (2002). Carbon nanotubes: dynamics of synthesis processes. *Carbon*, 40(10):1621–1634.

[Laurent et al., 1998] Laurent, C., Flahaut, E., Peigney, A., and Rousset, A. (1998). Metal nanoparticles for the catalytic synthesis of carbon nanotubes. *New Journal of Chemistry*, 22(11):1229–1937.

[Ledoux et al., 2000] Ledoux, G., Guillois, O., Porterat, D., Reynaud, C., Huisken, F., Kohn, B., and Paillard, V. (2000). Photoluminescence properties of silicon nanocrystals as a function of their size. *Physical Review B*, 62:15942–15951.

[Lee et al., 2009] Lee, D. H., Lee, W. J., and Kim, S. O. (2009). Vertical single-walled carbon nanotube arrays via block copolymer lithography. *Chemistry of Materials*, 21(7):1368–1374.

[Lee et al., 2005] Lee, J., Jin, S., Hwang, Y., Park, J., Park, H., and Hyeon, T. (2005). Simple synthesis of mesoporous carbon with magnetic nanoparticles embedded in carbon rods. *Carbon*, 43(12):2536–2543.

[Lemons and Gythiel, 1997] Lemons, D. S. and Gythiel, A. (1997). Paul langevin's 1908 paper *On the Theory of Brownian Motion*, *Sur la théorie du mouvement brownien*, c. r. acad. sci. (paris) [bold 146], 530–533 (1908)]. *American Journal of Physics*, 65(11):1079–1081.

[Leslie-Pelecky and Rieke, 1996] Leslie-Pelecky, D. L. and Rieke, R. D. (1996). Magnetic properties of nanostructured materials. *Chemistry of Materials*, 8(8):1770–1783.

[Li et al., 2009a] Li, F.-r., Yan, W.-h., Guo, Y.-h., Qi, H., and Zhou, H.-x. (2009a). Preparation of carboplatin-fe@c-loaded chitosan nanoparticles and study on hyperthermia combined with pharmacotherapy for liver cancer. *International Journal of Hyperthermia*, 25(5):383–91.

[Li et al., 2009b] Li, Z., Hu, C., Yu, C., and Qiu, J. (2009b). Synthesis and characterization of carbon-encapsulated magnetic nanoparticles via arc-plasma assisted cvd. *Journal of Nanoscience and Nanotechnology*, 9(12):7473–7476.

[Lifshitz and Slyozov, 1961] Lifshitz, I. and Slyozov, V. (1961). The kinetics of precipitation from supersaturated solid solutions. *Journal of Physics and Chemistry of Solids*, 19(1–2):35–50.

[Lindgren, 1999] Lindgren, E. R. (1999). The motion of a sphere in an incompressible viscous fluid at reynolds numbers considerably less than one. *Physica Scripta*, 60(2):97.

[Liu et al., 1993] Liu, F., Khanna, S. N., Magaud, L., Jena, P., de Coulon, V., Reuse, F., Jaswal, S. S., He, X.-G., and Cyrot-Lackman, F. (1993). Magnetism of al-mn quasicrystals. *Physical Review B*, 48:1295–1298.

[Liu et al., 2010] Liu, H., Hua, M. Y., Yang, H. W., Huang, C. Y., Chu, P. C., Wu, J. S., Tseng, I. C., Wang, J. J., Yen, T. C., Chen, P. Y., and Wei, K. C. (2010). Magnetic resonance monitoring of focused ultrasound/magnetic nanoparticle targeting delivery of therapeutic agents to the brain. *Proceedings of the National Academy of Sciences of the United States of America*, 107:15205–15210.

[Liu et al., 2001] Liu, Z. J., Yuan, Z. Y., Zhou, W., Xu, Z., and Peng, L. M. (2001). Controlled synthesis of carbon-encapsulated co nanoparticles by cvd. *Chemical Vapor Deposition*, 7(6):248–251.

[Lothe and Pound, 1962] Lothe, J. and Pound, G. M. (1962). Reconsiderations of nucleation theory. *The Journal of Chemical Physics*, 36(8):2080–2085.

[Lu et al., 2007] Lu, A., Salabas, E., and Schüth, F. (2007). Magnetic nanoparticles: synthesis, protection, functionalization, and application. *Angewandte Chemie International Edition*, 46(8):1222–1244.

[Lu et al., 2005] Lu, Y., Zhu, Z., and Liu, Z. (2005). Carbon-encapsulated fe nanoparticles from detonation-induced pyrolysis of ferrocene. *Carbon*, 43(2):369–374.

[Lyklema, 1995] Lyklema, J. (1995). *Fundamentals of Interface and Colloid Science: Solid-Liquid Interfaces*. Fundamentals of Interface and Colloid Science. Academic Press.

[Mahl et al., 2011] Mahl, D., Diendorf, J., Meyer-Zaika, W., and Epple, M. (2011). Possibilities and limitations of different analytical methods for the size determination of a bimodal dispersion of metallic nanoparticles. *Colloids and Surfaces A: Physicochemical and Engineering Aspects*, 377(1-3):386–392.

[Majetich et al., 1995] Majetich, S., Brunsman, E., Scott, J., and McHenry, M. E. (1995). Formation of nanoparticles in a carbon arc. *Materials Science and Engineering A-structural Materials Properties MIcrostructure and Processing*, 204(1-2):29–34.

[Marikani, 2009] Marikani, A. (2009). *Engineering Physics*. Prentice-Hall Of India Pvt. Ltd.

[Marsh and Rodríguez-Reinoso, 2006] Marsh, H. and Rodríguez-Reinoso, F. (2006). *Activated carbon*. Elsevier, London.

[Marshall and Norton, 1950] Marshall, A. L. and Norton, F. J. (1950). Carbon vapor pressure and heat of vaporization. *Journal of the American Chemical Society*, 72(5):2166–2171.

[McNeil, 2005] McNeil, S. (2005). Nanotechnology for the biologist. *Journal of Leukocyte Biology*, 78:585–594.

[Millan et al., 2007] Millan, A., Urtizberea, A., Silva, N., Palacio, F., Amaral, V., Snoeck, E., and Serin, V. (2007). Surface effects in maghemite nanoparticles. *Journal of Magnetism and Magnetic Materials*, 312(4):L5–L9.

[Mokari et al., 2005] Mokari, T., Sztrum, C., Salant, A., Rabani, E., and Bannin, U. (2005). Formation of asymmetric one–sided metal–tipped semiconductor nanocrystal dots and rods. *Nature Materials*, 4(11):855–863.

[Montano et al., 1986] Montano, P. A., Shenoy, G. K., Alp, E. E., Schulze, W., and Urban, J. (1986). Structure of copper microclusters isolated in solid argon. *Physical Review Letters*, 56:2076–2079.

[Moody and Attard, 2002] Moody, M. P. and Attard, P. (2002). Homogeneous nucleation of droplets from a supersaturated vapor phase. *The Journal of Chemical Physics*, 117(14):6705–6714.

[Moreno-Castilla, 2004] Moreno-Castilla, C. (2004). Adsorption of organic molecules from aqueous solutions on carbon materials. *Carbon*, 42(1):83–94.

[Morup et al., 1995] Morup, S., Bodker, F., Hendriksen, P., and Linderoth, S. (1995). Spin–glass-like ordering of the magnetic moments of interacting nanosized maghemite particles. *Physical Review B*, 52(1):287–294.

[Mostofizadeh et al., 2010] Mostofizadeh, A., Li, Y., Song, B., and Huang, Y. (2010). Synthesis, properties, and applications of low-dimensional carbon-related nanomaterials. *Journal of Nanomaterials*, 2011:1–21.

[Mukadam et al., 2008] Mukadam, M. D., Kumar, A., Yusuf, S. M., Yakhmi, J. V., Tewari, R., and Dey, G. K. (2008). Spin-glass behavior in ferromagnetic fe[fe(cn)$_6$]·xh$_2$o nanoparticles. *Journal of Applied Physics*, 103(12):123902.

[Murooka and Hearne, 1972] Murooka, Y. and Hearne, K. R. (1972). Measurement of arc electrode temperatures and reignition characteristics. *Journal of Applied Physics*, 43(6):2656–2663.

[NERL, 2010] NERL, m. (2010). Reference solar spectra irradiance: Air mass 1.5.

[Nicolson, 1955] Nicolson, M. M. (1955). Surface tension in ionic crystals. *Proceedings of the Royal Society of London A*, 228(1175):490–510.

[Nishijo et al., 2006] Nishijo, J., Okabe, C., Oishi, O., and Nishi, N. (2006). Synthesis, structures and magnetic properties of carbon-encapsulated nanoparticles via thermal decomposition of metal acetylide. *Carbon*, 44(14):2943–2949.

[NIST, 2009] NIST (2009). Nist atomic spectra database.

[NIST/SEMATECH, 2007] NIST/SEMATECH (2007). e-handbook of statistical methods.

[Néel, 1949] Néel, L. (1949). Théorie du traînage magnétique des ferromagnétiques en grains fins avec application aux terres cuites. *Annales de Géophysique*, 5:99–136.

[Oberlin et al., 1976] Oberlin, A., Endo, M., and Koyama, T. (1976). Filamentous growth of carbon through benzene decomposition. *Journal of Crystal Growth*, 32(3):335–349.

[Obraztsova et al., 1998] Obraztsova, E., Fujii, M., Hayashi, S., Kuznetsov, V., Butenko, Y., and Chuvilin, A. (1998). Raman identification of onion-like carbon. *Carbon*, 36(5-6):821–826.

[Oehlert, 2000] Oehlert, G. (2000). *A First Course in Design and Analysis of Experiments*. W.H. Freeman.

[of Standards et al., 1980] of Standards, U. N.-B., Burris, B., and Morehouse, R. (1980). *Publications of the National Bureau of Standards, 1979 catalog: a compilation of abstracts and key word and author indexes*. NBS special publication. U.S. Dept. of Commerce, National Bureau of Standards.

[Ostrovskaya et al., 2003] Ostrovskaya, L., Perevertailo, V., Matveeva, L., Milani, P., Ralchenko, V., and Shpilevsky, E. (2003). Characterization of different carbon nanomaterials promising for biomedical and sensor applications by the wetting method. *Powder Metallurgy and Metal Ceramics*, 42(1-2):1–8.

[Palmer and Shelef, 1968] Palmer, H. B. and Shelef, M. (1968). Vaporization of carbon. *Chemistry of Physics of Carbon*, 4:95–135.

[Park, 2008] Park, J. (2008). *Structural Characterization of Hard Materials by Transmission Electron Microscopy (TEM): Diamond-Silicon Carbide Composites and Yttria-stabilized Zirconia.* Stanford University.

[Park et al., 2008] Park, J., Jeong, S., Jeong, M., Kim, J., and Cho, B. (2008). Synthesis of carbon–encapsulated magnetic nanoparticles by pulsed laser irradiation of solution. *Carbon*, 46(11):1369–1377.

[Parsegian, 2005] Parsegian, V. (2005). *Van der Waals Forces: A Handbook for Biologists, Chemists, Engineers, and Physicists.* Cambridge University Press.

[Pellicer et al., 2000] Pellicer, J., García-Morales, V., and Hernández, M. J. (2000). On the demonstration of the young–laplace equation in introductory physics courses. *Physics Education*, 35(2):126.

[Petri-Fink et al., 2008] Petri-Fink, A., Steitz, B., Finka, A., Salaklang, J., and Hofmann, H. (2008). Effect of cell media on polymer coated superparamagnetic iron oxide nanoparticles (spions): Colloidal stability, cytotoxicity, and cellular uptake studies. *European Journal of Pharmaceutics and Biopharmaceutics*, 68(1):129–137.

[Pham-Huu et al., 2008] Pham-Huu, C., Ersen, O., and Ledoux, M.-J. (2008). *Carbon and Silicon Carbide Nanotubes Containing Catalysts*, pages 219–252. Wiley-VCH Verlag GmbH & Co. KGaA.

[Pimenta et al., 2007] Pimenta, M. A., Dresselhaus, G., Dresselhaus, M. S., Cancado, L. G., Jorio, A., and Saito, R. (2007). Studying disorder in graphite-based systems by raman spectroscopy. *Physical Chemistry Chemical Physics*, 9:1276–1290.

[Pomogailo and Kestelman, 2005] Pomogailo, A. and Kestelman, V. (2005). *Metallopolymer Nanocomposites*, volume 81 of *Springer Series in Materials Science*. Springer, Berlin, Heiderlberg, New York, 1 edition.

[Poplawska et al., 2010] Poplawska, M., Zukowska, G., Cudzilo, S., and Bystrzejewski, M. (2010). Chemical functionalization of carbon–encapsulated magnetic nanoparticles by 1,3–dipolar cycloaddition of nitrile oxide. *Carbon*, 48(4):1318–1320.

[Qi and Wang, 2005] Qi, W. H. and Wang, M. P. (2005). Size and shape dependent lattice parameters of metallic nanoparticles. *Journal of Nanoparticle Research*, 7:51–57. 10.1007/s11051-004-7771-9.

[qiang Wei et al., 2011] qiang Wei, Z., gang Liu, L., Yang, H., rong Zhang, C., and jun Feng, W. (2011). Characterization of carbon encapsulated fe-nanoparticles prepared by confined arc plasma. *Transactions of Nonferrous Metals Society of China*, 21(9):2026–2030.

[Reimer, 1998] Reimer, L. (1998). *Scanning Electron Microscopy: Physics of Image Formation and Microanalysis*. Springer Series in Optical Sciences. Springer.

[Reimer and Kohl, 2008] Reimer, L. and Kohl, H. (2008). *Transmission Electron Microscopy: Physics of Image Formation*. Springer Series in Optical Sciences. Springer.

[Reiss and Hutter, 2005] Reiss, G. and Hutter, A. (2005). Magnetic nanoparticles: Applications beyond data storage. *Nature Materials*, 4:725–726.

[Ricci and Braga, 2003] Ricci, D. and Braga, P. C. (2003). Imaging methods in atomic force microscopy.

[Richter and Schwedt, 2008] Richter, S. and Schwedt, A. (2008). *EMC 2008: Vol 2: Materials Science*. EMC 2008: 14th European Microscopy Congress, 1-5 September 2008, Aachen, Germany. Springer.

[Roduner, 2006] Roduner, E. (2006). Size matters: why nanomaterials are different. *Chem. Soc. Rev.*, 35:583–592.

[Roduner and Cronin, 2006] Roduner, E. and Cronin, L. (2006). *Nanoscopic Materials: Size-Dependent Phenomena*. RSC nanoscience & nanotechnology. Royal Society of Chemistry.

[Rohlfing, 1988] Rohlfing, E. A. (1988). Optical emission studies of atomic, molecular, and particulate carbon produced from a laser vaporization cluster source. *The Journal of Chemical Physics*, 89(10):6103–6112.

[Saito, 1995] Saito, Y. (1995). Nanoparticles and filled nanocapsules. *Carbon*, 33(7):979–988.

[Saito et al., 1994] Saito, Y., Yoshikawa, T., Okuda, M., and Fujimoto, N. (1994). Cobalt particles wrapped in graphitic carbon prepared by an arc discharge method. *Journal of Applied Physics*, 75(1):134–137.

[Sato et al., 2001] Sato, K., Furukawa, Y., and Nakajima, K. (2001). *Advances in Crystal Growth Research*. North-Holland.

[Sattler, 2010b] Sattler, K. (2010b). *Principles and Methods*. Handbook of Nanophysics. Taylor & Francis.

[Sattler, 2010a] Sattler, K., editor (September 2010a). *Handbook of Nanophysics: Clusters and Fullerenes*. CRC Press, University of Hawaii-Manoa, Honolulu, USA.

[Schaper et al., 2004] Schaper, A. K., Hou, H., Greiner, A., and Phillipp, F. (2004). The role of iron carbide in multiwalled carbon nanotube growth. *Journal of Catalysis*, 222(1):250–254.

[Scherrer, 1918] Scherrer, P. (1918). Bestimmung der grösse und der inneren struktur vonkol-loidteilchen mittels röntgenstrahlen. *Nachrichten von der Königl Gesellschaft der Wissenschaften zu Göttingen*, 26:98–100.

[Schreiber et al., 2010] Schreiber, H. A., Prechl, J., Jiang, H., Zozulya, A., Fabry, Z., Denes, F., and Sandor, M. (2010). Using carbon magnetic nanoparticles to target, track, and manipulate dendritic cells. *Journal of Immunological Methods*, 356(1–2):47–59.

[Schwan et al., 1996] Schwan, J., Ulrich, S., Batori, V., Ehrhardt, H., and Silva, S. R. P. (1996). Raman spectroscopy on amorphous carbon films. *Journal of Applied Physics*, 80(1):440–447.

[Scott et al., 1995] Scott, J., Majetich, S., Pyrzynska, K., Huczko, A., and Lange, H. (1995). Morphology, structure, and growth of nanoparticles produced in a carbon arc. *Physical Review B*, 52(17):564–571.

[Scrivens and Tour, 1992] Scrivens, W. and Tour, J. (1992). Synthesis of gram quantities of c–60 by plasma discharge in a modified round–bottomed flask – key parameters for yield optimization and purification. *Journal of Organic Chemistry*, 57:6932–6936.

[Sen et al., 1997] Sen, R., Govindaraj, A., and Rao, C. (1997). Carbon nanotubes by the metal-locene route. *Chemical Physics Letters*, 296(3–4):276–280.

[Seo et al., 2006a] Seo, W., Lee, J., Sun, X., Suzuk, Y., Suzuki, Y., Mann, D., Liu, Z., Terashima, M., Yand, P., McConnell, M., Nishimura, D. G., and Dai, H. (2006a). Feco/graphitic–shell nanocrystals as advanced magnetic–resonance–imaging and near–infrared agents. *Nature materials*, 5(12):971–976.

[Seo et al., 2006b] Seo, W., Lee, J. H., Sun, X., Suzuki, Y., Mann, D., Liu, Z., Terashima, M., Yang, P., McConnell, M., Nishimura, D., and Dai, H. (2006b). Feco/graphitic–shell nanocrystals as advanced magnetic–resonance–imaging and near–infrared agents. *Nature Materials*, 5:971–976.

[Seon and Munz, 2000] Seon, H. and Munz, R. (2000). Study of arc stability and erosion behaviour of a transferred arc with graphite dc electrodes. *The Canadian Journal of Chemical Engineering*, 79(4):626–632.

[Seraphin et al., 1996] Seraphin, S., Zhou, D., and Jiao, D. (1996). Filling the carbon nanocages. *Journal of Applied Physics*, 80(4):2097–2104.

[Sheng et al., 2010] Sheng, J., Welzel, U., and Mittemeijer, E. J. (2010). Nonmonotonic crystallite-size dependence of the lattice parameter of nanocrystalline nickel. *Applied Physics Letters*, 97(15):153109.

[Shibuta et al., 2009] Shibuta, Y., Watanabe, Y., and Suzuki, T. (2009). Growth and melting of nanoparticles in liquid iron: A molecular dynamics study. *Chemical Physics Letters*, 475(4-6):264–268.

[Shigeta and Murphy, 2011] Shigeta, M. and Murphy, A. B. (2011). Thermal plasmas for nanofabrication. *Journal of Physics D: Applied Physics*, 44(17):174025.

[Shimada et al., 2005] Shimada, T., Sugai, T., Fantini, C., Souza, M., Cançado, L., Jorio, A., Pimenta, M., Saito, R., Grüneis, A., Dresselhaus, G., Dresselhaus, M., Ohno, Y., Mizutani, T., and Shinohara, H. (2005). Origin of the 245 cm^{-1} raman bands in hopg, single-wall and double-wall carbon nanotubes. *Carbon*, 43(5):1049–1054.

[Simchi et al., 2007] Simchi, A., Ahmadi, R., Reihani, S. S., and Mahdavi, A. (2007). Kinetics and mechanisms of nanoparticle formation and growth in vapor phase condensation process. *Materials & Design*, 28(3):850–856.

[Snyder et al., 1993] Snyder, S. C., Lassahn, G. D., and Reynolds, L. D. (1993). Direct evidence of departure from local thermodynamic equilibrium in a free-burning arc-discharge plasma. *Physical Review E*, 48:4124–4127.

[Society, 2001] Society, E. (2001). *Quantum Confinement VI: Nanostructured Materials and Devices : Proceedings of the International Symposium*. Proceedings (Electrochemical Society). Electrochemical Society.

[Star et al., 2006] Star, A., Joshi, V., Skarupo, S., Thomas, D., and Gabriel, J.-C. P. (2006). Gas sensor array based on metal-decorated carbon nanotubes. *The Journal of Physical Chemistry B*, 110(42):21014–21020.

[Stokes et al., 1904] Stokes, G., Larmor, J., and Rayleigh, J. (1904). *Mathematical and physical papers*, volume 4 of *Mathematical and Physical Papers*. University Press.

[Stoneham, 1977] Stoneham, A. M. (1977). Measurement of surface tension by lattice parameter changes: theory for faceted microcrystals. *Journal of Physics C: Solid State Physics*, 10(8):1175.

[Stoner and Wohlfarth, 1948] Stoner, E. and Wohlfarth, E. (1948). A mechanism of magnetic hysteresis in heterogeneous alloys. *Philosophical Transactions of the Royal Society of London. Series A.*, 240(599).

[Sun and Simon, 2007] Sun, J. and Simon, S. (2007). The melting behavior of aluminum nanoparticles. *Thermochimica Acta*, 463(1-2):32–40.

[Sun et al., 2006] Sun, Z., Wang, L., Liu, P., Wang, S., Sun, B., Jiang, D., and Xiao, F. (2006). Magnetically motive porous sphere composite and its excellent properties for the removal of pollutants in water by adsorption and desorption cycles. *Advanced Materials*, 18(15):1968–1971.

[Sung and Tai, 1997] Sung, C.-M. and Tai, M.-F. (1997). Reactivities of transition metals with carbon: Implications to the mechanism of diamond synthesis under high pressure. *International Journal of Refractory Metals and Hard Materials*, 15(4):237–256.

[Szczytko et al., 2007] Szczytko, J., Osewski, P., Bystrzejewski, M., Borysiuk, J., Grabias, A., Huczko, A., Lange, H., Majhofer, A., and Twardowski, A. (2007). Carbon–encapsulated magnetic nanoparticles based on fe, mn, and cr for spintronics applications. *Acta Physics Polonica A*, 112:305–310.

[Tartaj et al., 2003] Tartaj, P., del Puerto Morales, M., Veintemillas-Verdaguer, S., González-Carreño, T., and Serra, C. (2003). The preparation of magnetic nanoparticles for applications in biomedicine. *Journal of Physics D: Applied Physics*, 36(13):R182–R197.

[Tashiro et al., 2010] Tashiro, S., Zeniya, T., Yamamoto, K., Tanaka, M., Nakata, K., Murphy, A. B., Yamamoto, E., Yamazaki, K., and Suzuki, K. (2010). Numerical analysis of fume formation mechanism in arc welding. *Journal of Physics D: Applied Physics*, 43(43):434012.

[Taylor et al., 2010] Taylor, A., Krupskaya, Y., Krämer, K., Füssel, S., Klingeler, R., Büchner, B., and Wirth, M. (2010). Cisplatin–loaded carbon–encapsulated iron nanoparticles and their in vitro effects in magnetic fluid hyperthermia. *Carbon*, 48(8):2327–2334.

[Teng et al., 1995] Teng, M., Host, J., Hwang, J., Elliott, B., Weertman, J., Mason, T., Dravid, V. P., and Johnson, D. L. (1995). Nanophase ni particles produced by a blown arc method. *Journal of Materials Research*, 10(2):233–236.

[Tersoff et al., 1996] Tersoff, J., Teichert, C., and Lagally, M. G. (1996). Self–organization in growth of quantum dot superlattices. *Physical Review Letters*, 76:1675–1678.

[Tsai et al., 2005] Tsai, C. C., Gabriel, T. A., Haines, J. R., and Rasmussen, D. A. (2005). Graphite sublimation tests for target development for the muon collider/neutrino factory.

[Tscharnuter, 2000] Tscharnuter, W. (2000). Mobility measurements by phase analysis. In *Photon Correlation and Scattering*, page MA3. Optical Society of America.

[Tscharnuter, 2006] Tscharnuter, W. (2006). Photon correlation spectroscopy in particle sizing. In *Encyclopedia of Analytical Chemistry*. John Wiley & Sons, Ltd.

[Ushio, 1988] Ushio, M. (1988). Arc discharge and electrode phenomena. *Pure & Applied Chemistry*, 60(5):809–814.

[Vaisman et al., 2006] Vaisman, L., Wagner, H. D., and Marom, G. (2006). The role of surfactants in dispersion of carbon nanotubes. *Advances in Colloid and Interface Science*, 128-130:37–46.

[Vargas et al., 2005] Vargas, J., Nunes, W., Socolovsky, M., Knobel, M., and Zanchet, D. (2005). Effect of dipolar interaction observed in iron-based nanoparticles. *Physical Review B*, 72(184428):1–6.

[Vehkamäki, 2006] Vehkamäki, H. (2006). *Classical Nucleation Theory in Multicomponent Systems*. Springer.

[Verwey and Overbeek, 1999] Verwey, E. and Overbeek, J. (1999). *Theory of the Stability of Lyophobic Colloids*. Dover Books on Chemistry Series. Dover Publications.

[Verwey, 1947] Verwey, E. J. W. (1947). Theory of the stability of lyophobic colloids. *The Journal of Physical and Colloid Chemistry*, 51(3):631–636.

[Wang et al., 2007a] Wang, C., Wang, J., and Sheng, Z. (2007a). Solid-phase synthesis of carbon-encapsulated magnetic nanoparticles. *The Journal of Physical Chemistry C*, 111(17):6303–6307.

[Wang et al., 2004] Wang, F. L., Jiang, J. C., and Meletis, E. I. (2004). Microstructural evolution of co nanostructures in diamond-like carbon by plasma-assisted processing. *Journal of Applied Physics*, 95(9):5069–5074.

[Wang et al., 2012] Wang, H., Cuppens, J., Biermans, E., Bals, S., Fernandez-Ballester, L., Kvashnina, K. O., Bras, W., Bael, M. J. V., Temst, K., and Vantomme, A. (2012). Tuning of the size and the lattice parameter of ion-beam synthesized pb nanoparticles embedded in si. *Journal of Physics D: Applied Physics*, 45(3):035301.

[Wang et al., 1995] Wang, J., Li, J., Yip, S., Phillpot, S., and Wolf, D. (1995). Mechanical instabilities of homogeneous crystals. *Physical Review B*, 52:12627–12635.

[Wang et al., 2007b] Wang, J. N., Zhang, L., Yu, F., and Sheng, Z. M. (2007b). Synthesis of carbon encapsulated magnetic nanoparticles with giant coercivity by a spray pyrolysis approach. *The Journal of Physical Chemistry B*, 111(8):2119–2124.

[Wegrowe et al., 2002] Wegrowe, J., Sallin, A., Fábián, A., Comment, A., Bonard, J., and Ansermet, J. (2002). Magnetoresistance properties of granular nanowires composed of carbon nanoparticles embedded in a co matrix. *Physical Review B*, 65(1):012407:1–4.

[Wei et al., 1998] Wei, B., Zhang, J., Liang, J., and Wu, D. (1998). The mechanism of phase transformation from carbon nanotube to diamond. *Carbon*, 36(7-8):997–1001.

[Wei et al., 2007] Wei, Z., Xia, T., Ma, J., Feng, W., Dai, J., Wang, Q., and Yan, P. (2007). Investigation of the lattice expansion for ni nanoparticles. *Materials Characterization*, 58(10):1019 – 1024.

[Weissleder et al., 2010] Weissleder, R., Ross, B., Rehemtulla, A., and Gambhir, S. (2010). *Molecular Imaging: Principles and Practice*. Pmph USA Ltd Series. People's Medical Publishing House.

[Westberg et al., 1992] Westberg, H., Boman, M., Norekrans, A.-S., and Carlsson, J.-O. (1992). Carbon growth by thermal laser–assisted chemical vapour deposition. *Thin Solid Films*, 215(2):126–133.

[Widenkvist et al., 2011] Widenkvist, E., Alm, O., Boman, M., Jansson, U., and Grennberg, H. (2011). Functionalization and area–selective deposition of magnetic carbon–coated iron nanoparticles from solution. *Journal of Nanotechnology*, 2011(2):1–4.

[Wiesendanger, 1994] Wiesendanger, R. (1994). *Scanning Probe Microscopy and Spectroscopy: Methods and Applications*. Cambridge University Press.

[Williams and Carter, 1996] Williams, D. and Carter, C. (1996). *Transmission Electron Microscopy: A Textbook for Materials Science*, volume 1 of *Transmission Electron Microscopy: A Textbook for Materials Science*. Plenum Press.

[Wyckoff, 1963] Wyckoff, R. (1963). *Crystal structures*, volume 1. Interscience Publiser, New York, New York, 2nd edition.

[Xiao and Chien, 1987] Xiao, G. and Chien, C. (1987). Giant magnetic coercivity and percolation effects in granular fe–($si0_2$) solids. *Applied Physics Letters*, 51(16):289–294.

[Xing and Rosner, 1999] Xing, Y. and Rosner, D. E. (1999). Prediction of spherule size in gas phase nanoparticle synthesis. *Journal of Nanoparticle Research*, 1:277–291.

[Xiong et al., 2004] Xiong, Y., Xie, Y., Li, X., and Li, Z. (2004). Production of novel amorphous carbon nanostructures from ferrocene in low-temperature solution. *Carbon*, 42(8-9):1447–1453.

[Xu et al., 2010] Xu, Y., Mahmood, M., and Fejleh, A. (2010). Carbon–covered magnetic nanomaterials and their application for the thermolysis of cancer cells. *International Journal of Nanomedicine*, 5:167–176.

[Yang et al., 2009] Yang, G., Wang, X., Xu, Q., Wang, S., Tian, H., and Zheng, W. (2009). Two types of carbon nanocomposites: Graphite encapsulated iron nanoparticles and thin carbon nanotubes supported on thick carbon nanotubes, synthesized using pecvd. *Journal of Solid State Chemistry*, 182(4):966–972.

[Yang, 2007] Yang, G. W. (2007). Laser ablation in liquids: Applications in the synthesis of nanocrystals. *ChemInform*, 38(38):648–698.

[Yang et al., 2003] Yang, W.-C., Zeman, M., Ade, H., and Nemanich, R. J. (2003). Attractive migration and coalescence: A significant process in the coarsening of tisi$_2$ islands on the si(111) surface. *Physical Review Letters*, 90:136102.

[Zeltner et al., 2012] Zeltner, M., Grass, R. N., Schaetz, A., Bubenhofer, S. B., Luechinger, N. A., and Stark, W. J. (2012). Stable dispersions of ferromagnetic carbon–coated metal nanoparticles: preparation via surface initiated atom transfer radical polymerization. *Journal of Materials Chemistry*, 22:12064–12071.

[Zeng et al., 2012] Zeng, H., Du, X.-W., Singh, S. C., Kulinich, S. A., Yang, S., He, J., and Cai, W. (2012). Nanomaterials via laser ablation/irradiation in liquid: A review. *Advanced Functional Materials*, 22(7):1333–1353.

[Zhang et al., 2010] Zhang, D., Wei, S., Kaila, C., Su, X., Wu, J., Karki, A. B., Young, D. P., and Guo, Z. (2010). Carbon–stabilized iron nanoparticles for environmental remediation. *Nanoscale*, 2:917–919.

[Zhang and Sham, 2002] Zhang, P. and Sham, T. K. (2002). Tuning the electronic behavior of au nanoparticles with capping molecules. *Applied Physics Letters*, 81(4):736–738.

[Zhou et al., 2009] Zhou, S., Berndt, M., Buerger, D., Heera, V., Potzger, K., Abrasonis, G., Radnoczi, G., Kovacs, G. J., Kolitsch, A., Helm, M., Fassbender, J., Moeller, W., and Schmidt, H. (2009). Spin–dependent transport in nanocomposite c:co films. *Acta Materialia*, 57(16):4758–4764.

[Zhu et al., 2007] Zhu, L. Y., Lu, G. H., Mao, S., Chen, J. H., Dikin, D. A., Chen, X. Q., and Ruoff, R. S. (2007). Ripening of silver nanoparticles on carbon nanotubes. *NANO*, 2(3):149–156.

Appendix

A.1 F–Distribution and ANOVA

Many statistical applications involve the comparison of more than two groups, such as social science, psychology, education. Statisticians have developed a method named *Analysis of Variance* (ANOVA) in order to determine the existence of a statistically significant difference among several group averages.

Several basic considerations are assumed in ANOVA tests: each population present a normal distribution, each sample is randomly selected and independent and finally, standard deviations are assumed to be the same for each population.

The null hypothesis is considered that all the group population have the same mean. In our experiments, we used the ANOVA test to verify the null hypothesis in the Plackett–Burman experiments (chapter 4). There is also the alternative hypothesis.

The ANOVA summary table consists of several columns [Lane, 2006]. The first column contains the source of variation. In our case we varied 6 sources (pressure, arc current, amount of Fe, He flow, cathode diameter and flow geometry). The second column contains the sum of squares. The sum of squares is the sum between the sum of squares groups (SSB) and the sum of squares error (SSE). The SSB is calculated as follows $SSB = \sum n_i \left(M_i - GM \right)^2$, where n_i is the sample size of the ith group and M_i is the mean of the ith group and GM is the mean of all scores in all groups. The SSE is the sum of the squared differences between the individual scores and their group means. In our case, the SSB agrees with the sum of squares. The third column contains the degree of freedom (df). The df for groups is always equal to the number of groups minus one. In our case, we studied two groups (positive level and negative level), therefore, $df_{\text{groups}} = 1$. The df for error is equal to the number of subjects minus one, $df_{\text{error}} = 5$ and the df for total is equal to the number of experiments minus one, $df_{\text{total}} = 11$. The fourth column contains the mean squares which are calculated by dividing the sum of squares by the

degrees of freedom for groups. In our case, the sum of squares agrees with the mean square ($df_{\text{group}} = 1$). The fifth column contains the F–ratio. The distribution used for the hypothesis test is the F-distribution or Fisher–Snedecor distribution (F–ratio).

The F–ratio is obtained by dividing the mean square for groups by the mean square for error. There is no F–ratio for error or total. The last column gives the probability value (p–value), which gives the significance level of the test, that is to say, the probability of obtaining an F as large than the one obtained in the the data assuming that the null hypothesis is true. It can be calculated from a F–table. The df for groups (1) is used as the degrees of freedom in the numerator and df for error (5) is used as the degrees of freedom in the denominator [Oehlert, 2000].

In Table A.1, critical values of F–ratio at the $p = 0.05$ level of significance are shown, where (x,y) are the degrees of freedom associated with it. In our case (x,y)=(1,5), in order to obtain a significance level of p=0.05, the F–ratio should be larger than 6.61.

Figure A.1: Critical Values of F-distribution at $p = 0.05$ printed from [Oehlert, 2000].

Table entries are $F_{.05,\nu_1,\nu_2}$ where $P_{\nu_1,\nu_2}(F > F_{.05,\nu_1,\nu_2}) = .05$.

ν_2	1	2	3	4	5	6	7	8	9	10	12	15	20	25	30	40
1	161	200	216	225	230	234	237	239	241	242	244	246	248	249	250	251
2	18.5	19.0	19.2	19.2	19.3	19.3	19.4	19.4	19.4	19.4	19.4	19.4	19.4	19.5	19.5	19.5
3	10.1	9.55	9.28	9.12	9.01	8.94	8.89	8.85	8.81	8.79	8.74	8.70	8.66	8.63	8.62	8.59
4	7.71	6.94	6.59	6.39	6.26	6.16	6.09	6.04	6.00	5.96	5.91	5.86	5.80	5.77	5.75	5.72
5	6.61	5.79	5.41	5.19	5.05	4.95	4.88	4.82	4.77	4.74	4.68	4.62	4.56	4.52	4.50	4.46
6	5.99	5.14	4.76	4.53	4.39	4.28	4.21	4.15	4.10	4.06	4.00	3.94	3.87	3.83	3.81	3.77
7	5.59	4.74	4.35	4.12	3.97	3.87	3.79	3.73	3.68	3.64	3.57	3.51	3.44	3.40	3.38	3.34
8	5.32	4.46	4.07	3.84	3.69	3.58	3.50	3.44	3.39	3.35	3.28	3.22	3.15	3.11	3.08	3.04
9	5.12	4.26	3.86	3.63	3.48	3.37	3.29	3.23	3.18	3.14	3.07	3.01	2.94	2.89	2.86	2.83
10	4.96	4.10	3.71	3.48	3.33	3.22	3.14	3.07	3.02	2.98	2.91	2.85	2.77	2.73	2.70	2.66
11	4.84	3.98	3.59	3.36	3.20	3.09	3.01	2.95	2.90	2.85	2.79	2.72	2.65	2.60	2.57	2.53
12	4.75	3.89	3.49	3.26	3.11	3.00	2.91	2.85	2.80	2.75	2.69	2.62	2.54	2.50	2.47	2.43
13	4.67	3.81	3.41	3.18	3.03	2.92	2.83	2.77	2.71	2.67	2.60	2.53	2.46	2.41	2.38	2.34
14	4.60	3.74	3.34	3.11	2.96	2.85	2.76	2.70	2.65	2.60	2.53	2.46	2.39	2.34	2.31	2.27
15	4.54	3.68	3.29	3.06	2.90	2.79	2.71	2.64	2.59	2.54	2.48	2.40	2.33	2.28	2.25	2.20
16	4.49	3.63	3.24	3.01	2.85	2.74	2.66	2.59	2.54	2.49	2.42	2.35	2.28	2.23	2.19	2.15
17	4.45	3.59	3.20	2.96	2.81	2.70	2.61	2.55	2.49	2.45	2.38	2.31	2.23	2.18	2.15	2.10
18	4.41	3.55	3.16	2.93	2.77	2.66	2.58	2.51	2.46	2.41	2.34	2.27	2.19	2.14	2.11	2.06
19	4.38	3.52	3.13	2.90	2.74	2.63	2.54	2.48	2.42	2.38	2.31	2.23	2.16	2.11	2.07	2.03
20	4.35	3.49	3.10	2.87	2.71	2.60	2.51	2.45	2.39	2.35	2.28	2.20	2.12	2.07	2.04	1.99
21	4.32	3.47	3.07	2.84	2.68	2.57	2.49	2.42	2.37	2.32	2.25	2.18	2.10	2.05	2.01	1.96
22	4.30	3.44	3.05	2.82	2.66	2.55	2.46	2.40	2.34	2.30	2.23	2.15	2.07	2.02	1.98	1.94
23	4.28	3.42	3.03	2.80	2.64	2.53	2.44	2.37	2.32	2.27	2.20	2.13	2.05	2.00	1.96	1.91
24	4.26	3.40	3.01	2.78	2.62	2.51	2.42	2.36	2.30	2.25	2.18	2.11	2.03	1.97	1.94	1.89
25	4.24	3.39	2.99	2.76	2.60	2.49	2.40	2.34	2.28	2.24	2.16	2.09	2.01	1.96	1.92	1.87
30	4.17	3.32	2.92	2.69	2.53	2.42	2.33	2.27	2.21	2.16	2.09	2.01	1.93	1.88	1.84	1.79
40	4.08	3.23	2.84	2.61	2.45	2.34	2.25	2.18	2.12	2.08	2.00	1.92	1.84	1.78	1.74	1.69
50	4.03	3.18	2.79	2.56	2.40	2.29	2.20	2.13	2.07	2.03	1.95	1.87	1.78	1.73	1.69	1.63
75	3.97	3.12	2.73	2.49	2.34	2.22	2.13	2.06	2.01	1.96	1.88	1.80	1.71	1.65	1.61	1.55
100	3.94	3.09	2.70	2.46	2.31	2.19	2.10	2.03	1.97	1.93	1.85	1.77	1.68	1.62	1.57	1.52
200	3.89	3.04	2.65	2.42	2.26	2.14	2.06	1.98	1.93	1.88	1.80	1.72	1.62	1.56	1.52	1.46
∞	3.84	3.00	2.61	2.37	2.21	2.10	2.01	1.94	1.88	1.83	1.75	1.67	1.57	1.51	1.46	1.40

A.2   Magnetic Units

In this section we present a table to convert magnetic units (Table A.1) with some related notes.

a. Gaussian units and cgs emu are the same for magnetic properties. The defining relation is $B = H + 4\pi M$.

b. Multiply a number in Gaussian units by C to convert it to SI.

c. SI (*Système International d'Unitès*) has been adopted by the National Bureau of Standards. Where to conversion factors are given, the upper one is recognized under, or consistent with, SI and is based on the definition $B = \mu_0(H + M)$, where $\mu_0 = 4\pi \cdot 10^{-7}$ H/m. The lower one is not recognized under SI and is based on the definition $B = \mu_0 H + J$, where the symbol I is often used in place of J.

d. 1 gauss $= 10^5$ gamma (γ).

e. Both oersted and gauss are expressed as $\text{cm}^{1/2}\text{g}^{1/2}\text{s}^{-1}$ in terms of base units.

f. A/m was often expressed as ampere–turn per meter when used for magnetic field strength.

g. Magnetic moment per unit volume.

h. The designation emu is not a unit.

i. Recognised under SI, even though based on the definition $B = \mu_0 H + J$. See note c.

j. $\mu_r = \mu/\mu_0 = 1 + \chi$, all in SI. μ_r is equal to Gaussian μ.

k. BH and $\mu_0 MH$ have SI units J/m^3; MH and $BH/4\pi$ have Gaussian units erg/cm^3.

This information was taken from [Goldfarb and Fickett, 1985].

Table A.1: Units for magnetic properties [Goldfarb and Fickett, 1985].

Quantity	Symbol	Gaussian & cgs emu[a]	Conversion, C[b] Factor	SI[c]
Magnetic flux density, magnetic induction	B	gauss (G)[d]	10^{-4}	testla (T), Wb/cm²
Magnetic flux	Φ	maxwell (Mx), G·cm²	10^{-8}	weber (Wb), volt second (V·s)
Magnetic potential difference, magnetomotive force	U, F	gilbert (Gb)	$10^4/4\pi$	A/m[f]
Magnetic field strength, magnetising force	H	oersted (Oe)[e], Gb/cm	$10^3/4\pi$	A/m[f]
(Volume) magnetisation[g]	M	emu/cm³ [h]	10^3	A/m
(Volume) magnetisation	$4\pi M$	G	$10^3/4\pi$	A/m
Magnetic polarisation, intensity of magnetisation	J, I	emu/cm³	$4\pi \cdot 10^{-4}$	T, Wb/m² [i]
(Mass) magnetisation	σ, M	emu/g	1	Am²/kg
Magnetic moment	m	emu, erg/G	10^{-3}	Am², joule per tesla (J/T)
Magnetic dipole moment	j	emu, erg/G	$4\pi10^{-10}$	Wbm [i]
(Volume) susceptibility	χ, κ	dimensionless, emu/cm³	4π / $(4\pi)^2 \cdot 10^{-10}$	dimensionless / henry per meter (H/m), Wb/(Am)
(Mass) susceptibility	$x_m, \kappa_m o l$	cm³/mol, emu/mol	$4\pi10^{-6}$ / $(4\pi)^2 \cdot 10^{-13}$	m³/mol / Hm²/mol
Permeability	μ	dimensionless	$4\pi \cdot 10^{-7}$	H/m, Wb/(Am)
Relative permeability[j]	μ_r	not defined	–	dimensionless
(Volume) energy density, energy product[k]	W	erg/cm³	10^{-1}	J/m³
Demagnetisation factor	D, N	dimensionless	$1/(4\pi)$	dimensionless

A.3 List of nanoparticle samples

Table A.2: Samples corresponding to Plackett–Burman experiments and other experiments produced by the **conventional arc–discharge plasma (ADP)** reactor.

#	SAMPLE	GAS	PRESSURE [± 1 mbar]	FLOW GEOMETRY	FLOW RATE [±0.1 l/min]	Fe AMOUNT [±0.1 mg]	ARC CURRENT [A]	ANODE DIAMETER [nm]
1	27K08	He	200	circular–flow	0.8	180.0	55	7
2	02L08	He	200	coaxial–flow	1.8	54.9	55	0.9
3	09C09	He	500	circular–flow	1.8	180.0	5	7
	04L08	He	500	circular–flow	1.8	180.0	5	7
4	05L08	He	200	coaxial–flow	1.8	180.0	5	0.9
	11L08	He	200	coaxial–flow	1.8	180.0	5	0.9
5	12L08	He	500	coaxial–flow	0.8	54.9	55	0.9
6	14A09	He	200	circular–flow	0.8	54.9	5	7
7	15A09	He	500	coaxial–flow	1.8	54.9	5	7
8	02B09	He	200	coaxial–flow	0.8	180.0	5	0.9
	03B09	He	200	coaxial–flow	0.8	180.0	5	0.9
9	05B09	He	500	circular–flow	0.8	180.0	55	7
10	09B09	He	500	coaxial–flow	0.8	54.9	5	0.9
11	11B09	He	200	circular–flow	1.8	54.9	55	7
12	23B09	He	500	circular–flow	1.8	180.0	55	0.9
Other	11A08	He	500	coaxial–flow	3.3	180.0	25	7
	29D08	He	300	circular–flow	5.2	72.5	25	7
	01E08	He	300	circular–flow	5.2	272.0	25	7
	16G08	He	200	circular–flow	1.8	253.2	70	7
	21G08	He	200	coaxial–flow	1.8	253.2	70	7
	09J08	He	200	circular–flow	1.8	181.3	55	7
	16J08	He	500	coaxial–flow	0.8	181.3	5	7
	17J08	He	500	circular–flow	0.8	54.9	55	7
	21J08	Ar	200	coaxial–flow	1.8	54.9	5	7
	22J08	Ar	200	circular–flow	0.8	54.9	5	7
	28J08	He	500	coaxial–flow	0.8	181.3	5	7

Table A.3: Samples from the group A and B produced by the **modified arc–dicharge plasma (mADP)** reactor.

#	Sample	Gas	Arc Current [A]	Flow Rate [±0.1 l/min]	Fe Precursor (w/w) [wt.%]	Injection Velocity [±0.01 l/min]
	28D10	He	15	1.6	0.5	1.00
*A*1	24K10	He	15	1.6	0.5	1.00
	17B11	He	15	1.6	0.5	1.00
	17C11	He	15	1.6	0.5	1.00
	30G10	He	20	1.6	0.5	1.00
*A*2	08C11	He	20	1.6	0.5	1.00
	18J11	He	20	1.6	0.5	1.00
	22I09	He	25	1.6	0.5	1.00
*A*3 & *C*2	12D10	He	25	1.6	0.5	1.00
	22K10	He	25	1.6	0.5	1.00
	25A11	He	25	1.6	0.5	1.00
	29G10	He	30	1.6	0.5	1.00
*A*4	22B11	He	30	1.6	0.5	1.00
	22C11	He	30	1.6	0.5	1.00
	27D10	He	40	1.6	0.5	1.00
*A*5	23K10	He	40	1.6	0.5	1.00
	10C11	He	40	1.6	0.5	1.00
*B*1	08B10a	He	15	6.8	0.5	1.00
	12A10	He	25	6.8	0.5	1.00
*B*2 & *D*2	23I09a	He	25	6.8	0.5	1.00
	04B10	He	25	6.8	0.5	1.00
	12B10	He	25	6.8	0.5	1.00
*B*3	08B10b	He	40	6.8	0.5	1.00
*B*4	08B10a	He	15	6.8	0.5	1.00

Table A.4: Samples from the group C and D (increasing ferrocene content at low and high He flow rate) and other experiments produced by the **mADP** reactor.

#	SAMPLE	GAS	ARC CURRENT [A]	FLOW RATE [±0.1 l/min]	Fe PRECURSOR (w/w) [wt.%]	INJECTION VELOCITY [±0.01 l/min]
C1	01C11	He	25	1.6	0.87	1.00
	17H09	He	25	1.6	1.75	1.00
C3	18H09	He	25	1.6	1.75	1.00
	28G10	He	25	1.6	1.75	1.00
	25C11	He	25	1.6	1.75	1.00
C4	14I09	He	25	1.6	2.63	1.00
	29D11	He	25	1.6	2.63	1.00
C5	06E11	He	25	1.6	3	1.00
D1	23I09b	He	25	6.8	0.87	1.00
D3	25I09	He	25	6.8	1.75	1.00
	07J09	He	25	6.8	1.75	1.00
D4	29I09	He	25	6.8	2.63	1.00
	18A10	He	25	6.8	2.63	1.00
D5	01J09	He	25	6.8	3	1.00
Other	26F09	He	15	1.6	1.75	1.00
	30F09	He	15	1.6	1.75	1.00
	14G09	He	75	1.6	1.75	1.00
	19H09	He	40	1.6	1.75	1.00
	20H09	He	55	1.6	1.75	1.00
	21I09	He	40	1.6	1.75	1.00
	13A10	He	25	6.8	0.5	1.50
	19A10a	He	25	6.8	0.5	2.00
	19A10b	He	75	6.8	1.75	1.00
	20A10	He	40	6.8	1.75	1.00

B Scientific Contributions

Publications and Communications

This section contains information about the scientific contributions of the author derived from this thesis.

Journal Publications

- AGUILÓ-AGUAYO, N.; García-Céspedes, J.; Pascual, E.; Bertran, E. **Magnetic properties of iron-filled multiwalled carbon nanotubes** Technical Proceedings of the 2008 NSTI Technology Conference and Trade Show Nanotech 2008, Nanotechnology 2008; Materials, Fabrication, Particles and Characterization (2008).

- AGUILÓ-AGUAYO, N.; Castaño-Bernal, J.L.; García-Céspedes, J.; Bertran, E. **Magnetic response of CVD and PECVD iron filled multiwalled carbon nanotubes**, Diamond and Related Materials , 18 (2009); 953–56.

- AGUILÓ-AGUAYO, N.; Inestrosa-Izurieta, M.J.; García-Céspedes, J.; Bertran, E., **Morphological and magnetic properties of superparamagnetic carbon-coated Fe nanoparticles produced by arc discharge**, Journal of Nanoscience and Nanotechnology, 10 (2010); 4:2646–49.

- AGUILÓ-AGUAYO, N.; Liu, Z.; Yang, J.C.; Bertran, E., **In-situ TEM observation of thermally induced structural evolution of carbon-encapsulated iron nanoparticles**, The Journal of Physical Chemistry (*Accepted*).

- AGUILÓ-AGUAYO, N.; Maurizi, M.G.; Ollivier Beuzelin M.G.; Coullerez, G.; Bertran, E.; Hofmann, H. **Stabilisation in aqueous solution of carbon-encapsulated superparamagnetic nanoparticles for several applications**, Nanoscale (*Submitted*).

- AGUILÓ-AGUAYO, N.; Bertran, E., **Controlled growth of carbon–encapsulated super-paramagnetic Fe nanoparticles obtained by a modified arc-discharge plasma method**, Carbon (*Manuscript*).

- AGUILÓ-AGUAYO, N.; Bertran, E., **Size-dependent magnetic properties of carbon–encapsulated superparamagnetic Fe nanoparticles**, Applied Physics Letters (*Manuscript*).

Patents

- Bertran, E.; AGUILÓ-AGUAYO, N.; Inestrosa-Izurieta, M.J., **Method and reactor for the production of carbon–encapsulated nanoparticles**. Application Number: ES31171 Spain (2010).

Conference contributions

- AGUILÓ-AGUAYO, N.; García-Céspedes, J.; Pascual, E.; Bertran, E., **Magnetic properties of iron–filled multiwalled carbon nanotubes**, POSTER, NSTI Nanotech 2008, The nanotechnology Conference and Trade Show, Boston MA (United States), 2008.

- AGUILÓ-AGUAYO, N.; Inestrosa-Izurieta, M.J.; García- Céspedes, J. Bertran, E., **Morphological and magnetic properties of superparamagnetic carbon-coated Fe nanoparticles produced by arc discharge**, ORAL COMMUNICATION, 2nd International Conference on Advanced Nano Materials "ANM 2008", Aveiro (Portugal), 2008.

- AGUILÓ-AGUAYO, N.; Castaño-Bernal, J.L.; García- Céspedes, J.; Bertran, E., **Enhanced magnetic response of iron filled multi–walled carbon nanotubes**, POSTER, 19th European conference on diamond, diamond-like materials, carbon nanotubes, and Nitrides. "DIAMOND 2008", Sitges (Spain), 2008.

- AGUILÓ-AGUAYO, N.; Castaño-Bernal, J.L.; Jover, E.; Bertran, E., **Optimization of the experimental parameters of an improved CVD reactor to control carbon nanotubes deposition characteristics**, ORAL COMMUNICATION, 1st IRUN Symposium on Nanotechnology, Münster (Germany), 2008.

- Bertran, E.; García- Céspedes, J.; Castaño, J.L.; Rubio–Roy, M.; AGUILÓ-AGUAYO,N.; Jover,E.; Pascual,E.; delCampo, F.J.; Muñoz, F.X., **Carbon nanotube based electrodes for energy applications**, INVITED CONFERENCE, 3rd International Conference on Surfaces, Coatings and Nanostructured Materials "NANOSMAT 2008", Barcelona (Spain), 2008.

- AGUILÓ-AGUAYO, N.; Jover, E.; Bertran, E., **Statistics–based experimental design to study the formation of carbon–coated magnetic nanoparticles by plasma arc**, POSTER,

10th Trends in Nanotechnology International Conference "TNT 2009", Barcelona (Spain), 2009.

- AGUILÓ-AGUAYO, N.; Inestrosa-Izurieta, M.J.; Bertran E., **Synthesis and superparamagnetic characterization of isolated carbon-coated iron oxide nanoparticles obtained by plasma arc.**, INVITED CONFERENCE, The Seventeeth Annual International Conference on Composites/Nano Engineerging "ICCE-17", Honolulu (United States), 2009.

- Liu, Z.; AGUILÓ-AGUAYO, N.; Sturgeon, J.L.; Bunker, K.L.; Bertran, E.; Yang, J. C., **Release and mobility of iron nanocrystals encapsulated in carbon shells by in-situ STEM/HRTEM observation**, ORAL COMMUNICATION, 2010 Materials Research Society Fall Symposium SS: Advanced Imaging and Scattering Techniques for In-situ Studies, "2010 MRS Fall Meeting", Boston (United States), 2010.

- Liu, Z.; AGUILÓ-AGUAYO, N.; Bertran, E.; Yang, J.C., **Structural stability and release behaviour of iron nanocrystals encapsulated in carbon shell by in-situ TEM/HRTEM observation**, ORAL COMMUNICATION, Microscopy & Microanalysis 2010 Meeting, "M&M2010", Portland (United States), 2010.

- AGUILÓ-AGUAYO, N.; Bertran, E., **Determination of anisotropy and blocking temperatures of carbon-encapsulated superparamagnetic nanoparticles**, ORAL COMMUNICATION, 5th International Conference on Surfaces, Coatings and Nanostructured Materials, "NANOSMAT2010", Reims (France), 2010.

- AGUILÓ-AGUAYO, N.; Bertran, E., **Superparamagnetic behaviour at low temperatures of carbon-encapsulated iron nanoparticles** POSTER, 7th International Conference on Inorganic Materials, Inorganic Materials Conference 2010, Biarritz (France), 2010.

- AGUILÓ-AGUAYO, N.; Bertran, E., **Correlation between applied current and carbon crystallinity in Fe@C nanoparticles obtained by plasma arc**, POSTER, 11th edition of the Trends in Nanotechnology International Conference, "TNT2010", Braga (Portugal), 2010.

- AGUILÓ-AGUAYO, N.; Bertran, E., **Carbon sealed monodispersed iron nanoparticles ($<$ 10 nm) with low superparamagnetic blocking temperature (up to 25K)**, POSTER, E-MRS ICAM IUMRS 2011 Spring Meeting, Nice (France), 2011.

- Sanaee, M. R.; Chaitoglou, S.; AGUILÓ-AGUAYO, N.; Bertran, E., **Influences of argon-helium mixtures on the carbon- coated iron nanoparticles produced by a modified arc dis- charge**, ORAL COMMUNICATION, 9th International Conference on Nanoscience & Nanotechnologies "NN12", Thessaloniki (Greece), 2012.

Resum en català

El segle XXI s'ha convertit en l'era de la nanociència i la nanotecnologia. El descobriment de noves propietats relacionades amb l'escala de mida nanomètrica ha fet que investigadors d'arreu del món es centréssin en el desenvolupament de nous nanomaterials amb característiques úniques, amb aplicacions revolucionàries. Tot això succeeix en un context on el mercat de la tecnologia es mou cap a dispositius més petits amb més capacitat i multi–funcionalitat. No obstant això, aquest sector no és l'únic beneficiari d'aquesta nova era, el descobriment d'estructures de mida nanomètrica ha possibilitat l'apropament a món biològic obrint noves vies per combatre malalties com el càncer, la malària o malalties degeneratives.

El 1959, el físic Richard P. Feyman, conegut com el pare de la nanotecnologia, va presentar a la reunió anual de la Societat America de Física al *California Institute of Technology (Caltech)* una xerrada amb títol *There's Plenty of Room at the Bottom* on es preveia la importància de la petita escala i l'enorme potencial d'aquest nou camp. El 1985, investigadors de la *Rice University*, van descobrir una nova forma al·lotròpica del carboni, els anomenats ful·lerens. Aquesta nova estructura similar al grafit, però amb figura geomètrica truncada semblant a una pilot de futbol, presenta noves propietats en comparació amb les ja conegudes pel carboni. Aquest va ser el primer pas cap a un nou camp de la nanociència relacionat amb el desenvolupament i l'estudi de diverses nanoestructures basades en carboni, com els nanotubs de carboni de grafè, individuals, dobles i paret múltiple (SWCNT, DWCNT, MWCNT), nanotubs de carboni, o les nanopartícules magnètiques recobertes de carboni. Aquestes nanomaterials presenten noves propietats físiques i químiques que cobreixen aplicacions en diversos camps de la biomedicia, l'electrònica, el medi ambient o l'automoció.

Les nanopartícules magnètiques de ferro recobertes de carboni s'estan investigant en gran mesura, ja que presenten avantatjoses propietats sobre d'altres recobriments protectors del nucli magnètic com els polímers o la sílice. El recobriment de carboni protegeix el nucli de ferro de l'oxidació, la degració química i tèrmica, d'aquesta manera els nuclis presenten propietats magnètiques estables quan les nanopartícules s'exhibeixen en aire o en un altre

medi. S'han realitzat diversos estudis sobre aquest tipus de nanopartícules, però aquest tipus de nanopartícules s'obtenen amb gran dispersió de grandàries i poca uniformitat en les seves característiques. És encara un repte en aquest camp la producció de nanopartícules de ferro recobertes de carbon amb propietats morfològiques i estructurals, així com l'estudi sistemàtic de les seves propietats magnètiques. Per aquest motiu, l'objectiu d'aquesta tesi es centra en la producció i caracterització de nanopartícules superparamagnètiques de ferro recobertes de carboni amb estreta distribució de mides i amb propietats magnètiques ben caracteritzades per diverses aplicacions, en particular, les relacionades amb el camp de la biomedicina. No obstant això, l'estudi sistemàtic d'aquestes aplicacions es troba fora del marc d'aquesta tesi.

El contingut s'estructura en quatre parts:

- La primera part d'introducció conté els aspectes bàsics sobre aquest tipus de nanopartícules, així com les propietats derivades de la seva mida nanomètrica, les tecnologies que s'utilitzen per generar aquest tipus de nanopartícules, una explicació sobre els possibles mecanismes responsables de la seva formació i les principals aplicacions d'aquestes nanopartícules.

- La segona part descriu les tècniques utilitzades per la caracterització d'aquestes nanopartícules que engloben tècniques de microscopia, de difracció de raigs-X, d'espectroscòpia Raman, per la caracterització col·loidal de les nanopartícules fins la seva caracterització magnètica. També inclou la descripció detallada dels equips basats en la descàrrega d'arc utilitzats per la seva producció. El primer equip es va dissenyar durant la tesi de màster de l'autor i segueix les característiques d'un reactor convencional (*conventional ADP reactor*). El segon equip basat en la mateixa tecnologia de descàrrega d'arc, però modificat (*mADP reactor*) i dissenyat especialment amb l'objectiu de millorar les característiques del producte final.

- La tercera part exposa els resultats obtinguts durant aquesta tesi. L'estudi previ del reactor convencional basat en un disseny d'experiments de Plackett–Burman per avaluar l'efecte dels diferents paràmetres del reactor en la grandària dels nuclis de ferro. A partir d'aquest estudi, es va realitzar un estudi més específic en el nou reactor modificat on es van estudiar l'efecte del corrent d'arc utilitzat, la velocitat del flux d'heli i el contigut de ferrocè com a materia prima del ferro. Després es va realitzar l'estudi sistemàtic de les seves propietats magnètiques observant la dependència d'aquestes propietats amb la grandària dels nuclis de ferro. A continuació, es va presentar la comparació d'aquestes nanopartícules amb d'altres obtingudes mitjantçant el mètode de dipòsit químic en fase vapor (*CVD*). A partir d'aquesta comparació es va estudiar l'evolució estructural d'aquestes nanopartícules sotmetes a un tractament tèrmic en obsersació *in–situ* d'un microscopi de transmissió electrònica. Finalment, es va presentar un primer estudi de les propietats

col·loidals en suspensió d'aquestes nanopartícules recobertes amb un polímer d'alcohol de polivinil (PVA). Es presenta un primer estudi de l'internalització d'aquestes nanopartícules en cèl·lules tumorals HeLa.

- Per acabar es presenten les conclusions i l'apèndix que conté informació sobre les mostres produïdes i un llistat de publicacions, congressos, patents resultants d'aquest treball.

Sobre aquest treball cal destacar els següents punts:

- Es va dissenyar i posar a punt un reactor modificat basat en el mètode de descàrrega d'arc amb la finalitat d'obtenir nanopartícules superparamagnètiques de ferro recobertes de carboni que presenten estretes distribucions de grandàries tant en el nucli com la grandària primària total (incloent l'escorça de carboni). La generació controlada d'aquest tipus de nanopartícules ha permès l'estudi sistemàtic de les seves propietats morfològiques, estructurals i magnètiques, i per tant, la comprensió d'alguns punts importants en el camp de la nanociència com per exemple, quin són els mecanismes implicats en la formació d'aquest tipus de nanopartícules i com varien les seves propietats magnètiques en funció de la seva grandària.

- Els resultats preliminars obtinguts en un reactor de plasma convencional de descàrrega d'arc ens van permetre dissenyar d'un reactor de descàrrega d'arc per tal de superar diversos inconvenients comuns presents en aquesta tecnologia:

    - La generació de nanopartícules en detriment d'altres estructures, com ara nanotubs de carboni o nanopartícules de carboni, entre d'altres.
    - L'obtenció de nanopartícules amb distribucions de mida estretes amb propietats homogènies.
    - L'alta qualitat de les nanopartícules amb uniformitat en la seva composició.

- El disseny de Plackett–Burman dut a terme al reactor conventional va permetre avaluar quins paràmetres eren més significatius per controlar la mida del nucli de ferro. Els resultats van mostrar que el corrent d'arc era el paràmetre més influent. Els resultats obtinguts en l'espectroscòpia d'emissió òptica realitzats en l'estudi del plasma del reactor modificat van assenyalar una relació entre la temperatura del plasma amb el corrent d'arc utilitzat. Els resultats van assenyalar la importància de la temperatura en aquest tipus de tecnologia i el seu paper en el creixement de les nanopartícules.

- A partir de l'estudi de l'efecte del corrent i per tant de la temperatura del plasma, sobre la formació de les nanopartícules obtingudes en el reactor modificat es van extreure les següents observacions:

- Diferents mecanismes de creixement tenen lloc en la formació del nucli Fe en funció de la temperatura del plasma (corrent d'arc utilitzat). Petits nuclis Fe <6 nm obtinguts mitjançant l'ús de corrents baixes (< 30 A) promovien un creixement per condensació dels àtoms de ferro sobre la superfície del nucli (creixement superficial), mentre que el creixement dels nuclis més grans obtinguts mitjançant l'ús de corrents més alts van ser deguts principalment per la coagulació i la coalescència de dos nuclis de Fe. L'augment dels diàmetres del nucli de Fe es va associar a una expansió del volum del plasma quan s'augmentava el corrent, proporcionant velocitats de refredament més baixes i, per tant, majors temps de residència dels nuclis de Fe. En aquest punt, les col·isions degudes al moviment brownià dels nuclis eren més probables promovent d'aquesta manera la coagulació i la coalescència d'aquests nuclis en nuclis més grans.

- En relació al recobriment del carboni, els resultats d'anàlisi elemental van mostrar que el contingut de carboni augmentava de manera exponencial amb la temperatura del plasma. Juntament amb els resultats sobre la dependència de la grandària primària total en funció de la temperatura, es va trobar un diàmetre crític Fe necessari pel creixement del recobriment de carboni als voltants de ≈ 4.8 nm.

- Arribem a la conclusió que les nanopartícules de ferro recobertes de carboni obtingudes mitjançant el reactor de descàrrega d'arc modificat s'obtenen mitjançant dos mecanismes: en primer lloc, la nucleació homogènia dels nuclis de Fe fins a un diàmetre crític i finalment, el creixement del recobriment de carboni sobre els nuclis de Fe per nucleació heterogènia. Durant aquest procés, els processos de condensació, coagulació i coalescència tenen lloc segons els paràmetres del reactor utilitzats.

- Durant l'estudi de la velocitat del flux d'heli en la morfologia de les nanopartícules es va observar que aquest augment provocava una velocitat de refredament més gran de les nanopartícules. Malgrat alguns estudis proposen que una major velocitat promou nanopartícules més petites, els nostres resultats van indicar que un refredament controlat és més beneficiós per produir nanopartícules d'alta qualitat que un refredament ràpid d'acord amb d'altres autors [Joshi et al., 1990]. Amb l'augment de la velocitat del flux d'heli es va observar un augment en la desviació estandard geomètrica dels nuclis de ferro. A més a més, el ràpid refredament també va afectar a la formació de l'escorça de carboni promovent un grau de crital·linitat del carboni més baix (resultats obtinguts amb l'espectroscòpia Raman) i una grandària més petita pel que fa als diàmetres primaris totals.

- També es va investigar l'efecte d'incrementar la concentració de ferrocè en les solucions in-

troduïdes utilitzades com a matèria prima pel ferro (solucions de ferrocè diluit en isooctà). Utilitzant una velocitat de flux d'heli més baixa (1.6 l/min), l'augment del ferrocè produïa una augment en la grandària dels nuclis de ferro. Aquestes observations es trobaven d'acord amb els estudis teòrits duts a terme per Tashiro i col·laboradors [Tashiro et al., 2010], els quals van estudiar que l'augment dels vapors de Fe causava una nucleació de les nanopartícules de ferro a temperatures més altes. La nucleació a temperatures més elevades promou majors temps de residència pels nuclis de ferro que resulten en diàmetres més grans. Quan la velocitat de flux d'heli utilitzada era més gran (6.7 l/min), les distribucions de grandàries dels nuclis presentaven similars valors evitant d'aquesta forma l'efecte de la nucleació a altes temperatures. Això està d'acord amb els estudis teòrics duts a terme per Aristizabal i col·laboradors [Aristizabal et al., 2006], els quan van proposar que alts fluxos d'heli promovien la disminució de la concentració de vapors de metall per dilució degut a la barreja del vapor de ferro amb el gas d'heli.

- Els estudis magnètics de les nanopartícules obtingudes amb el reactor modificat van confirmar els resultats trobats en la caracterització morfològica descrita anteriorment:

    - Les nanopartícules presentaven un comportament superparamagnètic confirmant d'aquesta forma la petita grandària dels nuclis de ferro, < 10 nm observats amb la microscopia electrònica.

    - L'estudi de les propietats magnètiques en funció de la grandària dels nuclis de ferro confirmava l'estreta distribució de grandàries de les mostres obtingudes amb el reactor modificat.

    - La imanació de saturació es va calcular a partir de la dependència dels moments magnètics amb la grandària dels nuclis de ferro trobats a partir del model de Langevin, $M_s = 109$ Am^2/kg, el valor trobat va ser més gran que els valors d'òxids de ferro confirmant d'aquesta forma la protecció dels nuclis de ferro de l'oxidació gràcies al recobriment de carboni.

    - La variació dels moment magnètics per cada mostra coincideix amb els mecanismes de creixement observats en cada cas. Les nanopartícules que van créixer per condensació (creixement superficial) mostraven un creixement lineal del moment magnètic amb el volum dels nuclis de ferro. D'altra banda, les mostres que van créixer principalment per coagulació de dos nuclis, el moment magnètic es mantenia constant corresponent a un diàmetre magnètic de 5.5 nm coincidint amb les observacions de microscopia electrònica. Finalment, les mostres que van créixer per coalescència també mostraven un augment del moment magnètic però la tendència lineal no es va observar tan clarament, assenyalant la necessitat d'introduir una energia d'anisotropia i per tant, el model de Langevin era massa simple per aquests

casos.

- La dependència del camp coercitiu a 5 K en funció de la grandària dels nuclis de ferro confirmaven el comportament monodomini dels nuclis. No es va observar un camp coercitiu extremadament elevat confirmant la suposició dels nuclis de ferro com un únic spin (el model de Stoner–Wohlfarth).

- L'ajust de les corbes ZFC amb el model de Gittleman consideraven que els nuclis de ferro presentaven anisotropia uniaxial mostrant un creixement lineal de la temperatura de bloqueig amb la grandària dels nuclis. De l'ajust es va trobar una energia d'anisotropia constant als voltants de $5.4 \cdot 10^4$ J/m^3 molt aprop del valor corresponent del ferro en volum ($K_1 = 4.8 \cdot 10^4$ J/m^3), confirmant que la principal composició dels nuclis es tracta de α-Fe. Algunes mostres no seguien aquesta dependència degut a la simplicitat del model. Per exemple, nanopartícles que presentaven un contigut de carboni baix, els nuclis de ferro es trobaven més aprop presentant interacions dipolars magnètiques més altes, les quals no es considen del model Gittleman.

- Es va realitzar la comparació de nanopartícules obtingudes mitjançant el reactor modificat amb les obtingudes mitjançant el dipòsit químic en fase vapor (*CVD*). Aquestes diferències es van relacionar amb les diferències en el procès de síntesi. Pel que fa al nucli de ferro, amb el mètode de *CVD* s'obtenien distribucions de grandàries molt més amples (alta polidispersitat). Pel que fa a l'escorça de carboni, les nanopartícules obtingudes a partir de *CVD* presentaven major grau de carboni ordenat. No obstant això, vam observar que després d'aplicar un tractament tèrmic les nanopartícules obtingudes amb el reactor modificat presentaven propietats més estables.

- Nanopartícules obtingudes amb *mADP* i *CVD* es van sotmetre a un tractament tèrmic controlat. Durant els experiments, es va observar un comportament depenent de la grandària dels nuclis de ferro. Aquells que presetaven diàmetres inferiors a 10 nm augmentaven la seva grandària mitjançant Ostwald ripening, mentre els nuclis més grans que 10 nm en diàmetre augmentaven mitjançant coalescència. Aquestes observacions proporcionen característiques interessants a tenir en compte per futures investigacions sobre els mecanismes de creixement de les nanopartícules.

- Es va investigar una primera aproximació cap a les aplicacions biomèdiques amb aquest tipus de nanopartícules. En primer lloc, es va aconseguir millor l'estabilitat col·loidal de les nanopartícules en solució aquosa mitjançant l'ús de PVA. Els resultats presentats mitjançant basada en la sedimentació diferencial per centrigufació i les observacions de microscopia coincidien en la mesura de nanopartícules esfèriques de diàmetre total 50 nm i que contenien varis nuclis de ferro, presentant characterístiques interessants per aplicacions biomagnètiques. Estudis preliminars sobre la internalització de les nanopartícules

en cèllules HeLa van mostrar que les nanopartícules interaccionaven amb la membrana cel·lular, s'observaba major interacció i menys danyina quan les nanopartícules presentaven una major càrrega superficial positiva. Encara que són necessaris més estudis, podem concloure d'aquests primers estudis que aquest tipus de nanopartícules presenten característiques interessants per les aplicacions biomèdiques.